UC Irvine

UC Irvine Electronic Theses and Dissertations

Title

Demonstration of an Approach to Precisely Measure Long-Lived Gamma-ray Branching Ratios for Beta Emitters

Permalink

https://escholarship.org/uc/item/8kz8b3cd

Author

Hennessy, Amber

Publication Date

2018

Peer reviewed|Thesis/dissertation

eScholarship.org Powered by the California Digital Library
University of California

UNIVERSITY OF CALIFORNIA,
IRVINE

Demonstration of an Approach to Precisely Measure γ-ray Branching Ratios for Long-Lived β Emitters

DISSERTATION

submitted in partial satisfaction of the requirements
for the degree of

DOCTOR OF PHILOSOPHY

in Chemistry

by

Amber M. Hennessy

Dissertation Committee:
Professor A.J. Shaka, Chair
Professor Emeritus G.E. Miller
Professor R.W. Martin

2018

© 2018 Amber M. Hennessy

DEDICATION

I would like to dedicate this and everything I do
to my best friend and my biggest supporter,
my husband.

I am among those who think that science has great beauty.
A scientist in his laboratory is not only a technician:
he is also a child placed before natural phenomena
which impress him like a fairy tale.
We should not allow it to be believed
that all scientific progress can be reduced
to mechanisms, machines, gearings,
even though such machinery has its own beauty.
-Marie Curie

TABLE OF CONTENTS

Page

LIST OF FIGURES vi

LIST OF TABLES x

ACKNOWLEDGMENTS xii

CURRICULUM VITAE xiii

ABSTRACT OF THE DISSERTATION xv

1 Introduction 1

1.1 Structure of the Atom . . . 2
1.2 Ionizing Radiation . . . 3
1.3 Fission . . . 5
1.4 Radioactive Decay . . . 7
1.4.1 Quantification of Radioactive Decay . . . 9
1.4.2 Transient Equilibrium . . . 11
1.4.3 Secular Equilibrium . . . 12
1.4.4 No Equilibrium . . . 13
1.4.5 Successive Radioactive Decays . . . 14
1.4.6 Radioactive Growth, Decay, and Measurement . . . 14
1.5 The Need for Precision Measurements . . . 16
1.6 Difficulties Associated with Precision Measurements . . . 17
1.7 Project Details . . . 19

2 Experimental Approach 21

2.1 Nuclear Reactor-Produced Test Sources . . . 21
2.2 Fission Fragment Collection at the CARIBU Facility . . . 23
2.3 TAMU - Source Measurement . . . 29
2.3.1 HPGe Detector Operation . . . 29
2.3.2 HPGe Setup . . . 32
2.3.3 Gas Counter Operation . . . 34
2.3.4 Gas Counter Setup . . . 36
2.3.5 Coincidence Measurement . . . 40
2.4 Analysis of Measured Data . . . 43

2.4.1 γ-ray Peak Fitting . . . 43
2.4.2 $\beta\gamma$ Coincidence Peak Fitting . . . 48
2.4.3 Gas Counter Efficiency . . . 52
2.4.4 Simulations using GEANT4 . . . 55
2.4.5 β Particle Rate Associated to the Isotope of Interest . . . 55
2.4.6 γ-ray Branching Ration Equation . . . 57
2.5 Uncertainty Contributions . . . 58
2.5.1 Uncertainties in γ-ray Peak Area . . . 58
2.5.2 Uncertainties in Coincidence Peak Fitting . . . 63
2.5.3 Uncertainties in Measured γ-ray and Gas Counter Efficiencies . . . 63
2.5.4 Uncertainties in Simulated Gas Counter Efficiencies . . . 64
2.5.5 Uncertainty in β Particle Determination . . . 65
2.5.6 Uncertainty in Correlated Terms . . . 66
2.5.7 Uncertainty in the γ-ray Branching Ratio . . . 67

3 Simulations using GEANT4 **68**
3.1 Gas Counter Designs . . . 69
3.1.1 Differences Between Simulated and Physical Detector Designs . . . 73
3.2 Evolution of Radiation Source . . . 74
3.2.1 The β Decay Code and Fermi Function . . . 76
3.2.2 Radiation Size and Geometry . . . 78
3.3 Simulated Experiments . . . 79
3.4 Analysis of Simulated Output . . . 83

4 Method Viability - ^{95}Zr **86**
4.1 ^{95}Zr/^{95}Nb Overview . . . 86
4.1.1 CARIBU Source Production . . . 87
4.1.2 Decay Scheme . . . 88
4.1.3 Simulated β Energy Spectrum . . . 90
4.1.4 Half-lives of ^{95}Zr/^{95}Nb . . . 90
4.1.5 Simulated Gas Counter Efficiency . . . 91
4.1.6 Reactor-Produced Source . . . 91
4.1.7 CARIBU-Produced Source . . . 92
4.2 ^{95}Zr Reactor-Produced Source Measurement . . . 94
4.3 ^{95}Zr CARIBU-Produced Source Measurements . . . 100
4.3.1 Initial Measurement of ^{95}Zr . . . 100
4.3.2 Final Measurement of ^{95}Zr . . . 109

5 Method Application - ^{144}Ce **121**
5.1 ^{144}Ce/^{144}Pr Overview . . . 121
5.1.1 CARIBU Source Production . . . 122
5.1.2 Decay Scheme . . . 123
5.1.3 Simulated β Energy Spectrum . . . 125
5.1.4 Half-Lives of ^{144}Ce/^{144}Pr . . . 126
5.1.5 Simulated Gas Counter Efficiency . . . 126

5.2 ^{144}Ce CARIBU-Produced Source Measurements 131
5.2.1 Initial Measurement of ^{144}Ce 134
5.2.2 Final Measurement of ^{144}Ce 135

6 Method Application - ^{147}Nd **144**
6.1 ^{147}Nd/^{147}Pm Overview 144
6.1.1 CARIBU Source Production 145
6.1.2 Decay Scheme 146
6.1.3 Simulated β Energy Spectrum 148
6.1.4 Half-lives of ^{147}Nd/^{147}Pm 149
6.1.5 Simulated Gas Counter Efficiency 150
6.2 ^{147}Nd CARIBU-Produced Source Measurement 156

7 Future Work and Conclusion **170**
7.1 Future Work 170
7.1.1 Method Improvements 170
7.2 Conclusion 172

Bibliography **173**

LIST OF FIGURES

Page

1.1 A generic β energy spectrum showing a range of energies for the emitted β particle. 4

1.2 Fission product yields as a function of mass number for ^{235}U, ^{238}U, ^{239}Pu, and ^{252}Cf[1]. 6

1.3 The process by which a conversion electron, x-ray, and Auger electron emission occurs. The red line is an emitted γ-ray. 8

1.4 The possible types of equilibrium between parent and daughter isotopes. It is also possible for no equilibrium to occur between the pair. Equilibrium relationships are dependent on the relative half-life of parent and daughter isotopes. 11

1.5 β energy spectra for (a) a high Q value decay and (b) a low Q value decay showing the relative spread and most probable β energies. For these spectra, a Q = ∼3 MeV results in the most probable energy being roughly 1/3 of the total energy of the reaction whereas a Q = ∼150 keV results in a most probable energy close to 1/30 of the total energy. 18

2.1 Fission product yields for ^{252}Cf showing mass number versus the probability of yield[2]. 24

2.2 Simplification of the gas catcher used at CARIBU. Fission products from spontaneous fission of ^{252}Cf interact with the He gas and are directed toward the RF cone, which concentrates the ions into a beam[3]. 25

2.3 A simplified picture of the components that make up the beam line. Source implantation occurs shortly after beam separation in order to achieve the highest intensity of ions possible[4]. 26

2.4 (a) Placement of the cross on the beam line. The arm which holds Si detectors and source foil fits in at the top. (b) Looking directly at the beam on the backside of the cross, one can see the foil positioned in the path of the oncoming beam. The arm that fits into the cross is shown for the side that faces the beam (c) and the side that faces away from the beam (d). 27

2.5 Interactions of γ-rays with the germanium crystal inside the HPGe detector[5]. 30

2.6 Characteristic features of a γ-ray spectrum using a ^{137}Cs source[6]. 31

2.7 (a) Texas A&M meticulously-calibrated HPGe detector used to measure γ-rays with high precision. (b) Full energy peak efficiency as a function of γ-ray energy of the TAMU HPGe detector[7]. 33

2.8 The pathway and interactions of an ionizing particle through detection gas in the presence of a bias. 35

2.9 Schematic of the gas counter system. 37
2.10 (a) A source holder that fits into (b) each half of the detector creating a sealed system (c). 38
2.11 Generic method by which Radware fits a γ-ray peak. 46
2.12 ASCII data format of (a) buffer, (b) coincidence, and (c) heavy ion information. The buffer occurs after the transfer of data. The header appears each 54.93 sec. and signifies the end of a cycle. The coincidence data set occurs each time there is a measurable coincidence event and contains the vital information about timing and energies of the β particle and γ-ray. The heavy ion data set occurs at a specific rate when the source strength is low. 49
2.13 Generic source activity over time. Two measurements of this source are taken over this range showing a decay correction for the activity to some reference time, t_0. 54
2.14 Variations in peak fitting result in an uncertainty that is half the midpoint of the two extremes. 59
2.15 Spectra from a source and dedicated background measurement overlaid. To align the peaks of interest, background peaks found in both spectra are fit to determine their center. The dedicated background is then shifted so that proper alignment is achieved. 60
2.16 Simplification of the qualities that make up a γ-ray peak. 62
3.1 Evolution of gas counter designs simulated in GEANT4. 71
3.2 Final simulated version of the gas counter representing all the major features of the physical detector. 73
3.3 Source holders for a reactor-made and CARIBU-made sources. The reactor source (a) is held in place with thin wires while the CARIBU source (b) consists of carbon foil floated on top of the source holder. 74
3.4 β energy spectra for the main transitions of ^{144}Ce, ^{95}Zr, and ^{147}Nd. 75
3.5 (a) Fermi function calculated for non-relativistic and relavistic β particles of ^{144}Ce and (b) the resulting β energy spectra for both relativistic and non-relativistic calculations. 77
3.6 Placement of the simulated radioactive isotopes within the foil. 79
3.7 (a) Deposition of energy spectrum produced from GEANT4 simulations. (b) Simulation to determine the material response to radioactive ions and the level of attenuation each imposes on β particles. 80
3.8 Simplified example of a decay scheme and possible pathways to ground state (GS). 84
4.1 Mass 95 fission product yield from ^{252}Cf[8]. 87
4.2 A simplified decay scheme exhibiting the major transitions of ^{95}Zr decaying to ^{95}Nb decaying to ^{95}Mo. The decay to the isomeric state of ^{95m}Nb is also seen at the 235.7 keV energy level. 89
4.3 (a) Major β transitions for ^{95}Zr and ^{95}Nb and (b) decay of the source over time. 90
4.4 (a) Voltage plateau and (b) change in counts per 100V. 96
4.5 (a) Background-subtracted γ-ray spectrum and (b) $\beta\gamma$ coincidence spectrum measurement of a reactor-produced source. 97

4.6 (a) γ-ray spectrum of the CARIBU beam monitoring of mass 95 isotopes. (b) Beam intensity over the length of the measurement. (c) Growth and decay of ^{95}Zr and ^{95}Nb source. The gray section indicates the duration of the measurement performed at TAMU. 101
4.7 (a) γ-ray spectra of the source and background measurements overlaid, (b) background-subtracted γ-ray source spectrum, and (c) $\beta\gamma$ coincidence spectrum of a ^{95}Zr/^{95}Nb CARIBU-made source. 103
4.8 (a) γ-ray spectrum of the CARIBU beam monitoring of mass 95 isotopes. (b) Beam strength over the duration of the measurement. (c) Growth and decay of ^{95}Zr and ^{95}Nb. The gray section indicates the length of the measurement. 111
4.9 (a) A measured voltage plateau using a ^{147}Nd source and (b) the change in counts per 100 V. 112
4.10 (a) γ-ray spectrum, (b) background subtracted γ-ray spectrum, and (c) measured coincidence spectrum of the CARIBU ^{95}Zr/^{95}Nb source. 113
4.11 Fits of both (a) γ-ray and (b) $\beta\gamma$ coincidence peaks. 115
4.12 The TDC spectrum of the source and its individual contributions. 116
4.13 (a) A comparison of the deposition of energy spectra between measured and GEANT4 simulated data for the total ^{95}Zr/^{95}Nb source. The zoomed region shows an average deposited energy of 4.1 keV and a threshold of 1.1 keV. In addition, specific transition deposition of energy spectra are shown for β particles gated on (b) 724.2, (c) 756.7, and (d) 765.8 keV γ-rays. 117
5.1 Mass 144 fission product yield from ^{252}Cf[8]. 122
5.2 A simplified decay scheme exhibiting the major transitions of ^{144}Ce decaying to ^{144}Pr decaying to ^{144}Nd. The decay to the isomeric state of ^{144m}Pr is also seen at the 59 keV energy level. 124
5.3 (a) Major β transitions for ^{144}Ce and ^{144}Pr and (b) decay of the source over time. 125
5.4 (a) γ-ray spectrum of the CARIBU beam monitoring of mass 144 isotopes. (b) Beam strength over the length of the measurement. (c) Growth and decay of ^{144}Ce and ^{144}Pr. The gray section indicates the length of the measurement. 132
5.5 First measurement of $\beta\gamma$ coincidences of ^{144}Ce source showing the presence of ^{103}Ru contamination. 134
5.6 (a) Voltage plateau and (b) change in counts per 100 V measured during the first ^{144}Ce source experiment. 135
5.7 (a) γ-ray spectrum, (b) background subtracted γ-ray spectrum, and (c) measured coincidence spectrum of the CARIBU ^{144}Ce/^{144}Pr source after over a year of decay. Each spectrum shows the lack of contamination present within the source. 136
5.8 (a) γ-ray and (b) $\beta\gamma$ coincidence peak fits of 80.1 and 133.5 keV peaks. . . . 137
5.9 The TDC spectrum generated from $\beta\gamma$ coincidence measurement of ^{144}Ce. . 140
5.10 (a) A comparison of the deposition of energy spectra between measured and GEANT4 simulated data. The zoomed region shows an average deposited energy of 2.7 keV and a threshold of 1.1 keV. (b) A transition-specific deposition of energy spectrum is shown for β particles gated on 133.5 keV γ-ray. 140
6.1 Mass 147 fission product yield from ^{252}Cf[8]. 145

6.2 A simplified decay scheme exhibiting the major transitions of ^{147}Nd decaying to ^{147}Pm decaying to ^{147}Sm. 147
6.3 (a) Major β transitions for ^{147}Nd and (b) decay of the source over time. . . . 149
6.4 (a) γ-ray spectrum of the CARIBU beam monitoring of mass 147 isotopes. (b) Beam intensity over the length of the measurement. (c) Growth and decay of ^{147}Nd and ^{147}Pm. The gray section indicates the time during measurement at TAMU. 155
6.5 (a) γ-ray spectrum, (b) background subtracted γ-ray spectrum, and (c) measured coincidence spectrum of the CARIBU ^{147}Nd/^{147}Pm source. 159
6.6 Two γ-ray spectra overlaid showing the effect of the gas counter on the 91.1 keV peak. These low energy γ-rays scatter off the copper housing and produce a broad peak on the low energy side of the 91.1 keV γ-ray. 160
6.7 Sample fits of the γ-ray and $\beta\gamma$ peaks for 91.1 and 531 keV transitions of a ^{147}Nd source. 161
6.8 TDC spectrum for the measurement of ^{147}Nd source. 164
6.9 (a) A comparison of the deposition of energy spectra between measured and GEANT4 simulated data. Gas counter events gated on the (b) 91.1 and (c) 531 keV γ-rays agree well with simulated data due to the lack of CEs associated to these decays. 165
6.10 A comparison between literature γ-ray branching values and those determined by this method. A value close to 1 is a good agreement. 168

LIST OF TABLES

		Page
3.1	Gas counter detection efficiency for x-rays and γ-rays of generic energies.	82
4.1	Literature branching ratios for γ-rays and β particles[9].	88
4.2	Simulated results for gas counter efficiency of a 1.31 μm reactor-made ^{95}Zr source.	92
4.3	Simulated results for gas counter efficiency of a 0.2 μm CARIBU-made ^{95}Zr source.	93
4.4	Manufacturer quoted limits of contaminates within an enriched ^{94}Zr foil.	96
4.5	Simulated and measured results for gas counter efficiency of a 1.31 μm reactor-made ^{95}Zr source. A threshold of 1.5 keV was imposed on the simulation results to best match measured results.	98
4.6	Measured peak rates for ^{95}Zr/^{95}Nb CARIBU source. The rates listed are those detected by the instruments which measured them.	105
4.7	Uncertainty contributions associated to the γ-ray peak analysis for ^{95}Zr/^{95}Nb CARIBU source.	105
4.8	Gas counter efficiencies for the main transitions of ^{95}Zr/^{95}Nb CARIBU source for GEANT4 simulations and measured data. A threshold of 1.1 keV was applied to these simulations.	106
4.9	γ-ray branching ratio contributions, uncertainties, and final values for ^{95}Zr/^{95}Nb decay.	108
4.10	Peak rates for γ-ray and $\beta\gamma$ coincidence measurements of ^{95}Zr/^{95}Nb CARIBU source.	114
4.11	Uncertainty contributions associated to the γ-ray peak analysis for ^{95}Zr/^{95}Nb CARIBU source.	114
4.12	Measured and GEANT4 simulated gas counter efficiency values for a ^{95}Zr/^{95}Nb CARIBU source.	118
4.13	Calculated γ-ray branching ratio values for a ^{95}Zr/^{95}Nb CARIBU source.	120
5.1	Literature branching ratios for γ-rays and β particles[10].	123
5.2	Literature branching ratios for γ-rays and CE emissions associated to the decay of ^{144}Ce[9]. This isotope is highly converted.	125
5.3	List of possible decay pathways to ground state (GS) or isomeric state of ^{144}Ce including emitted β particles, CEs, and γ-rays.	128
5.4	Simulated results for gas counter efficiency of a 0.2 μm CARIBU-produced ^{144}Ce source.	131
5.5	Measured peak rates for γ-ray and $\beta\gamma$ coincidence measurements of ^{144}Ce/^{144}Pr CARIBU source.	139

5.6 Uncertainty contributions associated to the γ-ray peak analysis for $^{144}Ce/^{144}Pr$ CARIBU source. 139
5.7 Measured and GEANT4 simulated gas counter efficiency values for a $^{144}Ce/^{144}Pr$ CARIBU source. 141
5.8 Calculated γ-ray branching ratio values including the contributions and uncertainties associated to the measurement for a $^{144}Ce/^{144}Pr$ CARIBU source. 143
6.1 Literature branching ratios for γ-rays and β particles from the decay of ^{147}Nd[9]. 148
6.2 γ-ray and conversion electron emissions from excited states associated to the decay of ^{147}Nd[9]. This isotope is highly converted. 149
6.3 List of possible pathways from the decay of ^{147}Nd to ground state (GS) of ^{147}Pm. 151
6.4 Simulated results for gas counter efficiency of a 0.2 μm CARIBU-made $^{147}Nd/^{147}Pm$ source. 156
6.5 Measured peak rates for γ-ray and $\beta\gamma$ coincidence measurements of $^{147}Nd/^{147}Pm$ CARIBU source. 162
6.6 Uncertainty contributions associated to the γ-ray peak analysis for $^{147}Nd/^{147}Pm$ CARIBU source. 163
6.7 Measured and GEANT4 simulated gas counter efficiency values for a $^{147}Nd/^{147}Pm$ CARIBU-made source. 166
6.8 Calculated γ-ray branching ratio values for a $^{147}Nd/^{147}Pm$ CARIBU-produced source. 168

ACKNOWLEDGMENTS

I would like to thank Nicholas Scielzo and Kay Kolos, Lawrence Livermore National Laboratory (LLNL) research collaborators. Nick has graciously mentored and spent untold hours discussing every aspect of this project with me. Kay has made the mundane and tedious parts of this project memorable. I will miss the almost daily talks we had and the combined years we spent devoted to the success of this project.

I would like to thank George Miller and A.J. Shaka, UC Irvine academic advisors. Dr. Miller introduced me to the world of nuclear science to which I have developed a genuine passion for understanding. His level of knowledge and dedication to teaching students has forever influenced the way I conduct myself as a scientist. Dr. Shaka gave me a chance and accepted me as his graduate student. He allowed me the freedom to dictate the way I performed research without judgment or criticism. He has always made himself available to discuss research or the evolution of the price of milk.

I would like to acknowledge the extensive amount of time spent by John Hardy and Victor Iacob, collaborators at Texas A&M University. These amazing scientists have given many months of their time and detection system for the purpose of completing this project. They have bestowed upon me a deeper understanding of what makes a precision measurement.

I would like to thank Jonathan Wallick, the nuclear reactor supervisor at the UC Irvine Nuclear Reactor Facility. His patience and willingness to teach accelerated my understanding of nuclear reactor physics. He instilled a foundation of hard work that I will carry throughout my career.

I would also like to acknowledge the Nuclear Science and Security Consortium for funding this project under Department of Energy National Nuclear Security Administration Award Number DE-NA0003180. This agency not only supplied financial help, but also assisted with the creation of a network of scientists with a common goal, many of whom I expect to see again in the future. Meetings and summer schools made available through this grant gave me an understanding of the broader impacts of this research.

I would also like to acknowledge LLNL for supporting me in the last phase of my research as a graduate student intern. This assistance gave me the opportunity to present a well-rounded thesis without urgency, resulting in a complete and new contribution to the scientific community.

CURRICULUM VITAE

Amber M. Hennessy

EDUCATION

Doctor of Philosophy in Chemistry **2018**
University of California Irvine *Irvine, CA*

Master of Science in Chemistry **2016**
University of California Irvine *Irvine, CA*

Bachelor of Science in Chemistry **2012**
University of California Irvine *Irvine, CA*

RESEARCH EXPERIENCE

Graduate Research Assistant **2013–2018**
University of California, Irvine *Irvine, CA*

Nuclear Regulatory Commission Licensed Nuclear Reactor Operator **2013–2017**
Senior Reactor Operator *Irvine, CA*

Reactor Operator *Irvine, CA*

TEACHING EXPERIENCE

Teaching Assistant **2013–2014**
University of California, Irvine *Irvine, CA*

PRESENTATIONS

Poster Presentation **June 2018**
University Program Review

Poster Presentation **May 2018**
National Nuclear Security Administration and Commissariat à L'énergie Atomique of France Postdoctoral Partnership Program

Poster Presentation **June 2018**
University Program Review

Poster Presentation **June 2017**
University Program Review

Oral Presentation **Sept. 2017**
Nuclear Science and Security Consortium Workshop and Advisory Board Meeting

Poster Presentation **June 2016**
University & Industry Technical Interchange Program and Technical Review Meeting

Poster Presentation **June 2015**
University & Industry Technical Interchange Program and Technical Review Meeting

Oral Presentation **Sept. 2015**
The National Organization of Training Research and Test Reactors Conference

ABSTRACT OF THE DISSERTATION

Demonstration of an Approach to Precisely Measure γ-ray Branching Ratios for Long-Lived β Emitters

By

Amber M. Hennessy

Doctor of Philosophy in Chemistry

University of California, Irvine, 2018

Professor A.J. Shaka, Chair

Measurements of γ-rays are a reliable way to identify the quantities of different long-lived radioactive isotopes present in a sample. Many of the radioactive nuclei of interest emit γ-rays at characteristic energies that can be detected with high energy resolution and limited background noise using high purity germanium (HPGe) detectors. However, these γ-rays are only emitted in a fraction of the decays, and this fraction (known as the γ-ray branching ratio) must be known accurately to determine the total number of atoms present.

In the following work, I discuss, in detail, the development of a general method for accurately and efficiently determining the γ-ray branching ratios of fission products through measurement of the emitted β particles, conversion electrons, and γ-rays with extreme precision. I then apply this technique to long-lived fission products that have branching ratios that either have large uncertainties (^{147}Nd) or that have only been precisely measured once (^{144}Ce).

The steps to measure γ-ray branching ratios are: (1) design, create, and simulate a highly-efficient gas counter through a collaboration between the University of California Irvine (UCI) and Lawrence Livermore National Laboratory (LLNL), (2) produce radioactive test sources using the Texas A&M Nuclear Reactor to identify any potential challenges or systematic effects, (3) run experiments at the Californium Rare Ion Breeder Upgrade (CARIBU) facility

at Argonne National Laboratory (ANL) to collect isotopically-pure samples on thin foil backings, (4) perform β spectroscopy using the custom-made gas counter, and (5) perform γ-ray spectroscopy using the precisely calibrated high-purity germanium (HPGe) detector at Texas A&M University. Through the efforts of these participating institutions, γ-ray branching ratios are measured with a precision of $\sim$1%.

Chapter 1

Introduction

The high-energy density (HED) environments of stellar interiors, inertial confinement fusion experiments, nuclear reactors, and nuclear weapons blasts produce many short-lived radioactive isotopes that are typically difficult to study because the isotopes decay before any conclusive measurements can be made. In these types of environments, extreme pressures and temperatures limit the amount of direct information available.

Much of the information learned from these systems involving fission chain reactions is obtained by detecting long-lived radioisotopes produced from the decay of these initial, shorter-lived isotopes. The fission products ^{147}Nd, ^{144}Ce, and certain other relatively long-lived isotopes play a crucial role in extracting information necessary to understand these environments. Fission product yields are typically determined using γ-ray spectroscopy. Often times, the largest sources of uncertainties in these calculations are a result of insufficient nuclear data concerning γ-ray branching ratios.

These large sources of uncertainties have far reaching consequences in many measurements where γ-rays are detected. Experiments involving the quantification of isotopes in measurements of neutron energy dependence of fission product yields, nuclear reactor design,

stockpile stewardship, and fundamental theories of fission could benefit from improved absolute normalization of measurements involving γ-ray branching ratios.

1.1 Structure of the Atom

Atoms are the basic building blocks of matter which make up the known universe. Their properties can be described by chemistry and their interactions by quantum mechanics. Combinations of atoms make up molecules that interact in different ways to form the various states of matter: solid, liquid, gas, and plasma. Individual atoms have a size of roughly 0.1 nm ($\sim$1.0 Å). The majority of the atomic mass is located at its center called the nucleus.

An atom is comprised of protons, neutrons, and electrons. Protons are positively charged hadrons with a mass of 1 u or 1.6606×10^{-27} kg. Neutrons are also hadrons that are neutral in charge and have a mass that is slightly higher than the proton (although its behavior in the nucleus allows for it to also have a 1 u). Protons and neutrons are referred to as nucleons because together they make up the atomic nucleus. The number of protons (atomic number, Z) within a nucleus determines the element of the atom and its chemical behavior. The number of both protons and neutrons (atomic mass number, A) determine the isotope. All isotopes of a given element have the same number of protons, but different number of neutrons and, as a result, different atomic masses. There are 120 known elements and 3,386 isotopes[9]. The majority of isotopes are radioactive and are artificially created. The most common notation to describe a specific isotope is ${}^{A}_{Z}X$ where X is the specific element. For example ${}^{14}_{6}C$ would denote a carbon-14 atom commonly employed in radioactive dating[11].

The positively-charged nucleus is surrounded by electrons which maintain the stability of the atom by Coulombic forces. Electrons are subatomic particles with a negative charge. The mass of the electron is roughly 0.054% the size of the proton[12] and is generally ignored when

discussing atomic masses. The majority of an atom's volume is comprised of electron clouds which assume certain well-known shapes. An atom is considered neutral when the number of protons and electrons are equal. The process of ionization occurs when an external force causes the ejection of an electron from the atom, creating a disproportionality of the number of protons and electrons.

Processes involving the nucleus of an atom make up the heart of nuclear transitions. The structure of the nucleus undergoes changes in the number of neutrons or protons whereby the different combinations describe different types of radioactive emissions. The energies released by the emitted particles can be described by comparing the initial and final states of the nucleus.

1.2 Ionizing Radiation

There are four main types of ionizing radiation: α particles, β particles, neutrons, and γ-rays. Ionization occurs when an electron is freed from an atom due to interactions with some type of radiation. Electrons in low-lying atomic orbitals close to the nucleus have higher binding energies than their counterparts in outer orbitals. It follows that electrons which reside in outer orbitals (the valence electrons) are more easily liberated from the atom because they are less tightly bound to the nucleus due to their proximity to the nucleus.

An α particle is a helium nucleus (bound together by two protons and two neutrons) with a +2 charge. Due to its charge, α particles do not travel far distances in air and can be readily absorbed by a thin sheet of paper. An α decay occurs mostly in heavy atoms which undergo atomic transmutation into another element. An α particle is emitted at discrete energies characteristic of the isotope from which it is emitted.

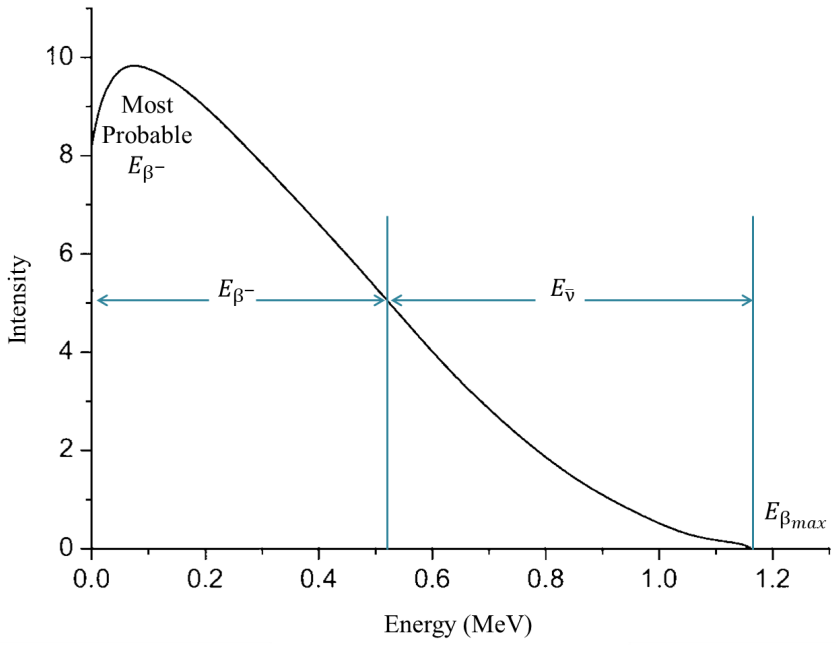

Figure 1.1: A generic β energy spectrum showing a range of energies for the emitted β particle.

A β particle is similar to an electron with the major difference being its origination from an atomic nucleus instead of an atomic orbital around the nucleus. The specific energy of a β particle at the time of emission depends on the energy spectrum of the isotope. The most probable energy at which a β particle is born occurs in the low energy region relative to some maximum energy, $E_{\beta_{max}}$ (Fig. 1.1). Due to their negative charge, β particles interact greatly with matter and are absorbed relatively easily. They can be readily stopped by a thin sheet of metal.

A neutron is a neutral particle with roughly the same mass as a proton. Due to the lack of Coulombic attraction, the neutron's main interaction with matter is through collisions with other nuclei. As a result, its travel in air is farther than either α or β particles. Neutrons have the ability to induce atomic transmutation through absorption into a nucleus and subsequent decay of that isotope into a new isotope often of a different element. Neutrons are best stopped by material that is of similar size, such as a proton. Water is very effective at reducing the travel distance of neutrons.

In contrast to other sources of ionizing radiation, a γ-ray (high energy light) has no mass, no charge, and is emitted with discrete energies. The energy of the γ-ray can be a major identifier of the decaying isotope. The interactions between γ-rays and matter are different than that of α or β particles, allowing for large travel distances before absorption. High Z materials such as lead are most effective at blocking penetration of γ-rays.

1.3 Fission

Fission occurs when a large, unstable nucleus breaks into smaller parts releasing neutrons and a large amount of energy. The release of energy is both electromagnetic radiation in the form of γ-rays and also kinetic energy carried by the emitted particles expelled as a result of Coulombic repulsion. The resulting fragments, called fission products, are radioactive themselves and go through a series of successive decays until becoming a stable nucleus over time. Along with the initial release of radioactivity during the fission process, the fission products also emit some form of radiation during their decay to stability. In general, these initial fission products are highly radioactive and decay almost immediately to longer-lived fission products. These later fission products may remain radioactive anywhere from hours to years before completely decaying.

In order for the fission process to occur, the binding energy of the initial nucleus must be higher than that of the sum of the products. Thus fission is energetically preferable with the larger mass nuclei. Fission can happen spontaneously through natural radioactive decay or may be induced by neutron bombardment of a heavy nucleus. Spontaneous fission occurs in the largest masses and competes with the more readily occurring α decay. It is observed in masses of A=226 or more[13], with increasing probability, as mass number increases.

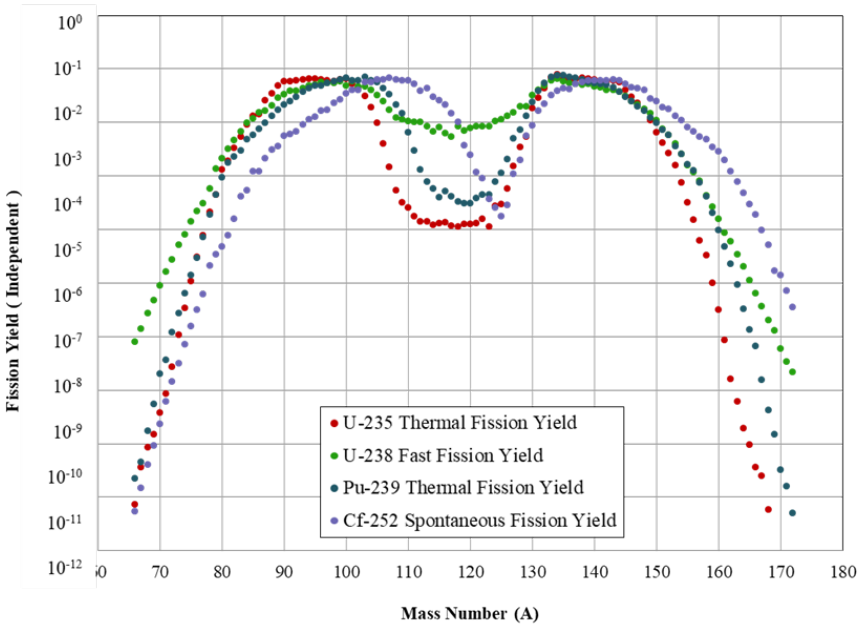

Figure 1.2: Fission product yields as a function of mass number for ^{235}U, ^{238}U, ^{239}Pu, and ^{252}Cf[1].

Neutron bombardment of heavy nuclei resulting in fission cause destabilization of the nucleus that makes decay by fission energetically favorable. Depending on the isotope, different energies of the incident neutron have varied probabilities to induce fission. A thermal neutron with energy 0.025 eV has high probability to be absorbed in ^{235}U and ^{239}Pu, but a low probability for ^{238}U. Conversely, a fast neutron of 14 MeV energy has high probability to be absorbed by ^{238}U, but low probabilities for ^{235}U and ^{239}Pu. It is possible for this process to be self-sustaining in the sense that the emitted fission neutrons could go on to induce more fission in a sustainable chain reaction. This idea of a self-sustaining fission chain reaction is used in nuclear reactors for base-load power production. These fissile isotopes generally have odd mass numbers that gain enough energy from the absorbed neutron to make fission favorable.

In both spontaneous and neutron-induced fission, typical fission products are asymmetrical in mass. Fig. 1.2 shows several cumulative fission product yields (the probability of a fission

product with a specific mass number produced per fission event) for several different fissionable isotopes. Depending on the isotope undergoing fission and the energy of the incident neutron, the shape and yields are different. However, they each follow the same trend; two fission products born at low and high atomic masses with a dip in the center of more unlikely atomic masses.

1.4 Radioactive Decay

Most fission products decay through emission of a β particle. This decay mode occurs as an unstable, neutron-rich nucleus tries to obtain a more stable form. The result is the transmutation of one element (parent, ${}^{A}_{Z}X$) to another (daughter, ${}^{A}_{Z+1}Y^{*}$) as a neutron changes to a proton within the nucleus of the atom. The resulting daughter isotope has the same mass number, but a different proton number than its parent.

$$ {}^{A}_{Z}X \rightarrow {}^{A}_{Z+1}Y^{*} + \beta^{-} + \bar{\nu} \tag{1.1} $$

Along with emission of a β particle, an $\bar{\nu}$ (antineutrino) and, most often, γ-ray are ejected. An $\bar{\nu}$ shares the total energy released during the emission (Q value) in addition to a small (negligible) amount of recoil energy:

$$ Q = \left[m_N \left({}^{A}_{Z}X \right) - m_N \left({}^{A}_{Z+1}Y^{*} \right) - m_e - m_{\bar{\nu}} \right] c^2 \tag{1.2} $$

Where $m_N \left({}^{A}_{Z}X \right)$ is the mass of the nucleus of the parent isotope, $m_N \left({}^{A}_{Z+1}Y^{*} \right)$ is the mass of the nucleus of the daughter isotope, m_e is the mass of the emitted β particle (electron mass), and $m_{\bar{\nu}}$ is the mass of $\bar{\nu}$. The mass of the parent nucleus can be found by rearranging the standard mass for the atom and solving for m_N:

$$ m_N \left({}^{A}_{Z}X \right) c^2 = m_N \left({}^{A}_{Z}Y^{*} \right) c^2 + Z m_e c^2 - \sum_{i=1}^{Z} B_i \tag{1.3} $$

Where Z is the atomic number and B_i is the electron binding energy. Eq. 1.3 can be simplified by neglecting the mass of the $\bar{\nu}$ and the binding energies (small for high Z atoms) resulting in the Q value being equal to the difference in masses between the parent and daughter

nuclides:

$$Q = \left[m_N\left({}^{A}_{Z}X\right) - m_N\left({}^{A}_{Z+1}Y^{*}\right)\right]c^2 \tag{1.4}$$

The amount of energy taken by the $\bar{\nu}$ varies for each decay causing a spread of possible β particle energies (Fig. 1.1). Once the parent nucleus has ejected the β particle and $\bar{\nu}$, the daughter nucleus is most likely in some excited state. It will de-excite by emission one or more γ-rays to the ground state level. While not emitted from the initial decay of the parent, the γ-rays share the Q value energy (alongside the β particle and the $\bar{\nu}$) in the form of the daughter mass ($m_N\left({}^{A}_{Z+1}Y^{*}\right)$).

In general, the decay path whereby a β particle and $\bar{\nu}$ are emitted in addition to a γ-ray (as a result of the de-excitation of the daughter nucleus) is simple. Detection of β particles and γ-rays are relatively straightforward. There exists more complex emissions where, rather than emission of a γ-ray, a conversion electron (CE) is emitted. In these CE decays, the γ-ray which is emitted from the nucleus (similar to the simple decay path) becomes absorbed by an orbital electron. The energy of the absorbed γ-ray is enough to eject the electron from its orbital and ultimately from the atom (Fig. 1.3). This electron has energy equal to the absorbed γ-ray minus the binding energy of that orbital electron. In addition to a release of an electron, a characteristic x-ray is emitted as an outer-shell electron fills the vacancy

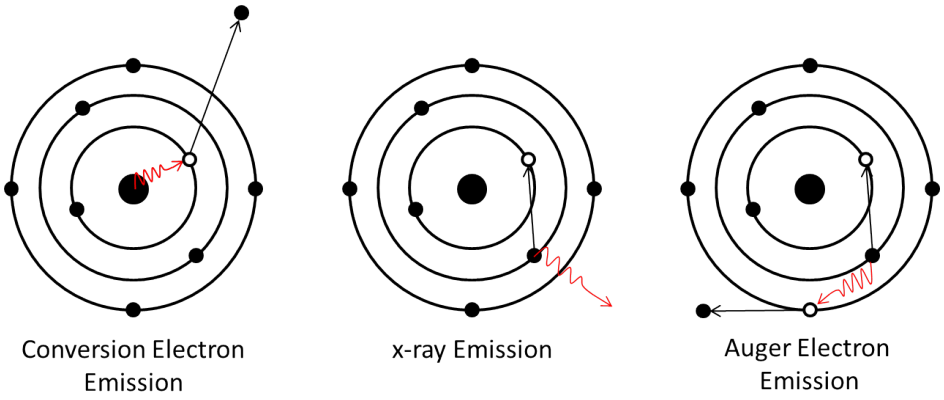

Figure 1.3: The process by which a conversion electron, x-ray, and Auger electron emission occurs. The red line is an emitted γ-ray.

left behind by an inner-shell electron. The energy of the emitted x-ray is determined by the difference in energy of the higher and lower orbital states.

In these decays where a β particle, CE, and x-ray is emitted, no γ-ray is seen. It is also possible for the x-ray to become absorbed by another electron and eject that electron as well (instead of emitting the x-ray). This second orbital electron emission is called an Auger electron. In this case, the Auger electron has kinetic energy equal to the difference between the x-ray energy from CE and the binding energy of the atomic orbital of which the Auger electron originated from. Overall, it is possible for one β particle and one or two electrons to be emitted in place of a γ-ray.

1.4.1 Quantification of Radioactive Decay

Radioactive β decay, when a neutron transforms into a proton, can be expressed as a statistical process by which a parent nucleus transitions into a daughter nucleus. The disintegration probability can be expressed as:

$$\frac{dN}{dt} = \lambda N \tag{1.5}$$

Where N is the number of radioactive nuclei, dN/dt is the change of radioactive nuclei per unit time, and λ is the decay constant (the probability of decay per nucleus per unit time). The decay constant is specific to the isotope and is calculated using the half-life, $t_{1/2}$:

$$\lambda = \frac{\ln 2}{t_{1/2}} \tag{1.6}$$

The rate of decay, A, defined as the number of disintegrations per unit time, is related to the number of radioactive atoms N through the following expression:

$$A = -\frac{dN}{dt} = \lambda N \tag{1.7}$$

As radiation causes a decrease in the amount of nuclei present, the expression has a negative sign inserted within it. Rearranging the equation and taking the integral of this expression:

$$\ln(N) = -\lambda\, t + c \tag{1.8}$$

Where c is some constant which arises out of the integral. Next, taking the exponential of both sides:

$$N(t) = c * e^{-\lambda t} \tag{1.9}$$

Solving for c at time $t = 0$ when the number of nuclei is equal to $N(0) = N_0$.

$$N(0) = N_0 = c * e^{-\lambda * 0} = c * 1 \tag{1.10}$$

Substituting $c = N_0$ into Eq. 1.9, one obtains the expression for the number of nuclei remaining after some unit of time.

$$N(t) = N_0 * e^{-\lambda t} \tag{1.11}$$

Similarly, if calculating the activity of a sample, A, one can use the same method to produce a similar expression:

$$A(t) = A_0 * e^{-\lambda t} \tag{1.12}$$

It is important to note the rate of disintegration decreases over time as the source becomes less active as it decays. There are several circumstances in which a radioactive parent decays into a radioactive daughter. This daughter has its own rate of decay and $t_{1/2}$ which must be taken into account when calculating the total activity of a sample. The parent nucleus decays as discussed in Eq. 1.13 where the subscript A denotes the parent isotope:

$$A_A = -\frac{dN}{dt} = \lambda_A N_A \tag{1.13}$$

Integrating this equation gives an expression for the decay of the parent:

$$N_A = N_{0A} * e^{-\lambda_A t} \text{ and } A_A = A_{0A} * e^{-\lambda_A t} \tag{1.14}$$

To determine the amount of nuclei the daughter has, one must take into account the radioactive decay and the radioactive growth from the decay of the parent nuclei:

$$\frac{dN_B}{dt} = \lambda_A N_A - \lambda_B N_B \tag{1.15}$$

Where the subscript B denotes the daughter isotope. Rearranging and taking the integral of both sides:

$$N_B = \frac{\lambda_A}{\lambda_B - \lambda_A} N_{0A} \left(e^{-\lambda_A t} - e^{-\lambda_B t}\right) + N_{0B} e^{-\lambda_B t} \tag{1.16}$$

Eq. 1.16 takes into account the amount of daughter nuclei existing at a reference time. If there is no daughter nuclei at the reference time, $N_{0B} = 0$, the rate growth of the daughter nuclei is dependent on the rate of decay of the parent nuclei:

$$N_B = \frac{\lambda_B}{\lambda_B - \lambda_A} N_{0A} \left(e^{-\lambda_A t} - e^{-\lambda_B t}\right)$$

and (1.17)

$$A_B = \lambda_B N_B = \frac{\lambda_A}{\lambda_B - \lambda_A} A_{0A} \left(e^{-\lambda_A t} - e^{-\lambda_B t}\right)$$

The ratio of λ_A to λ_B is the dominating factor when determining the growth of the daughter nuclei. There are three different possibilities for this ratio which is determined by the rate of equilibrium between the parent and the daughter: secular equilibrium, transient equilibrium, or no equilibrium.

1.4.2 Transient Equilibrium

Transient equilibrium occurs when the half-life of the daughter is less than that of the parent, however, it is not negligible. In this case, the activity of the daughter grows as the parent

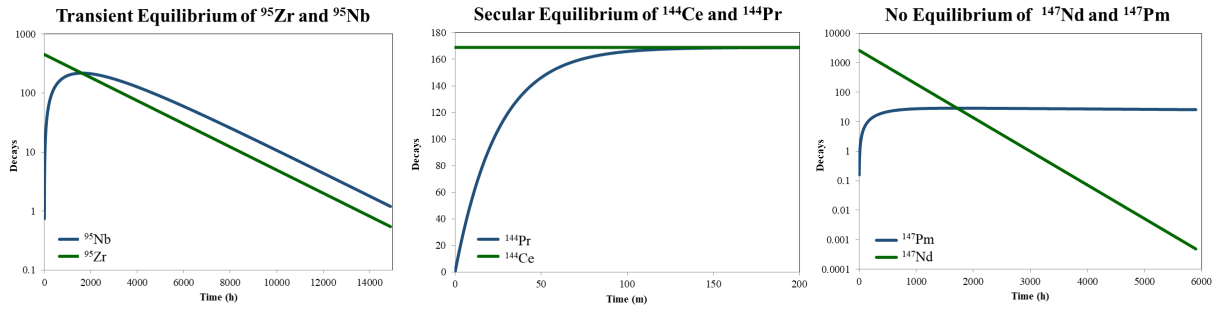

Figure 1.4: The possible types of equilibrium between parent and daughter isotopes. It is also possible for no equilibrium to occur between the pair. Equilibrium relationships are dependent on the relative half-life of parent and daughter isotopes.

decays. After some time, the activity of the daughter reaches a maximum value, which exceeds that of the parent. Once equilibrium is reached, both the parent and the daughter decay at the same rate with the activity of the daughter higher than that of the parent.

During transient equilibrium, the parent's decay constant is less than that of the daughter ($\lambda_A < \lambda_B$) and Eq. 1.17 reduces to:

$$N_B = \frac{\lambda_A}{\lambda_B - \lambda_A} N_{0A} \left(e^{-\lambda_A t} - e^{-\lambda_B t}\right) = \frac{\lambda_A}{\lambda_B - \lambda_A} N_A \tag{1.18}$$

Transforming Eq. 1.18 into activity by multiplying both sides by λ_B:

$$\lambda_B N_B = \frac{\lambda_B \lambda_A}{\lambda_B - \lambda_A} N_A \quad \rightarrow \quad A_B = \frac{\lambda_B}{\lambda_A - \lambda_B} A_A \tag{1.19}$$

Eq. 1.19 suggests that during equilibrium, the activity of the daughter is larger than the activity of the parent. Transient equilibrium is seen in the decay of ^{95}Zr ($t_{1/2} = 64\ d$) to ^{95}Nb ($t_{1/2} = 35\ d$).

1.4.3 Secular Equilibrium

Secular equilibrium occurs when the half-life of the parent is much larger than that of the daughter ($\lambda_B \gg \lambda_A$). In this case, the activity of the daughter quickly matches that of the parent, with each isotope contributing equal amounts of activity to the total overall activity of the sample. Over time, the activity of the parent isotope does not remarkably change ($N_{0A} = N_A$).

For an initially pure sample of the parent, the daughter has not yet grown in, $N_{0_B} = 0$. The half-life of the parent isotope is much larger than the sample reference time, $t_{1/2_A} \gg t$. The expressions: $e^{-\lambda_A t} \approx e^0 = 1$ and $\lambda_B \gg \lambda_A$; $\lambda_B - \lambda_A \cong \lambda_B$ reduce, resulting in a simplified decay equation for the daughter (Eq. 1.17):

$$N_B = \frac{\lambda_A}{\lambda_B} N_A \left(1 - e^{-\lambda_B t}\right) \tag{1.20}$$

When secular equilibrium is reached, the time of the sample is much greater than $t_{1/2}$ of the daughter isotope, ($e^{-\lambda_B t} \rightarrow\ e^{-\infty} = 0$), Eq. 1.20 reduces to:

$$N_B = \frac{\lambda_A}{\lambda_B} N_A \tag{1.21}$$

Transforming Eq. 1.21 into activity:

$$\lambda_B N_B = \lambda_A N_A\ \rightarrow\ A_B = A_A = A_{total/2} \tag{1.22}$$

While the number of nuclei of either isotope change, their respective activities of each remain constant and equal. Secular equilibrium is seen in the decay of ^{144}Ce ($t_{1/2} = 285\ d$) to ^{144}Pr ($t_{1/2}$ =17.3 m).

1.4.4 No Equilibrium

In the circumstance where there is no equilibrium, the $t_{1/2}$ of the daughter is much larger than the $t_{1/2}$ of the parent. As the parent quickly decays to zero, the daughter grows, reaches a maximum, and then decays at its own rate. There is no equilibrium established between the two and given enough time, the daughter will be the only remaining isotope in the decay of the source.

When the amount of time is much larger than that of the parent $t_{1/2}$ ($t \gg t_{1/2_A}$) and $e^{-\lambda_A t} = e^{-\infty} = 0$ simplifies, reducing Eq. 1.17 to:

$$N_B = \frac{\lambda_A}{\lambda_B - \lambda_A} N_{0A} \left(-e^{-\lambda_B t}\right) \approx N_{0A} \left(-e^{-\lambda_B t}\right) \tag{1.23}$$

No equilibrium between parent and daughter is seen in the decay of ^{147}Nd ($t_{1/2} = 11\ d$) and ^{147}Pm ($t_{1/2} = 2.6\ y$).

1.4.5 Successive Radioactive Decays

The previous equilibrium equations assume only a radioactive parent and daughter. In certain situations, there are multiple daughters that could be decaying within the source. The solutions to these equations require the use of the Bateman Equation[14,15], which follows the general explicit formula:

$$N_n(t) = \sum_{i=1}^{n} \left[N_i(0) * \left(\prod_{j=i}^{n-1} \lambda_j \right) * \left(\sum_{j=i}^{n} \left(\frac{e^{-\lambda_j t}}{\prod_{p=i,p\neq j}^{n} (\lambda_p - \lambda_j)} \right) \right) \right] \tag{1.24}$$

where n is the last isotope in the decay chain.

1.4.6 Radioactive Growth, Decay, and Measurement

In situations where an isotope is being created (such as in a nuclear reactor or particle accelerator) and decaying, both the growth and decay of the isotope must be examined. The radioactive isotope, A, is being created at a constant rate of R_A while also decaying with a rate constant, λ_A:

$$\frac{dN_A(t)}{dt} = R_A - \lambda_A N_A \tag{1.25}$$

Integrating both sides results in:

$$N_A(t_{irr}) = N_A(0)\, e^{-\lambda_A t_{irr}} + \frac{R_A}{\lambda_A}\left(1 - e^{-\lambda_A t_{irr}}\right) \tag{1.26}$$

Where t_{irr} is the time during which the radioactive ions are created. There is usually no starting radioactive material before the irradiation, $N_A(0) = 0$, and Eq. 1.26 reduces to:

$$N_A(t_{irr}) = \frac{R_A}{\lambda_A}\left(1 - e^{-\lambda_A t_{irr}}\right) \tag{1.27}$$

Which can rearrange to give the activity of the irradiated isotope:

$$A_A(t_{irr}) = R_A\left(1 - e^{-\lambda_A t_{irr}}\right) \tag{1.28}$$

As $t_{irr} \to \infty$ ($e^{-\lambda_A t_{irr}} \to e^{-\infty} = 0$), the maximum activity of species A depends entirely on R_A:

$$A_A = \lambda_A N_A = R_A \tag{1.29}$$

If the irradiation ends before the maximum activity has been reached, no new growth occurs while the isotope continues to decay. After a period of rest, t_{rest}, the activity will be proportional to the amount of time irradiated and the amount of time rested:

$$N_A = \frac{R_A}{\lambda_A}\left(1 - e^{-\lambda_A t_{irr}}\right)\left(e^{-\lambda_A t_{rest}}\right) \tag{1.30}$$

After a period of rest, the sample may be measured for activity. As it is continuously decaying, it is necessary to determine the number of decays during a time period, t_1 and $t_2 = t_1 + \Delta t$:

$$\Delta N_A = \int_{t_1}^{t_2} A_A \, dt = \int_{t_1}^{t_2} \lambda_A N_A \, dt = N_{0A}\left(e^{-\lambda_A t_1}\right)\left(1 - e^{-\lambda_A t_2}\right) \tag{1.31}$$

If we assume the number of original radioactive nuclei is the expression for the creation of those nuclei ($N_{0A} = \frac{R_A}{\lambda_A}\left(1 - e^{-\lambda_A t_{irr}}\right)$) and the end of the rest period is the beginning of the measurement ($t_{rest} = t_1$), we can obtain an expression for the number of disintegrations which were created, decayed, then measured over a set period of time.

$$N_A = \frac{R_A}{\lambda_A}\left(1 - e^{-\lambda_A t_{irr}}\right)\left(e^{-\lambda_A t_1}\right)\left(1 - e^{-\lambda_A t_2}\right) \tag{1.32}$$

Eq. 1.32 is an expression for the number of radioactive parent nuclei. If there also exists radioactive daughter nuclei, an expression for that can be determined in a similar way using Eq. 1.15:

$$\begin{aligned} N_B = &\frac{R_A \lambda_B}{\lambda_A\left(\lambda_B - \lambda_A\right)}\left(1 - e^{-\lambda_A t_{irr}}\right)\left(e^{-\lambda_A t_1}\right)\left(1 - e^{-\lambda_A (t_2)}\right) \\ &- \frac{R_A \lambda_A}{\lambda_B\left(\lambda_B - \lambda_A\right)}\left(1 - e^{-\lambda_B t_{irr}}\right)\left(e^{-\lambda_B t_1}\right)\left(1 - e^{-\lambda_B (t_2)}\right) \end{aligned} \tag{1.33}$$

1.5 The Need for Precision Measurements

Many fission products decay by emission of a β particle producing isotopes of the same atomic mass, but different elemental properties. These mass chains progress with well-known half-lives and, by measuring the longer-lived daughters of the parent fission products, one can calculate information about fission events indirectly.

Most β decays are accompanied by the further emission of a γ-ray as a large majority of these decays populate an excited state of the daughter. De-excitation to ground state results in the emission of a γ-ray. Measurements of γ-rays are a reliable way to identify the quantities of different long-lived radioactive isotopes present in a sample. Many of the radioactive nuclei of interest emit γ-rays at characteristic energies which can be detected with high energy resolution and limited background noise using high-purity germanium (HPGe) detectors. However, these γ-rays are only emitted in a fraction of the decays, and this fraction (known as the γ-ray branching ratio) must be known accurately to determine the total number of atoms present.

The γ-ray branching ratios (the fraction of decays in which a specific γ-ray is emitted) of many isotopes have been measured with high accuracy due to their simple decay scheme and the relative ease of the analytical measurements involved. However, some of the more complex decay schemes have large uncertainties due to the fact that these decays do not always yield a γ-ray. In many cases, the radioactive isotope decays directly to the ground state or decays to excited states that de-excite by internal conversion (where an atomic electron is ejected in place of a γ-ray). These "dark" decays where a γ-ray is not emitted will not be detected from a measurement based solely on the detection of γ-rays. As such, more detection information on each of the emitted particles is necessary in order to recreate an accurate depiction of the γ-ray branching ratios.

1.6 Difficulties Associated with Precision Measurements

Both γ-rays and internal conversion electrons (CE) can be measured relatively easily due to their distinct energies and interactions with matter. γ-rays are minimally attenuated in matter especially if the material is made from low Z elements. Heavy materials such as lead are often used to block γ-rays because of its high density and high atomic number. CEs, while charged and possessing mass, generally penetrate materials more effectively than β particles due to the lack of spread in their energy distribution. The attenuation of CEs in materials is well known because the energy they possess during emission is well known.

β particles present a difficult problem because their kinetic energies span from near zero to almost the total amount of energy released during the decay (Q value). During β decay, the Q value is the energy shared between the emitted β particle, $\bar{\nu}$, recoiling parent nucleus, and any γ-rays, x-rays, or CEs produced. The nuclear recoil energy is small compared to the energies shared by the β particle and $\bar{\nu}$ and is generally neglected.

Fig. 1.5 depicts a β spectrum showing a generic distribution of energies. For most nuclides with large Q values, the β spectrum looks similar to Fig. 1.5a. However, for nuclides with large nuclear charge and small Q values, the β spectrum looks more like Fig. 1.5b, where the most probable β energy occurs at much lower energies than the $E_{\beta_{max}}$ value. The difference in the shapes of the β spectra is due primarily to the Coulombic interaction of the positively-charged nucleus and the negatively-charged β particle. Detecting low-energy β particles is particularly difficult due to the high probability of interaction and absorption by the material surrounding the source.

An additional issue faced when detecting β particles has to do with the limitations of the electronics. Most systems are not ideal and have some noise associated to their operation. This noise level is generally small and can be minimized by imposing some electronic threshold that effectively blocks its noise interference. However, for detection of β particles, this

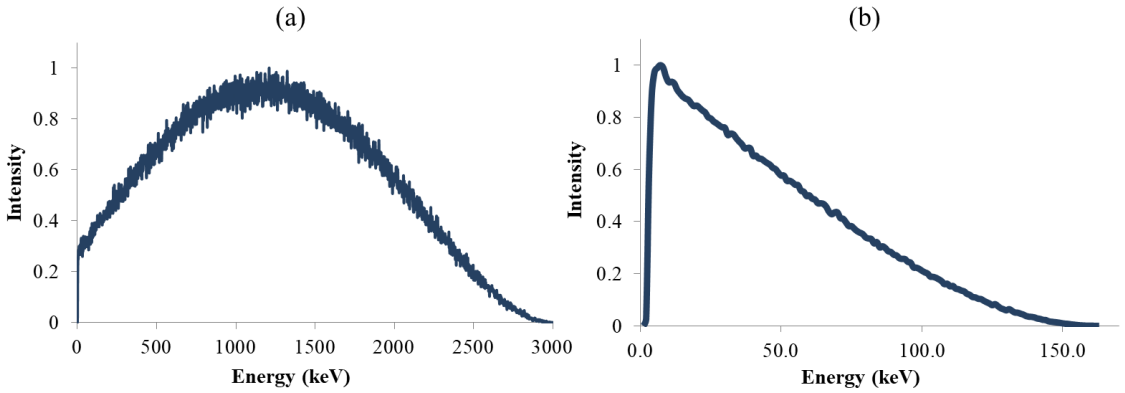

Figure 1.5: β energy spectra for (a) a high Q value decay and (b) a low Q value decay showing the relative spread and most probable β energies. For these spectra, a $Q = \sim$3 MeV results in the most probable energy being roughly 1/3 of the total energy of the reaction whereas a $Q = \sim$150 keV results in a most probable energy close to 1/30 of the total energy.

interference from noise has some overlap with the energy deposited from the β particle. The electronic threshold must be well-known and quantified so its effects are minimized.

Another consideration which arises from the measurement of β particles is determining the specific isotope which deposits the energy. The spread of possible energies associated to β decay make it challenging to determine its isotopic origin. If the source of decay is from a single isotope, the energy spectrum deposited can be assigned to the decay. If there are multiple isotopes associated to the decay of a source (such as radioactive parent and daughter), the resulting deposition of energy spectrum is a combination of the two and, without discrete energies associated to the decay, it is almost impossible to determine the contribution of the parent from the daughter. Furthermore, if there are unknown sources of radiation within the source (such as contamination from an unexpected isotope), the separation of contributions using solely the deposition of energy spectrum is challenging without further information.

1.7 Project Details

To gain an understanding of the γ-ray branching ratios and further reduce the uncertainties associated with these values to the $\sim$1% level, all of the decays (except for the $\bar{\nu}$) emitted from the source must be accurately measured. This involves detecting the emitted γ-rays, β particles, and CEs with high precision. The efficiency of the instruments involved must be controlled at the 0.5% level or better while also maintaining the uncertainty of the source and statistics to the same level.

For the purpose of confirming the method's precision, the β decay of ^{95}Zr is studied. ^{95}Zr is ideal to investigate systematic effects as its γ-ray branching ratios have been determined to 0.5% precision and it decays to ^{95}Nb, for which the γ-ray branching ratio is known to a precision of $<$0.1%. For the majority of the β decays associated to these isotopes, a single γ-ray is emitted allowing for source strength and branching ratios to be determined precisely from γ-ray spectroscopy. The half-life of ^{95}Zr ($t_{1/2}$ = 64 d) allows for sufficient time to perform measurements and optimize the experimental approach.

To prepare for the high precision measurements at the collaborating facilities, a production source is made using Texas A&M University TRIGA nuclear reactor by irradiating a mg-sized thin metal foil of isotopically enriched stable ^{94}Zr. This source is used to study the performance of the gas counter and identify potential systematic effects. While this method of source production can create ample quantities of the isotopes of interest, the purity of the source is not guaranteed as contaminates within the foil could activate to create levels of backgrounds which are difficult to characterize with high precision.

Production of high-purity sources were created at the CARIBU facility at Argonne National Laboratory using radioactive beams of mass separated fission products implanted on thin foils. The CARIBU mass separator has demonstrated a mass resolution of $\Delta M/M \sim 10^{-4}$

which is ideal to maintain source purity. A 0.7 cm diameter aperture located in between the beam and the foil will ensure a source implantation geometry that is well-controlled.

Measurement of the γ-rays will be performed at Texas A&M University using their HPGe. Their system is uniquely suited for this measurement because of the low uncertainty associated to their γ-ray detection efficiency. The HPGe detector response has been well characterized and understood which is imperative to keep the total uncertainty associated to the measurement low.

To properly account for the β particles and CEs emitted from the radioisotope, a custom gas counter and source holder was developed. The source holder consists of an ultra-thin foil floated over open space on which the radiation is placed. This minimizes the dead layers between the radiation and the active detection volume. The sample holder is placed inside the chamber of the gas counter allowing for 4π geometry. This detector design has been optimized for low-energy electrons ($\sim$keV energies) resulting in nearly 100% efficiency for detection. Measurement of the source using this gas counter will be performed at Texas A&M University alongside measurement of the emitted γ-rays.

To have confidence in this custom-made, 4π gas counter, simulated detector responses have been actively studied using the program GEANT4. Through the collaboration with LLNL, a custom code is used to generate transition-specific β decay events which produce isotropically-emitted β particles with an allowed energy spectrum. The outputs from the simulations are used to determine source foil material and thickness that results in optimization of detection efficiency. Furthermore, simulations are compared with experimental measurements to determine any issues with gas counter operations.

Chapter 2

Experimental Approach

This method has been applied to several isotopes to confirm the validity of the procedure and its application. As such, the experimental measurement and analysis is quite similar for each isotope. The basic format consists of: (1) create the sources at ANL using the CARIBU facility, (2) transfer the source to TAMU for measurement of the emitted β particles, CEs, and γ-rays, (3) compare results with simulated values using GEANT4, and (4) analyze the data for γ-ray branching ratio values.

2.1 Nuclear Reactor-Produced Test Sources

It is possible to make ^{95}Zr using a nuclear reactor. A major benefit of producing these radioactive sources is to test the operational capabilities of the gas counter using the same isotopes as the final method. These test sources not only allow for initial gas counter characterizations, they also provide a chance to compare the gas counter response with simulated results using a different geometry of radioactive source. A nuclear reactor has the potential to produce more active sources in a shorter amount of time compared to the source production

at CARIBU. Some of the drawbacks of a reactor made source are the relative thicknesses and the potential contaminates created as a result of neutron bombardment.

To produce ^{95}Zr test source, the TAMU nuclear reactor was used. It is a Training, Research, and Test General Atomic (TRIGA) homogeneous solid-type reactor that operates at 1.0 MW with a neutron flux between 1.0×10^{12} $^{neu}/_{cm^2 s}$ and 1.4×10^{13} $^{neu}/_{cm^2 s}$. This relatively large neutron flux range allows for less irradiation time to produce high-activity sources.

The TAMU nuclear reactor works on the principal of a sustained, neutron-induced, fission chain reaction of ^{235}U. A mixture of ^{235}U/^{238}U and Zr-H make up the nuclear fuel. This TRIGA reactor is built in such a way as to be inherently safe. The safety feature arises from interactions between the neutron and hydrogen atom; as the fuel increases in temperature, the continued fission chain reaction becomes less efficient. As such, potential nuclear meltdowns experienced by commercial nuclear reactors are not likely to occur. Control rods made of boron-impregnated carbon are used to control the chain reaction. Boron is excellent at capturing free neutrons, which would have otherwise continued to create more fission events.

Different isotopes can absorb neutrons into the nucleus, which results in the same element (same Z number), but a different isotope (different number of neutrons). In most cases, this absorption of a neutron changes the isotope from a stable nucleus into a radioactive one. This process, known as neutron activation analysis (NAA), is an effective method for quantifying material at the isotopic level. A nucleus' ability to absorb a neutron is known as the neutron cross section (σ). The neutron cross section is highly dependent on the incident energy of the neutron. Research reactors have the ability to operate at different power levels. The power at which the reactor is operated is directly proportional to the neutron flux (ϕ) of a reactor, or the number of neutrons per square centimeter per second. The higher the neutron flux, the more neutrons are available for absorption in material.

A theoretical calculation of the amount of activity created in a specific material can be determined by:

$$A = N * \sigma * \varphi * \left(1 - e^{-\lambda t_{irr}}\right) \tag{2.1}$$

Where $N = \frac{w*f*N_A}{MW}$, N is the number of elemental molecules in the sample, w is the weight of the element in grams, f is the fractional abundance of the parent isotope, N_A is Avogadro's number, MW is the molecular weight of the parent isotope, σ is the cross section of the parent in cm^2, φ is the neutron flux in ${}^{neu}/_{cm^2 s}$ which is specific to the reactor being used, λ is the decay constant of the daughter, and t_{irr} is the total time the sample is to be irradiated. The specific activity calculated is for the production of one isotope. If there are other possible sources of activity within the sample, this calculation is required for each, with the total sample activity being a summation of the individual radioactive isotope activities.

2.2 Fission Fragment Collection at the CARIBU Facility

In an effort to further study low energy nuclear physics, the Californium Rare Isotope Breeder Upgrade (CARIBU) is an addition to the Argonne Tandem Linac Accelerator System (ATLAS) located at Argonne National Laboratory (ANL). ATLAS is a linear accelerator for stables isotopes ranging from protons to uranium. CARIBU increases the capabilities of ATLAS to include low-energy, short-lived, neutron-rich isotopes[3]. These isotopes are produced as fission products from the spontaneous fission of ^{252}Cf. The basic layout of the CARIBU facility consists of a fission source to supply the fission products, an RF gas catcher to extract fission product into a beam, and a high-resolution magnetic separator to isolate the isotopic mass of interest.

^{252}Cf ($t_{1/2} = 2.64\ y$) undergoes spontaneous fission 3.1% of its total decays. The energy distribution of the fission products of ^{252}Cf have an averaged mass yield centering on $A =$

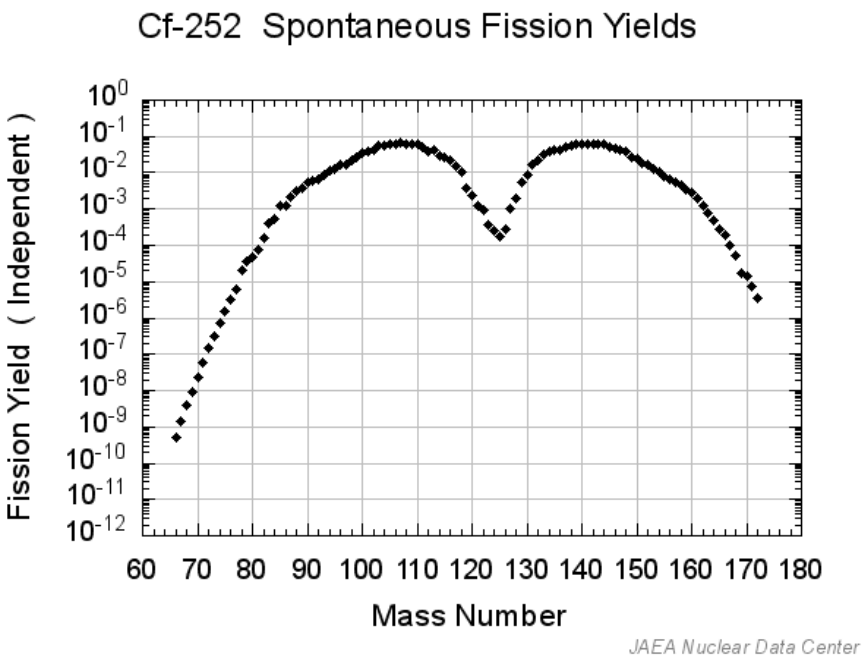

Figure 2.1: Fission product yields for ^{252}Cf showing mass number versus the probability of yield[2].

107 and 143 (Fig. 2.1). The source is electro-deposited on a flat, 0.1 *in.*-thick tantalum backing supported on a source holder[16], which restricts the solid angle of emission to 2π.

After spontaneous fission, the emitted fission products are energetically slowed in a gold degrader foil and then in high purity helium. As the fission products hit the helium ions and slow within the gas catcher, they lose energy and collect electrons released from helium. Once they have lost enough energy, the fission products can no longer extract electrons from helium due to the high binding energy (28.3 MeV) and remain in a +1 or +2 charged state (dependent on the second ionization potential of the fission product). These thermalized fragments are quickly guided towards an extraction nozzle using a combination of DC and RF fields[17]. The quick transportation reduces the time spent radioactively decaying and also minimizes the interactions between fission products and gas impurities and/or collisions with the inner walls of the chamber. Once the ions are within *mm*-distance of the nozzle, the flow of gas transports the ions from the gas catcher to a radio-frequency quadrupole (RFQ).

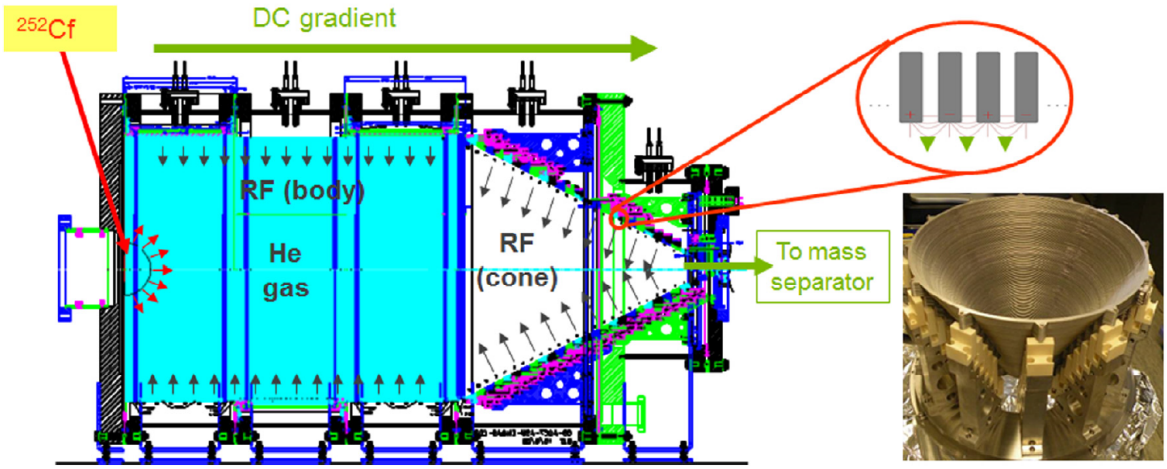

Figure 2.2: Simplification of the gas catcher used at CARIBU. Fission products from spontaneous fission of ^{252}Cf interact with the He gas and are directed toward the RF cone, which concentrates the ions into a beam[3].

At this stage, the ions are being directed by the large gas flow escaping the gas catcher. The relatively high pressure at the nozzle effects the acceleration of the ions. In order to achieve good acceleration, the helium gas must be pumped out and the pressure reduced. This is performed by guiding the ions into two sections of RFQ coolers which serve to focus and accelerate a charge particle beam while pumping out the helium and decreasing the pressure. The ions are concentrated into a beam through electrostatic acceleration to 50 keV which help to focus the ions and reduce straggling. Gas collisions within the RFQ serve to cool the beam so that the energy spread is below 1 eV and a transverse emittance of 3π *mm rad* at 50 keV[18].

Once the fission fragments are released from the gas cooler system, they are transported into a high-resolution isobar separator[19]. At this stage, the ions that make up the beam are the full range of emitted fission products with masses proportional to their fission yield for ^{252}Cf. It is necessary at this stage to impose a mass restriction to select the product of interest for experiments. Due to the low energy spread and low emittance of the incoming beam, a magnetic high-resolution isobar separation with a mass resolution of >20,000:1 is achievable with transmittance of >95%. The output at this stage is a purified beam of the

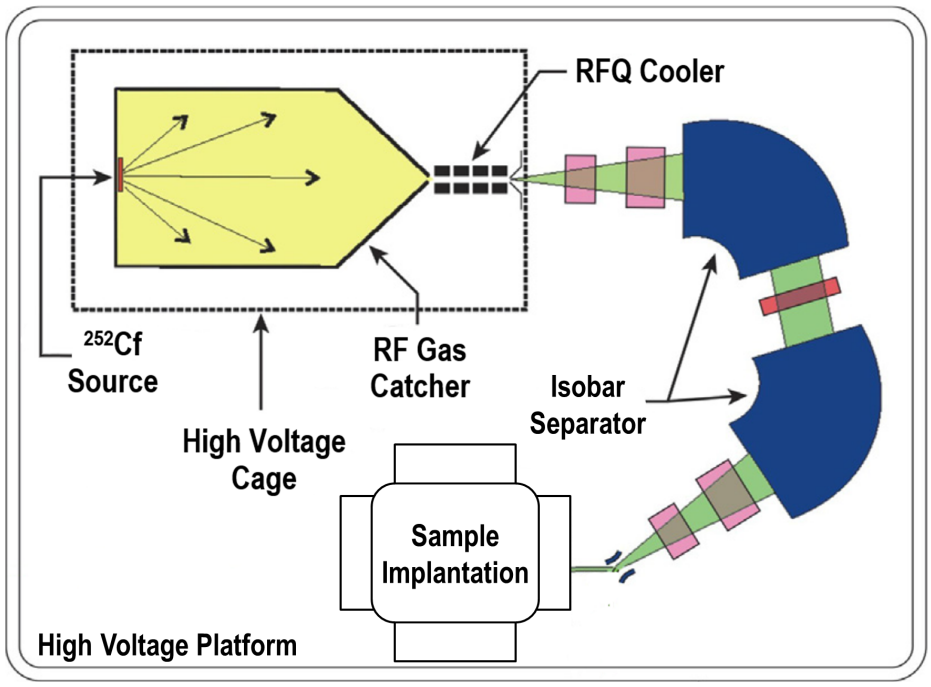

Figure 2.3: A simplified picture of the components that make up the beam line. Source implantation occurs shortly after beam separation in order to achieve the highest intensity of ions possible[4].

selected mass. The byproducts of the isobar separator, or those ions with a different mass than selected, are kept within the separator and are not transmitted within the beam.

Each of the described components of the CARIBU facility are located on top of a large 200 kV high-voltage platform (shown in Fig. 2.3). This platform helps to stabilize the voltage being supplied to the different systems. All of the excess radiation from the isobar separation of the fission products is contained on this platform, with only the mass of interest able to continue on pass the mass separator. At the end of the beam line shown in Fig. 2.3, the experimental setup is positioned to stop the beam and implant the ions onto the sample foil.

The sample implantation site in reference to the CARIBU beam line is shown in Fig. 2.4a and the setup of the implantation and foil placement is shown in Fig. 2.4b. The last attachment bolted to the end of beam line is a four-way, six-inch aluminum cross which maintains the vacuum of the system and supports the sample foil. This cross has four openings for the

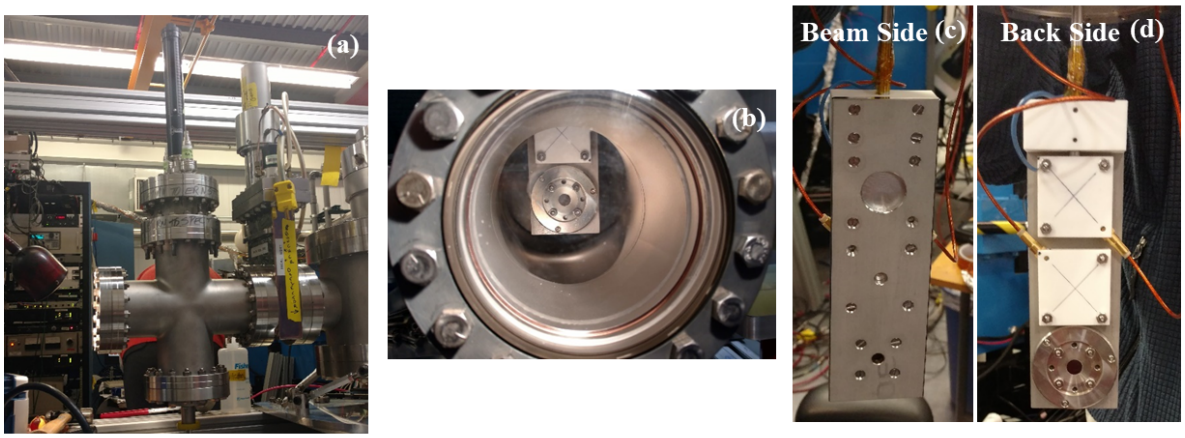

Figure 2.4: (a) Placement of the cross on the beam line. The arm which holds Si detectors and source foil fits in at the top. (b) Looking directly at the beam on the backside of the cross, one can see the foil positioned in the path of the oncoming beam. The arm that fits into the cross is shown for the side that faces the beam (c) and the side that faces away from the beam (d).

purpose of: connection to the beam line, connection of a vacuum pump for a controlled pump down to low vacuum pressure, connection of a ladder assembly supporting the diagnostics and sample foil, and a viewing station at the far end of the beam to verify the sample foil remains intact throughout placement and collection.

The mass separated ions are implanted on an ultra-thin carbon foil supported by the aluminum cross. The foil has a thickness of 40 $\mu g/cm^2$ floated on an aluminum sample holder. This holder is screwed onto a ladder assembly which is then bolted onto the top of the aluminum cross structure. The ladder assembly, shown in Fig. 2.4c and Fig. 2.4d, supports two silicone surface barrier detectors and the aluminum holder with the carbon foil. The ladder assembly has the capability of lateral movement of the support structure while the beam is in operation. The side of the ladder which faces the beam has one 30 mm and two 7 mm apertures used to detect and focus the beam into a specific region where the highest implantation can be achieved.

Small aluminum sheets are placed in between the beam and silicone detectors so as not to contaminate or damage the Si detector material. As ions are implanted onto the aluminum sheet in front of the silicone detector, the β particles are counted and an estimation of the ion collection rate is calculated. Ions are initially detected using the top most detector with the 30 mm aperture. The second detector, with the 7.0 mm aperture, is used to focus the beam both vertically and laterally. Once the beam has been concentrated, the target foil, with a 7.0 mm aperture, is moved in front of the beam to collect the ions. The aperture in front of the target foil restricts the implantation of ions to the center of the carbon foil. The connection of the ladder assembly to the aluminum cross is equipped with a linear motion vacuum feed through to allow signal cables into the beam line vacuum system so that connection to the silicone detectors is possible.

Once the assembly ladder is bolted to the top of the aluminum cross, the isolated system is pumped down to low vacuum (10^{-2} $torr$) through a throttling valve for the purpose of fine control of air flow rate. Well-controlled pumping is necessary so that the delicate carbon foil does not rupture from abrupt changes in pressure. Once low vacuum has been reached, a gate valve introduces the cross system to the rest of the beam line, which is under high vacuum (10^{-6} $torr$). This relatively large change in pressure has been experimentally verified to cause no harm to the foil.

An HPGe detector is positioned towards the middle of the aluminum cross on the outside of the implantation site to monitor the beam as the ions are collected. Before the ladder assembly is attached to the cross on the beam line, a quick efficiency calibration of the detector is performed. Monitoring the beam confirms the correct mass is being transported through the beam and that a consistent beam intensity is maintained. Post beam implantation, these monitoring spectra are used to identify the existence of any contamination from isotopes that are not the desired mass. Direct monitoring of desired fission product isotopes (^{95}Zr, ^{144}Ce, and ^{147}Nd) are not practicable as their activities are generally not large enough to

detect in the short time periods after the fission of ^{252}Cf. Instead, isotopes of the same mass further up the mass chain (parent isotopes) are monitored as they have shorter $t_{1/2}$, making their emitted activity more intense. These parent isotopes will eventually decay into the desired isotope given enough time.

Once the implantation of the ions onto the carbon foil is complete, the cross is isolated from the beam line and slowly returned to atmospheric pressure. A small rest time between end of implantation and opening of the beam line is taken to let some of the more active isotopes decay. Once the cross is opened, the ladder is removed from the cross and the aluminum holder supporting the carbon foil is removed from the ladder. The source is delicately packaged so as not to damage the foil then shipped to Texas A&M for measurement.

2.3 TAMU - Source Measurement

In order to reduce uncertainties in the measurement of γ-ray intensities to the $\sim$1% level, precision instrumentation is necessary. A custom built 4π gas-flow proportional counter is used in coincidence with an HPGe that has an absolute efficiency that is known to better than 0.2% over the energy range 50-1400 keV[20,21,7,22,23]. Setup of these systems are optimized before each measurement and care is taken to maintain the settings over the duration of the experiment.

2.3.1 HPGe Detector Operation

Several instruments have been developed over the years to detect γ-rays with high efficiency and good resolution. By far the most commonly used for γ-ray spectroscopy is the high purity germanium (HPGe) detector. The basic design consists of a semiconductor germanium crystal under the influence of a bias cooled to liquid nitrogen temperatures. The ionizing

radiation produces free electron-hole pairs by means of γ-ray interactions with matter. The number of electron-hole pairs is proportional to the energy deposited in the crystal. These crystals also have some dead layer of lithium diffusion surrounding the crystal for the purpose of assisting the transportation of electrons and holes to the contact.

Detection of γ-rays occurs through interactions with matter by which there are three main processes: photoelectric effect, Compton scattering, and pair production (Fig. 2.5). Each of the processes result in partial or total deposition of energy of the γ-ray to electron. The photoelectric effect explains γ-ray absorption within electrons in orbital around a nucleus. If the energy of the γ-ray exceeds the binding energy of the electron, it is possible for the electron to be ejected from the atom. This process dominates low energy γ-rays. For higher energy γ-rays, Compton scattering is the most prominent interaction with matter. The energy of the γ-ray is inelastically scattered by a charged particle (usually an electron). The original angle of travel of the γ-ray is altered and some energy is deposited into the charged particle in the form of its recoil. The resulting γ-ray has less energy than the incident γ-ray. Finally, for γ-rays with several MeV of energy or greater (>1022 keV), it is possible for pair production to occur whereby the energy of the γ-ray is directly converted into matter in the presence of an electric field of a heavy atom. The process of pair production does not occur to a large degree for the isotopes of interest and is not further discussed.

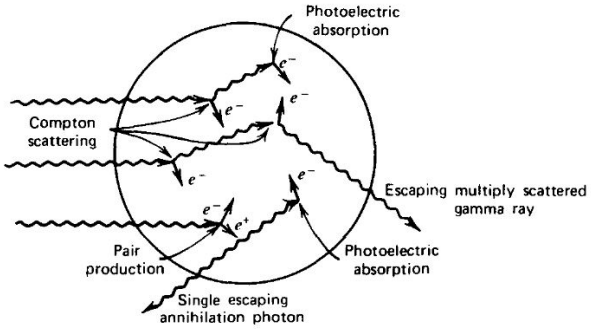

Figure 2.5: Interactions of γ-rays with the germanium crystal inside the HPGe detector[5].

The density of the crystal is such that total absorption of the γ-ray is readily achievable for energies of up to a few MeV[6]. It is possible for γ-rays to escape the crystal and deposit a

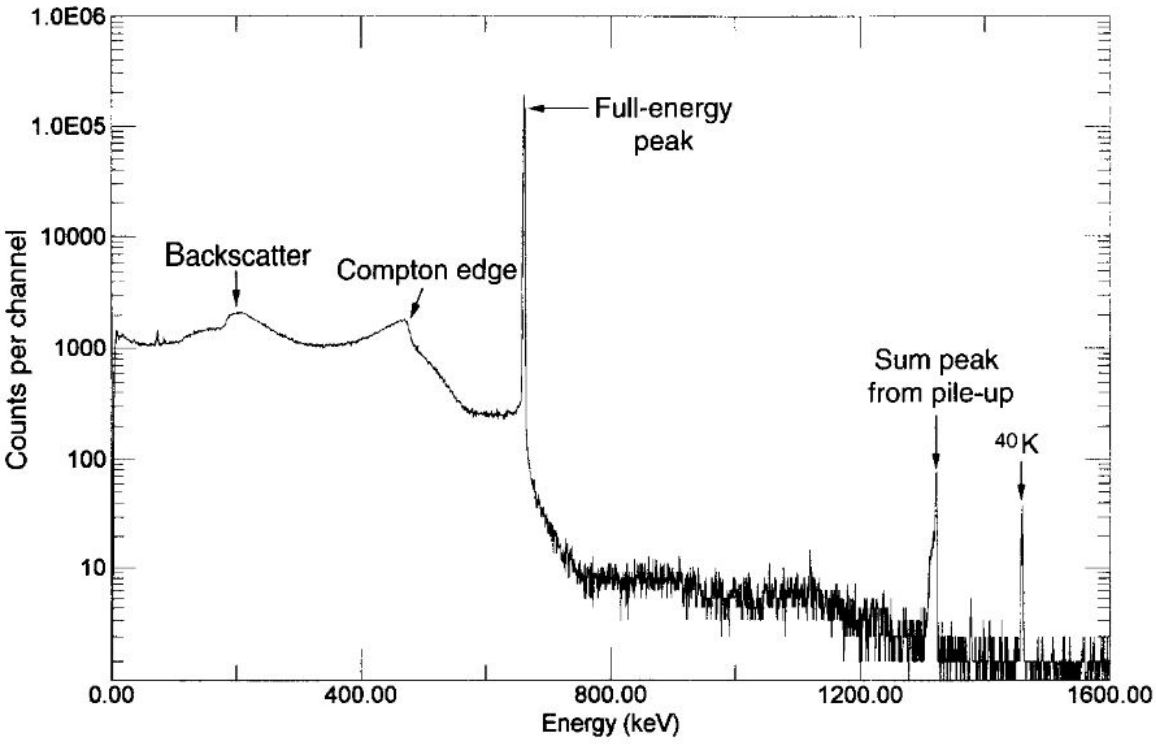

Figure 2.6: Characteristic features of a γ-ray spectrum using a ^{137}Cs source[6].

fraction of its total energy. This fraction of energy deposition inside the crystal makes up the Compton continuum commonly seen in a γ-ray energy spectrum.

Fig. 2.6 shows the main features of a γ-ray energy spectrum for the isotope ^{137}Cs, which decays by emission of a single 662 keV γ-ray. Pair production is not possible as the energy of the γ-ray is less than the required energy. The full energy peak is identifiable by the peak at 662 keV whereby the full energy of the γ-ray was deposited and collected in the Ge crystal. The Compton continuum is seen as the background from low energies to just below 662 keV. Those γ-rays that scatter (depositing the maximum energy corresponding to a scattering angle of 180°) then escape the crystal are identified by the Compton edge. The backscatter peak is a result of γ-rays which have scattered from an external material surrounding the detector (such as shielding) then entered the crystal. This backscatter peak is broad and generally in the vicinity of 200 - 250 keV[6]. Several other peaks can be seen at energies higher than 662 keV as a sum peak from pulse pileup and a ^{40}K peak. The sum peak is a

result of two γ-rays entering the detector at similar times, which combine together to create a total energy deposition twice larger than expected (662 + 662 = 1324 keV in the case of ^{137}Cs). The higher the activity of the source, the higher probability multiple decays enter the detector at similar times producing this sum peak. Finally, sources of background γ-ray radiation are readily found in the environment (^{40}K and uranium / thorium decay chains). These can mostly be shielded against using high Z material such as lead or employing shorter count times.

2.3.2 HPGe Setup

The instrument used for measuring γ-rays for this experiment is an EG&G ORTEC Gamma-X HPGe, a coaxial type detector with an active volume of 280 cm^3 operating at -4.3 kV (Fig. 2.7a). A n-type Ge semiconductor is mounted horizontally and is encapsulated by an aluminum housing with a Be window used for measuring γ-rays with low energies. The set of electronics used to characterize the pulses are: an attached pre-amplifier mounted on the HPGe, a Tennelec spectroscopy amplifier (TC-249), and an Ortec TRUMP 8k/2k analog-to-digital converter card controlled by MAESTRO software.

Researchers at Texas A&M have devoted a large amount of time to determining the efficiency curve associated with their HPGe using both experimental and Monte Carlo techniques[20,21,7,22,23]. Thirteen individual sources with ten isotopic decays were used with activities between 2 and 47 kBq to perform the experimental determination of the detector efficiency. Monte Carlo calculated efficiencies were determined by adjusting physical parameters (based on direct measurements of the detector's physical properties) in order to agree with experimentally determined efficiencies. As a result, detector efficiencies for a specific energy and source geometry can be determined precisely over a large energy range. Fig. 2.7b

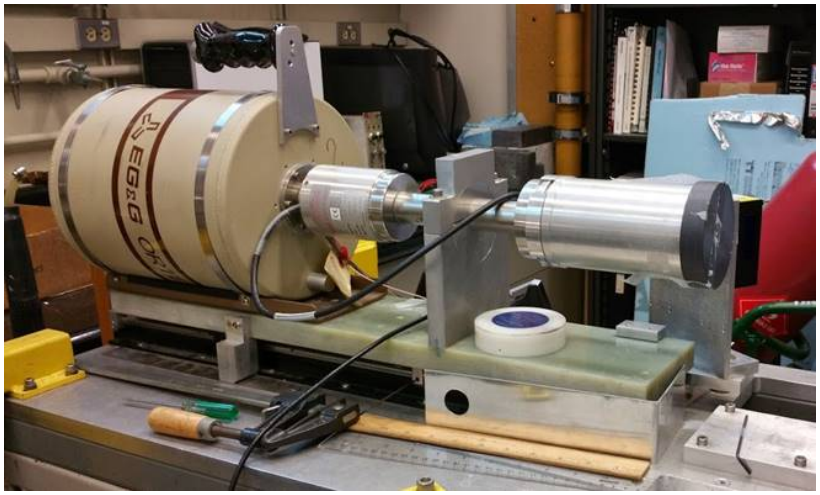

(a)

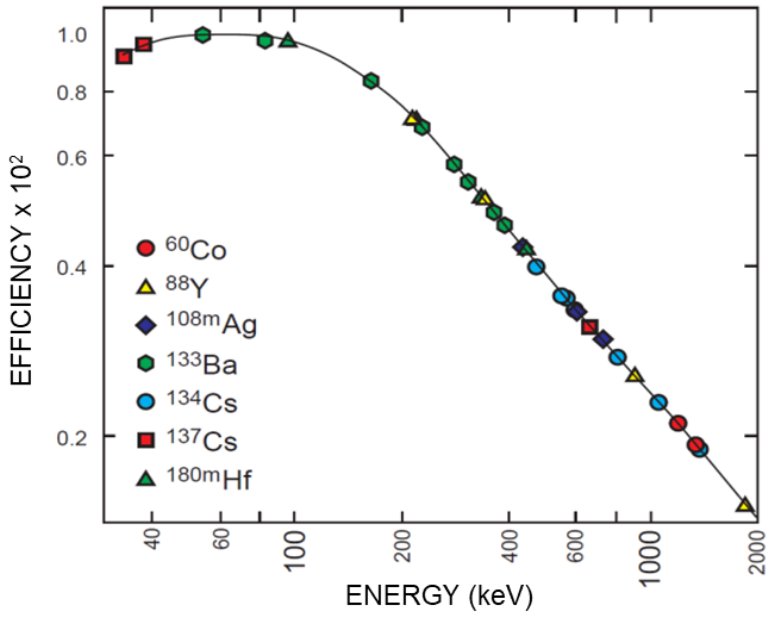

(b)

Figure 2.7: (a) Texas A&M meticulously-calibrated HPGe detector used to measure γ-rays with high precision. (b) Full energy peak efficiency as a function of γ-ray energy of the TAMU HPGe detector[7].

show both the experimental (points) and simulated (solid line) detector efficiency over the range of 40 – 2000 keV.

For each experiment, the room background radiation was measured. As there are others who perform research within the same building, the background radiation associated to the

location may differ over time. Generally, a background performed at the beginning and end of the experimental measurement is preferable to verify its stability over the length of the measurement. The length of the background measurements should be equal to or longer than the length of the source measurement as this helps to reduce uncertainties associated with comparisons between the source and background γ-ray spectra.

2.3.3 Gas Counter Operation

Different forms of radiation require instrumentation which can accurately detect and measure with high certainty. While the HPGe is used to measure the γ-rays, the gas counter is used to measure the emitted β particles and CEs. Of particular importance are the energies at which the radiation is emitted. For β particles with a spectrum of energies ranging from the maximum energy emitted in the decay down to near zero, the instrumentation greatly relies on being effective over a large range.

As mentioned, the nature of β particles are to interact with surrounding matter due to their -1 charge and mass. Coulombic and collision interactions result in deposition of energy to the point of absorption within a material. As such, their travel distance within air is several centimeters and is greatly dependent on the initial β particle energy. This distance reduces greatly when the β energy is low or when the density of the material they travel through is high.

As a charge particle passes through a gas, the energy released occurs primarily through ionization (Fig. 2.8). The electron is accelerated toward the positive anode wire while the ion is attracted to the detector housing which serves as the cathode. The accelerated electron will further ionize other gas particles creating an avalanche of electrons toward the anode wire.

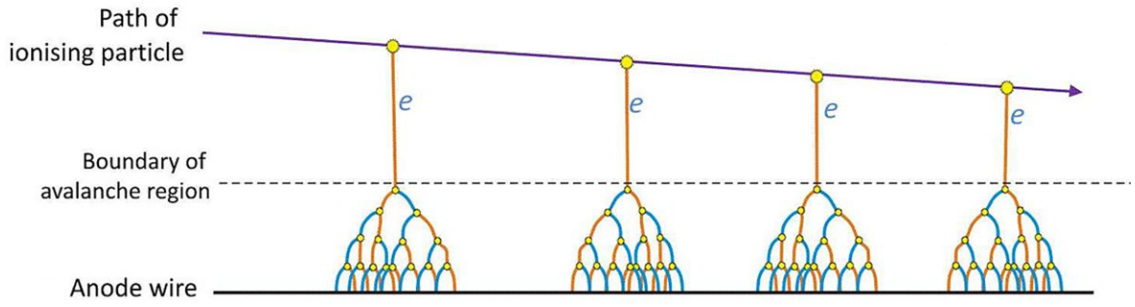

Figure 2.8: The pathway and interactions of an ionizing particle through detection gas in the presence of a bias.

The gas used for these experiments is methane because of its relatively unresponsive nature towards γ radiation. Emitted γ-rays could directly cause ionization in the fill gas or produce electrons through interactions of the wall material by way of the photoelectric effect. These direct interactions could produce electrons which get accelerated toward the anode, causing further gas multiplication not associated to direct emission of β decay. Methane's interaction with γ radiation produces minimal secondary radiation as it preferentially absorbs the radiation rather than emit it. As such, methane is commonly used as a quench gas to prevent further interactions of γ-rays with detection systems. Methane's ionization potential at room temperature is between 12.64 and 14.34 eV[24] (depending on the level of ionization) which readily occurs in the presence of $\sim$keV β interactions.

For the purpose of this experiment, the gas counter is operated in the proportional region. The energy deposited in the gas from incident radiation is proportional to the signal generated by such an event. Operation in this region allows for the collection of radiation energy information. Below the region of proportionality, it is possible for the electrons to recombine with the ionized gas resulting in a diminished signal compared to the energy deposited. Above the region of proportionality, excessive ionization occurs causing the entire volume to become charged instead of distinct point-like charges. This method of operation is used by Geiger counters and supplies limited energy information. To determine the optimum region of interest where proportionality takes place, a voltage plateau can be determined by in-

creasing the bias and measuring the resulting detector response to radiation. The optimum voltage for the system is determined to be the voltage that corresponds to the center of the plateau region.

Other attributes of the gas counter is its 4π design and gas-flow nature. The radioactive source is placed in the center of the active volume of the detector giving a 4π geometry for detection. The system uses gas that is constantly flowing through the detection space at atmospheric pressure. The gas purity and integrity is maintained as it is actively being replaced by fresh gas. These design choices minimize material interference between the radiation and active volume of the detector as the source is in direct contact with the detection gas. It also maintains stability of the detector response over time by eliminating gas degradation.

2.3.4 Gas Counter Setup

Design of the 4π gas counter is largely based upon designs from Koslowsky *et al*[25,26]. The detector is constructed from a block of oxygen free copper and has two identical sides. Fig. 2.9 shows a schematic of the detector from the front and side. From the front view, the middle set of dotted lines shows the support structure for the anode wires with the gas intake and exhaust on either side. Both sides of the detector are similar in design. An inlet and outlet are found on both sides of the chamber so as to reduce the movement of gas through the fragile foil. The gas exhaust diameter is 0.125 *in.* while the inlet is a smaller 0.016 *in.* so as to restrict the amount of air allowed in to the system.

The chamber is 1.438 *in.* in diameter and has a length of 2 *in.* in total. Two windows of 12.7 μm Havar are located on either side of the chamber so as to reduce the interaction of γ-rays escaping from the foil to the outside of the chamber. The windows can be removed from the detector body to allow for precision positioning of the source-to-HPGe distance.

The windows are screwed into place and sealed with rubber o-rings. Two SHV connections are located at the top of the detector. Each side can be operated independently so as to determine the detector response from either side or the signals can be summed together to measure the total detector response.

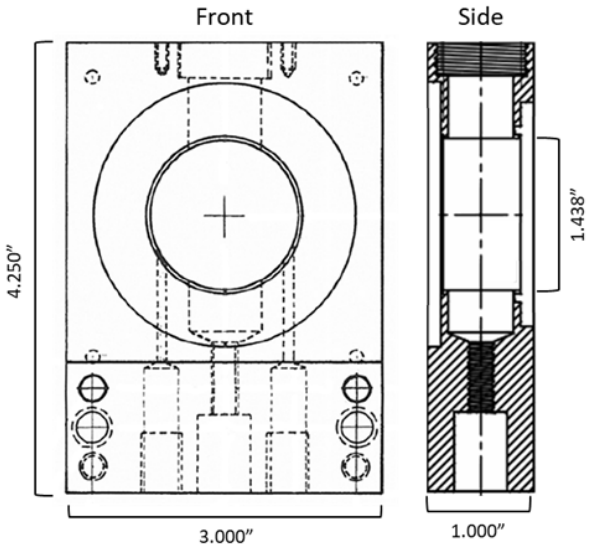

Figure 2.9: Schematic of the gas counter system.

Methane gas flows throughout the chamber at 1 atm. Methane was chosen for its relative insensitivity to γ-rays and acceptable gas gain when in the presence of β particles[27]. Methane is also an effective gas because of its nonpolar quality; it will not greatly interfere with avalanche electrons. The benefit of a gas flow detector is the low threshold which can be achieved, the consistent purity of the gas being used, and the prolonged lifetime of the system[6]. Gas continuously flowing through the detector reduces the chance of external impurities (such as oxygen) which might have high electron affinities and cause spurious pulses. If necessary, the detector can be opened, cleaned, and restored to original operating conditions without loss of quality to the system. A low inlet air flow rate is used to reduce the possibility of introducing dust that may be residing inside the inlet tubes. The rate of gas flow is determined by a regulator set to 1 cm^3/min and is generally set to exhaust at a rate of one bubble per second in water. Swagelok fittings and 1/8 inch vinyl tubing are used for both inlet and exhaust.

Gold-plated tungsten wires, 12.7 μm diameter, are suspended in each chamber supported by Teflon inserts. Tungsten is known to be quite strong as a metal, but it is brittle which causes small differences in the diameter over the length of the wire. This causes inconsistencies of

the uniformity of the electric field strength. Plating the tungsten wires with gold results in a more uniform diameter along the wire and produces an electric field strength that does not vary much over its length. Teflon inserts which support the anode wire serve to insulate the wires from the copper housing and help to maintain the airtight seal inside the chamber.

The anode wire is difficult to handle and replacing it is challenging. The best way to manipulate the wire into position is to attach it to a larger, more rigid wire ($\sim 0.1\ mm$ in diameter) so it can be thread through the small Teflon holes on both the bottom and top of the detector. A small ball of solder is placed on the end of the anode wire to act as the stopper to hold it in place within the bottom Teflon insert. The anode wire is measured for length of the chamber and is guided by the thicker wire through the top Teflon insert. This larger wire makes up the SHV connection at the top of the detector. Once the anode wire is fully threaded through the chamber, it is gently pulled tight then held in place with solder. A tight wire helps to maintain a uniform electric field inside the chamber. Finally, silver epoxy is used to fully stabilize the wire in place. An SHV connector is soldered to the thicker guide wire and the SHV assembly is screwed in place. Once the epoxy has been fully cured, the anode wire is cleaned with acetone and a soft paint brush so as to remove any debris that collected on the wire. A microscope then examines the wire for any final debris. The inside chamber and windows are cleaned with acetone. The system is then reassembled and ready for use.

Figure 2.10: (a) A source holder that fits into (b) each half of the detector creating a sealed system (c).

The source holder (Fig. 2.10a) slides into the center of the chamber and places pressure on two rubber o-rings which create an airtight seal between the two halves of the detector (Fig. 2.10b,c). The source holder is an aluminum frame with a 1.0 cm aperture in the center to support the radioactive foil. This center aperture is surrounded by smaller holes for the purpose of equalizing gas pressure on either side of the holder and minimize air flow through the foil. The source holder was designed to be used with a metal foil supported by small grid wires or with a carbon foil floated on one side of the holder. The source holder was designed such that it could be used both inside CARIBU during implantation of radioactive ions then placed inside the gas counter with little alteration. The holder also serves to support the carbon foil as it is shipped cross country without it rupturing in transit.

Once the gas counter has been cleaned, preparation for the each measurement largely follows the sample protocol: begin the flow of methane gas through the system for at minimum 6 h, introduce voltage at 0.5 kV steps each for about 3-6 h, leave the detector voltage at 3.0 kV for at least 12 h to fully condition and burn any remaining debris or oils, and reduce the voltage to operating voltage for 3 h. Once finished, the detector is ready to use. In general, the longer the system has methane flowing and voltage applied, the more stable the detector response is. Newly strung anode wires and chambers are generally degassed and conditioned for longer periods of time due to oils which may still reside on the wire or walls of the chamber. After each changing of the sample holder (to introduce a new source) or measurement of source-to-HPGe distance (requiring the windows to be removed), the detector has to go through a similar conditioning experience with slightly varying times to restore the system to operation.

One of the best ways to determine the operational reliability of the gas counter is to measure its response to radiation at different voltages. This is useful for identifying its optimal operating voltage for the measurement and its stability over its plateau range. Many factors contribute to the specific operating voltage for the measurement such as temperature, length

of conditioning, thickness and type of anode wire, cleanliness of chamber, etc[28,29]. A sign of potential issues with the detector can be seen by measuring the stability of the plateau region. The level of change in voltage over a 100 V region can be a sign of leaks in the system, unstable voltage supply, high electronic threshold setting, etc. A stable region where the difference in count rate over 100 V is less than 0.5% is the ideal detector response[30].

The electronics used in each of the experiments are also based upon the system used by Kolowsky et al[25,26]. The individual signals are summed and sent to a Philipps Scientific (Model 6950) fast current pre-amplifier, a fast filter amplifier (Ortec 579), a 100 MHz lower-level discriminator (Ortec 436), a non-retriggerable gate generator (Leroy 222 N), and a CAMAC based multiscalar (Leroy 3521A). This system has been well tested and has been in operation for precision half-life measurements[31,32,33]. Gain settings and discriminator levels were changed for each experiment and optimized for the specific operating voltage.

Throughout the experiment, a measurement of the gas counter background was taken to verify its consistency over the different source changes. This was also a check to confirm the lack of radioactive particles left within the chamber once a source was removed. For the background measurement, an aluminum holder with no previous source implantation history was inserted into the detector and the system was left to condition. A background measurement of the gas counter occurred for a minimum of two hours. In general, a measurement of the background was performed at the beginning and end of an experiment to confirm its stability.

2.3.5 Coincidence Measurement

The HPGe and gas counter can be used in coincidence to identify those decays which emit both a β particle and γ-ray within a specific range of time. The basic setup for a coincidence measurement is: position the radioactive source inside the gas counter at a position of

152.9(1) mm distance from the face of the HPGe (optimized distance for lowest uncertainties attributed to γ-rays), return gas counter to operating conditions, apply voltage to both HPGe and gas counter, and optimize electronics for the measurement.

For proper position of the source-to-HPGe distance, the source must be inside the gas counter and the two halves fully closed. The gas counter is mounted on the same table as the HPGe with the height of the sample in the same plane as the HPGe head. A laser is mounted on the side of the HPGe at a specific angle such that the laser-to-source distance can be converted into an HPGe-to-source distance. The gas counter window facing the HPGe is removed so that there is only air between the source and HPGe. The HPGe is then positioned such that the distance between the source and HPGe head is 152.9(1) mm. The HPGe position is locked in placed and the distance re-measured a final time. The gas counter window is placed back on the gas counter and the detector exhaust is checked for methane bubbling.

The gas counter is allowed to condition and return to an operational state over the next 12 h. Signals from both the HPGe and gas counter are measured and calculations are performed to determine the gas counter is responding in an expected manner. Using the signal generated from the HPGe, γ-rays are measured, the spectrum is energy calibrated, and a preliminary count rate is determined based upon the main peaks of interest. Using the signal generated from the gas counter, a preliminary count rate is determined for both the total system and each detector half. Based upon the isotope being measured, the staff scientist, Victor Iacob, spends several hours tweaking the system in order to optimize the electronics for a $\beta\gamma$ coincidence measurement. The timing window imposed on the system is set to 2.0 μs and parameters such as gain, threshold, and delays are adjusted such that the coincidence response is consistent with what is expected. Losses due to threshold differences between timing and ADC are identified and minimized to the best of the electronic ability.

The basic idea of the coincidence electronic system is to take the signals from the gas counter and HPGe and compare their timing information for correlations. The pulses emitted from

the gas counter are narrow due to the source being within the detection space and the travel of electrons through gas is quick. Conversely, pulses produced from the HPGe are wider as the source is located at some distance and the electrons produced from a γ-ray event are generated in a solid germanium crystal. It is not advantageous to use a gas counter event as the trigger of a coincidence event due to the high rate within the gas counter that could increase the dead time of the coincidence analysis. As such, the γ-ray is used to trigger the start of a coincidence. The gas counter event is delayed by some amount of time so that a comparison can be made on the time scale of the γ-ray event.

The modules used for the coincidence setup are a charge-sensitive preamplifier, an amplifier with a 1/8 μs time constant, a 100 MHz lower-level discriminator, a non-retriggerable gate generator, and a PDP-1 computer operated in a multiscaling mode. The analog electronics of the system have been rigorously characterized and used for many precise γ-ray branching ratio measurements[34,35,36] and for detailed studies of internal conversion[37,38,39].

The system associated to collection of $\beta\gamma$ coincidence events collects the data in cycles of 54.93 s with 5 s of dead time used for other experiments (total 60 s per cycle)[40]. The time window to measure both a γ-ray and β particle in coincidence is set to 2.0 μs. The event is recorded as a coincidence event when both radiations have been observed. Information recorded includes the energy of the γ-ray and β particle, the exact time between the detection of one relative to the other, and the time of the event relative to the start of the cycle. For each cycle, the total number of γ-rays and β particles are counted. Electronic dead times associated to each detection of a γ-ray, β particle, and coincidence measurement are taken as 17 μs, 0.5 μs, and 26 μs.

A background of the coincidence system is also performed. For this measurement, the radioactive source is removed from the gas counter and placed with all other radioactive sources at a location far from the measurement room. A blank source holder with no history of radiation is placed inside the gas counter. Depending on the specific experiment, the amount

of time give for the coincidence background varied, but generally was at least 1 h. The rate of coincidences during background is typically much less than either the β and γ-ray measurements, so high statistics are not achieved. This is mainly a check to confirm the lack of radiation present in the gas counter and identification of any accidental coincidences detected during a source measurement.

2.4 Analysis of Measured Data

From the measurements at TAMU, the main pieces of data acquired are the source's γ-ray spectrum taken using Ortec's Maestro MCA and $\beta\gamma$ coincidence information in ASCII format. Within the coincidence file, there are several pieces of information: the number of γ-rays detected, the number of β particles detected, the timing information between β particles and γ-rays, the β particles in coincidence with γ-ray energy spectrum, and the γ-rays in coincidence with β particles energy spectrum. These coincidence files are processed so that the data is displayed in a meaningful way. Once the γ-ray and $\beta\gamma$ coincidence spectra are acquired, the peaks of interest are analyzed.

2.4.1 γ-ray Peak Fitting

The beginning step of each analysis starts with fitting the γ-ray peaks of interest. In the location where the measurement takes place, there is a large interference from background that can drown out the peaks of interest. As a result, the background was initially analyzed in different ways: (1) γ-ray peaks fit with the background included, (2) integration of a specific range in both source and background γ-ray spectra then subtraction of background area from source, and (3) γ-ray spectrum minus the dedicated background spectrum and fit of the resulting peaks in the subtracted spectrum.

Fitting the peaks over a region of interest worked well in most cases. However, with the high level of background noise present in the γ-ray spectrum, the peak fits would miss the smaller background peaks that were hidden in between the larger peaks. The peak areas which had this interference from background would overestimate the γ-ray peak areas. Peak areas would also vary wildly depending on the parameters of the fits. This method was regarded as less than ideal for a precision analysis.

The next most promising peak fitting method was to integrate both the source spectrum and the normalized background spectrum over a specific range then subtract the two values. The two spectra are energy calibrated so that the regions of interest are the same and the background spectrum was live time normalized. While this method is acceptable, it relied heavily on the region chosen for integration. There is some level of low energy tail on each peak which altered the peak areas especially when the peaks of interest were close in energy. This method did not give reproducible results and was not pursued.

The final method of γ-ray peak fitting involved: normalization of the background spectrum, alterations of gain and peak broadening to match that of the γ-ray spectrum, then direct subtraction of the two. The resulting spectrum contains little interference from background. Performed correctly, this method produced the lowest values of uncertainty in the peak areas with results that were reproducible within error.

Full energy peaks describing γ-ray energies are more than a single channel wide and generally increase in width as the energy of the γ-ray increases. These full energy peaks can be described as a Gaussian function of the form:

$$y\left(x\right) = y_0 * e^{\frac{-(x-x_0)^2}{2\sigma^2}} \tag{2.2}$$

Where $y\left(x\right)$ describes the number of counts in channel x, y_0 is the amplitude of the peak, x_0 is the peak centroid, and σ^2 is the variance. The variance describes the full width at half

maximum (FWHM) of the peak and can be determined by:

$$FWHM = 2\sqrt{2 * \ln 2} * \sigma = 2.35482\sigma \tag{2.3}$$

The area under a Gaussian curve can be determined by:

$$A = \sqrt{2\pi} * \sigma * y_0 = 2.507\sigma * y_0 = 1.0645\,(FWHM) * y_0 \tag{2.4}$$

It is common for γ-ray peaks to be asymmetric around the center due to low energy tailing which occurs as a result of the HPGe being used. In general, the effect is small and can be determined by including a skewed Gaussian to the lower half of the peak[41,42,43].

The background underneath a peak is typically not a straight line. A step function is used with the smoothed step occurring at the center of the peak. A step function is used for two reasons: (1) γ-rays which are scattered such that the deposited energy within the detector is less than the full energy of the original γ-ray and (2) incomplete charge collection of excited electrons within the HPGe detector. Emitted γ-rays that interact with external material before entering the detector result in differences between the original and final energies. Once the γ-ray enters the detector, its energy is absorbed (in part or fully) by an atomic electron. This electron becomes freed and will ionize other atoms to produce a charge which is proportional to the energy of the incident photon. If the energy collected is not equal to the full energy peak, it contributes to the background of the source spectrum. In these cases, the energy is less than that of the full energy peak and raises the background level of the low energy side of the peak resulting in an inconstant background under the peak.

Initially, programs such as Canberra's Genie, Ortec's Maestro, Peakeasy, etc. were used to fit the γ-ray peak. These programs were not employed in the final analysis due to the high level of certainty needed for the fits. On the recommendation of our collaborators at TAMU, the software Radware was chosen the peak fitting software used for this experiment[44].

Radware was developed at Oak Ridge National Laboratory for the purpose of resolving γ-ray coincidence data. Within Radware, the specific package employed is gf3 which is a least

squares peak-fitting program. Each peak fit is made up of a Gaussian (which comprises the majority of the peak), a skewed Gaussian which handles the low energy tail, and a smoothed step function which accounts for an uneven background level under the peak. Several parameters are available to optimize the fit of both the peak and the background. The peak parameters (Fig. 2.11) are made up of: heights of both the peak Gaussian and the skewed Gaussian (R), the decay constant of the skewed Gaussian ($Beta$), and the height of the step function ($Step$). The background is fit by changing the parameters (A, B, and C) in the equation:

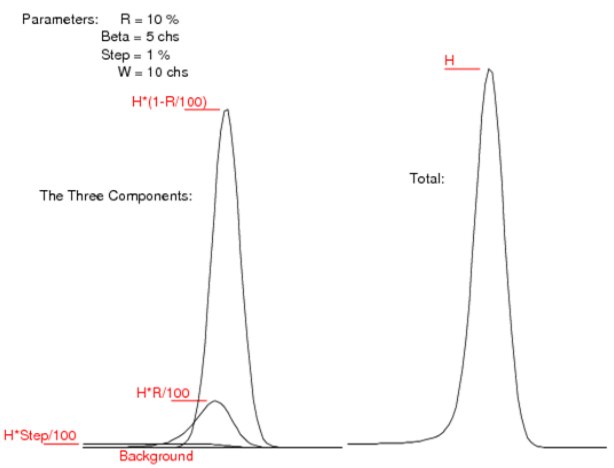

Figure 2.11: Generic method by which Radware fits a γ-ray peak.

$$Background = A + B * X + C * X^2 \tag{2.5}$$

Where X is the channel number. In Eq. 2.5, parameter A will fit the background with a linear fit while B adds a slope and C will induce a curve.

Using the background subtraction method, a large effort is involved to alter the background spectrum so that it aligns well with the source spectrum in both gain and normalization. For gain adjustments, natural radiation peaks (such as ^{212}Bi and ^{214}Pb) in both the source and background spectrum are analyzed to determine the level of gain needed. The centroids of the natural radiation peaks (on the left and right sides of each peak of interest) are identified then compared between the source and background spectra. An average of the differences for each left and right side are calculated and the background spectrum is shifted linearly according to the findings.

Once alignment between the source and background spectra is optimized, normalization is the next parameter on which to work. Initially, a live time normalization factor was used:

$$Normalization = \frac{Source\ Live\ Time}{Background\ Live\ Time} \tag{2.6}$$

The background spectrum is multiplied by this factor and then overlaid onto the source spectrum to see the agreement. In order to prevent over subtraction of the source spectrum, the normalization factor is taken to be slightly less than the live time ratio depending on the agreement between the overlay of the background and source spectra.

Once the proper gain adjustment and normalization are calculated, the background spectrum is altered then subtracted from the source spectrum. In most cases, the subtraction results in a clean spectrum with minimal natural background radiation peaks. Outside the region of interest, the peaks may be over/under subtracted as the gain has not been optimized for that region. Other peaks, such as the 511 keV, are never fully subtracted as its activity can be attributed to both background and the source radiation, causing the activity at the time of the measurement of the source to be unequal to that during background. Extra effort is made for the low energy region (< 100 keV) due to the high level of Compton background. Analysis of peaks in this region requires a separate comparison with the background spectrum.

Once a background subtracted source spectrum is acquired, the γ-ray peak areas are analyzed. Using Radware gf3, each of the peaks were identified and fit over a selected range limited to 100 channels. This range is an accurate depiction of background levels around the peak of interest. Most often, background parameters B and C are set to zero as the background around higher energy peaks is relatively linear. Parameter A is set to the average value of the background level to the right of the peak. The *Step* parameter is determined by averaging the background on the left side of the peak and changing the *Step* so that the fit matches the averaged background level. The *Beta* and R parameters are generally left as the default values of the fit.

2.4.2 $\beta\gamma$ Coincidence Peak Fitting

Once an optimized value of γ-ray peak areas is found, the next step is to fit the $\beta\gamma$ coincidence peaks. As mentioned previously, the coincidence files from the measurement needed to be processed to gain the necessary information for analysis. Mark Stoyer from LLNL (along with my efforts) created a code that reads in the ASCII files and outputs the data into a usable format. The code was error-checked with simplified data and, after several renditions, was able to accurately account for the measured coincidence data.

2.4.2.1 ASCII Data Format

The overall format of the data ASCII files includes a buffer header, a cycle header, and a data set. The cycles come in two forms: coincidence data and heavy ions. In some cases where the activity of the source is low, heavy ion information is inserted into the data to force the buffer to fill up at a quicker rate. When the activity of the sample is high, heavy ions are not needed to force the buffer and are not included in the data set. Within the buffer header (Fig. 2.12a), the "4 1 1" is the start of the buffer with the last value indicating how many lines are in the buffer. The last header before the data is the main one of note (the 12290) as it indicates the data is contained following this header.

After the buffer header section is the cycle header. The data is measured in cycles with each cycle having a set time scale of 54.93 s of data collection. The measurement system forces a dead time of about 5 s. to allow the system to process the data and transfer it to a computer without further loss of collection time. In either case, the cycle header starts with a value of "48387." The cycle header information describes the data that proceeds this header. There are slight differences between the coincidence data and the heavy ion data.

(a)

Buffer Header		
4	1	1
0		
4	1	2
0		
0		
4	1	12290

(b)

Coincidence Header	
48387	
0	
5524	γ-rays
0	
5017	β's
2	Cycle / 2

Coincidence Data Set	
37890	CC Header
4113	
0	
39679	
497	TDC Channel
36865	
2309	γ-ray Channel
9098	β Channel + 8192

(c)

Heavy Ion Header	
48387	
0	
787	Heavy Ions
0	
0	
1	Cycle

Heavy Ion Data Set
37890
1
1
34832
4581

Figure 2.12: ASCII data format of (a) buffer, (b) coincidence, and (c) heavy ion information. The buffer occurs after the transfer of data. The header appears each 54.93 sec. and signifies the end of a cycle. The coincidence data set occurs each time there is a measurable coincidence event and contains the vital information about timing and energies of the β particle and γ-ray. The heavy ion data set occurs at a specific rate when the source strength is low.

2.4.2.2 Coincidence Data

Coincidence headers (Fig. 2.12b) start with a 48387 and end with an even value (shown in green). This even value indicates the data which proceeds it is information associated to coincidence data. To determine the cycle number, the even value in green is divided by 2. The value in blue is the number of γ-rays detected during this cycle and the value in purple is the number of β particles detected during this cycle. Both the γ-rays and β particles are the true values detected by the instrumentation and are not limited by a coincidence event.

The zeros above the blue and purple values in the coincidence header can be non-zero when the count rate is high (over 65,536). For example, if the value above the blue number is 1, the total number of γ-rays would then be $1 * 65,536 + 5524 = 71,060$ γ-rays in the cycle. These spots are reserved for overflow counters.

The format of the coincidence data (Fig. 2.12b) starts with a 37890 value and can be a variable length of 6, 7, or 8 lines long. A full data set contains 8 lines, anything less indicates

some sort of information (TDC, γ-ray, or β) missing from the data set. Within the code, data sets with missing TDC information is accepted as both the β and γ-ray information is present. Those sets with missing β particle information are also accepted as the γ-ray information is present. These missing data are small compared to the overall measurement. The TDC channel number is the 5^{th} line down and can be any values from 1 – 1024. Most of the TDC channel numbers collected will be localized in the center as set by the timing delay. The γ-ray channel number is 7^{th} value. Each γ-ray event will have the channel number listed and can be any value between 1 – 8192 channels. The β channel number is the 8^{th} and last value before another event (starting with the header 37890). Its value can be from 8193 – 16,384 channels. The code will take the value listed for a β event and subtract 8192 to get the real channel at which the β event occurred.

2.4.2.3 Heavy Ion (HI) Data

HI headers start with a 48387 and end with an odd value (in green) (Fig. 2.12c). This odd value indicates the data which precedes this header is HI data. The blue value is the number of HI data sets inserted into the cycle. The HI data sets are 5 lines in length and start with a 37890. For low activity samples, HI headers and data sets are included in the ASCII files. For higher activity samples, the HI headers are included in the files but do not contain any of the HI data sets (the blue value in the header is set to zero). The coincidence code ignores data from HI events as it is not measured data.

2.4.2.4 Coincidence Code Operation

The code discussed in the previous sections reads in a series of ASCII data files, looks for the headers of both the buffers and cycles, and withdrawals the relevant information. That information is then distributed into different histograms. The main files generated from the

output of the code are: γ-ray spectrum gated on the detection of a β particle ($\beta\gamma$ coincidence spectrum), β particles gated on the detection of a γ-ray, the number of detected γ-rays per cycle, the number of detected β particles per cycle, TDC spectrum, and a list of the number of cycles not included in the final output files.

Different cuts can be imposed on the data depending on the information needed. β particles gated on a specific γ-ray can be isolated to study the gas counter response to this specific end-point energy β particle. The TDC time window can be shortened to ignore accidental events which occur outside the main TDC peak. Three main histograms are created of the resulting data which falls within the TDC cut limits. A threshold can be imposed on the number of total γ-rays per cycle in order to eliminate those cycles which have a large spikes in value due to noise or some external force. Typically, the number of skipped cycles is low.

These extra abilities are used to verify the system's operation during measurement. For most of the analysis, the main pieces of information taken from the output of this code are the $\beta\gamma$ spectrum (which includes those events with missing TDC and β information) and the total number of β particles per cycle over the entire measurement. At the beginning of each cycle, the coincidence data misses the first event of TDC information. In order to collect all of the available data, these missing events needed to be added back into the $\beta\gamma$ spectrum. The total number of β particles is used in the calculation of γ-ray branching ratio. It is advantageous to have this measured at the same time as the coincidence events in order to avoid further corrections to the data.

The $\beta\gamma$ spectrum is unlike the γ-ray spectrum in that there is almost no natural radiation peaks present. The background visible in the coincidence spectrum can be attributed to Compton scattering of the γ-rays. Compared to the peak counts, the background levels are quite low. It is possible with higher activity sources to have enough accidental events to register on the $\beta\gamma$ spectrum resulting in a visible background peak. However, these types of peaks have very little counts and do not affect the overall analysis in an appreciable way.

Fitting the $\beta\gamma$ coincidence peaks is similar to fitting the peaks in the γ-ray spectrum. A new fit is started by identifying the range of fit and the peak locations. The background range around the peak is not entirely flat, so parameters B and C are not immediately set to zero. The fit is altered by changing each of the parameters so that it closely resembles the trends of the region. There is more forgiveness in the fitting of $\beta\gamma$ coincidence peaks because the level of background around the peak is generally low and does not appreciably alter the peak area due to slight differences in fits.

2.4.3 Gas Counter Efficiency

Taking the peak areas from the γ-ray and $\beta\gamma$ spectrum, the gas counter efficiency of the detector can be calculated. In order to determine the number of γ-ray or β particle events which occurred, the number of overall decays (N) for a γ or $\beta\gamma$ coincidence event, the efficiency of the detector (ε), and the branching ratio (I_γ) values are needed:

$$N_\gamma = N\varepsilon_\gamma I_\gamma \tag{2.7}$$

and

$$N_{\beta\gamma} = N\varepsilon_\beta\varepsilon_\gamma I_\gamma \tag{2.8}$$

Dividing Eq. 2.8 by Eq. 2.7 results in a measurable efficiency of the gas counter for a specific transition:

$$\frac{N_{\beta\gamma}}{N_\gamma} = \frac{N\varepsilon_\beta\varepsilon_\gamma I_\gamma}{N\varepsilon_\gamma I_\gamma} = \varepsilon_\beta \tag{2.9}$$

This relation is used for a particular β transition and does not apply to the overall isotopic or source gas counter efficiency.

Eq. 2.9 needs to be altered slightly to account for differences in detection times between the γ-ray and $\beta\gamma$ coincidence. The output of the γ-ray signal is split in two directions: direct measurement of the emitted γ-rays and further processing for $\beta\gamma$ coincidence. As a result, the measurements are performed at slightly different times using different systems. To make

these two measurements comparable, each measurement needs to be decay-corrected to a specific time and changed into a rate.

For γ-ray measurements, the data is taken in 30 m intervals over the entire length of the measurement. The γ-ray detector is refilled every 12 h causing the detector to exhibit high dead times and increase electronic noise. There are several 30 m intervals taken out of the full measurement to overcome the filling process. For the $\beta\gamma$ coincidence measurement, the system would stop collection randomly. Once the system is manually restarted, the data collection would continue. However, there is a time interval of missing data which needs to be tracked. The decay correction equation is applied directly to the peak areas of the γ-ray and $\beta\gamma$ coincidence and includes the specifics of the start/stop times for each interval of data as well as the dead time.

The area of the peaks can be transformed into a rate (R) by dividing the area by the total amount of time the measurement was collected (the live time). The rate at any time during the measurement can be calculated by:

$$R = R_0 e^{-\lambda t} \tag{2.10}$$

Where R_0 is the reference rate, λ is the decay constant, and t is the time between the reference measurement and current measurement.

Suppose there was an interruption during the duration of the measurement (Fig. 2.13) causing two start (t_1 and t_3) and stop times (t_2 and t_4). In order to determine the overall rate during the measurement, one can correct for this missing time and relate the two rates to a reference rate (t_0). The area under the curve in the regions of interest can be determined by:

$$A = \int_{t_2}^{t_1} R_1 dt + \int_{t_4}^{t_3} R_2 dt \tag{2.11}$$

Using the derived equations for activity (Section 1.4.1), this equation reduces similarly to:

$$A = \frac{R_0}{\lambda}\left(e^{-\lambda t_1} - e^{-\lambda t_2} + e^{-\lambda t_3} - e^{-\lambda t_4}\right) \tag{2.12}$$

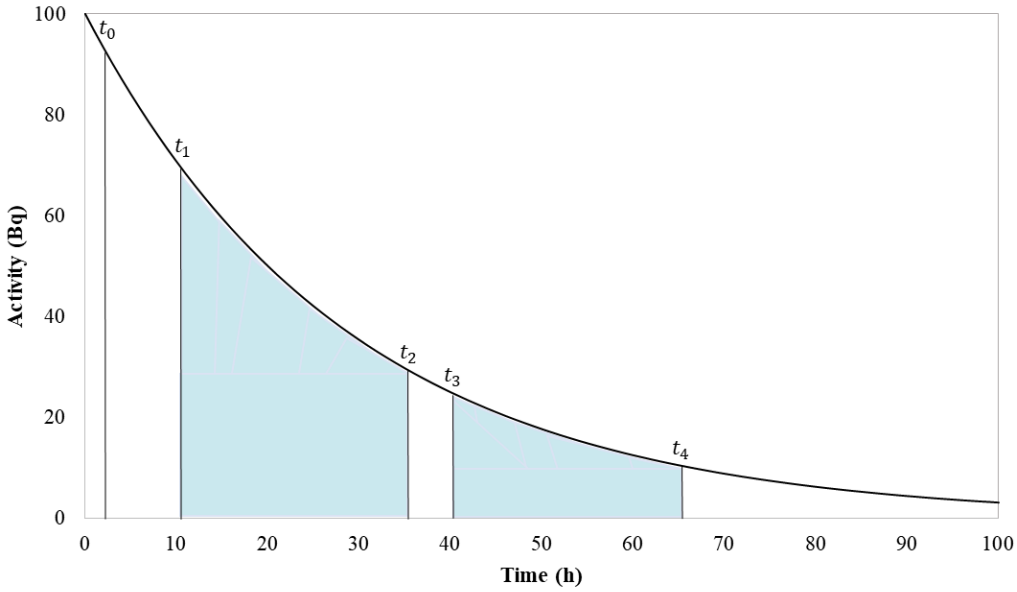

Figure 2.13: Generic source activity over time. Two measurements of this source are taken over this range showing a decay correction for the activity to some reference time, t_0.

Which rearranges to give an expression for the rate of the sample at some reference time:

$$R_0 = \frac{A\,\lambda}{(e^{-\lambda t_1} - e^{-\lambda t_2} + e^{-\lambda t_3} - e^{-\lambda t_4})} \tag{2.13}$$

Where the term A is the peak area of either the γ-ray or the $\beta\gamma$ coincidence. Eq. 2.13 can be altered to allow for more interruptions in the measurement time.

Applying this correction to both γ-ray and $\beta\gamma$ coincidence data sets will give a rate at a specific reference point which allows the two values to be directly compared. Depending on the half-life of the sample, this decay correction will be small because the overall ratio between the $\beta\gamma$ and γ-ray rates is the desired outcome. The gas counter efficiency can then be calculated using these two rates determined at the reference time.

It is important to note the way gas counter efficiency is defined in this context. A γ-ray must be emitted a short time after the emission of the β particle. If, for some reason, the

γ-ray was not emitted (as is the case for a CE emission), a measured gas counter efficiency would not be achievable.

2.4.4 Simulations using GEANT4

Measured gas counter efficiencies can then be compared to simulated gas counter efficiencies for different transitions. The simulations can be a better model for the measurement as it is not prone to experimental difficulties. The simulations also have the added advantage of calculating the total gas counter efficiency for the isotope and more complex decays for the case where a γ-ray is not emitted. A more general discussion of the simulations and the effort that went into optimizing them will be discussed in Chapter 3. For the calculation of γ-ray branching ratios, the simulations are tuned to represent measured data, then those simulated values are used for the calculation.

2.4.5 β Particle Rate Associated to the Isotope of Interest

One of the pieces of information determined from the coincidence code is a value for the number of β particles detected during the measurement. This value is made up of contribution's from parent and daughter isotopes along with any contamination or isomers included in the source. As a result, the total amount of β particles needs to be separated into its individual components. This is accomplished by theoretical calculations involving the specific details of the sample creation/decay.

2.4.5.1 Theoretical Ratio of Isotope to Source

The radioactive source is created then decays over specific time ranges. These times can be used to calculate a theoretical ratio of isotope (parent or daughter) to total source. During

CARIBU source collection, specific times at which ions were implanted were noted. The number of parent atoms implanted (N_{Parent}) can be determined by accounting for the decay of the previous hour's atoms ($N_{Previous}$) and the contribution of the current hour's atoms ($N_{Current}$):

$$N_{Parent} = N_{Previous}e^{-\lambda t} + N_{Current} \tag{2.14}$$

An assumption being made is that the rate of new ions per hour is relatively constant over the time intervals at which the spectra were taken during monitoring of the beam. This is not quite accurate as the CARIBU beam varies in strength as time progresses and sometimes cuts out for tuning. The number of parent decays per hour (A_{Parent}) can be calculated by:

$$A_{Parent} = N_{Previous}\,(1 - \lambda_{Parent}) \tag{2.15}$$

Which is directly equal to the number of new daughter atoms being created per hour (as the daughter is not directly created from CARIBU implantation). The total number of daughter atoms implanted per hour is made up of the number of new daughter atoms decaying from the parent and the number of daughter atoms decaying from the previous hour. The number of daughter atoms can be converted into the number of daughter decays ($A_{Daughter}$) similarly to Eq. 2.15 by:

$$A_{Daughter} = N_{Previous}\,(1 - \lambda_{Daughter}) \tag{2.16}$$

Once the implantation process has completed, the sample no longer receives any additional ions. Instead, the existing ions continue to decay and Eq. 2.14 simplifies to:

$$N_{Parent} = N_{Previous}e^{-\lambda t} \tag{2.17}$$

The daughter is unchanged by the completion of collection. After implantation, the parent and daughter continue to decay at a constant rate. Once source measurement begins, a summation of the total decays for the isotope (parent, daughter, or contamination/isomer) and the total decays for the source (combination of parent, daughter, and any contamination/isomer) are calculated.

This theoretical calculation of the ratio is based upon activities rather than the detected number of β particles. The total β particles detected is an observable, which is dependent on the efficiencies of the detector. The ratio of detected particles ($Ratio_{Observed}$) can be found by multiplying the activities of each isotope by their gas counter efficiencies:

$$Ratio_{Observed} = \frac{A_{Isotope}}{A_{Source}} * \frac{\varepsilon_{\beta_{Isotope}}}{\varepsilon_{\beta_{Source}}} \tag{2.18}$$

The ε_β of the isotope and total source are determined using simulations as it takes into account each of the possible decay scheme transitions.

This ratio of isotope to total source activity is effective if there are isomeric states or contamination within the source whereby the source is made up of several decaying isotopes instead of solely a parent and daughter combination. This value takes the measured rate of the source and separates the isotopic contributions based upon the growth and decay of the isotopes (or isomer) that make up the source.

2.4.6 γ-ray Branching Ration Equation

The previous calculations discussed in this Chapter are applied to the calculation of the γ-ray branching ratio. The form of the γ-ray branching ratio equation is shown:

$$BR = \frac{R_{\beta\gamma}}{R_{\beta_{total}}\varepsilon_\gamma}\frac{\varepsilon_{\beta_{total}}}{\varepsilon_\beta} \tag{2.19}$$

Where $R_{\beta\gamma}$ is the rate of $\beta\gamma$ coincidences, ε_β is the gas counter efficiency of a β particle gated on the γ-ray of interest, ε_γ is the HPGe efficiency of the γ-ray of interest, $\varepsilon_{\beta_{total}}$ is the efficiency of the gas counter for the isotope, and $R_{\beta_{total}}$ is the rate of the detected β particles of the isotope.

2.5 Uncertainty Contributions

In any sort of measurement, there are uncertainties that can be assigned to each value. The heart of this research is to minimize the uncertainty associated with these types of measurements. For each isotope to which the analysis is applied, a basic set of calculations can be used to determine the uncertainty for each of the values.

For a given function, $F = f(x, y)$, where the measured value of x represents the mean of a Gaussian distribution and σ represents the standard deviation of the Gaussian distribution, the variance of F can be determined by:

$$\sigma_F{}^2 = \sigma_x{}^2 \left(\frac{\partial F}{\partial x}\right)^2 + \sigma_y{}^2 \left(\frac{\partial F}{\partial y}\right)^2 + 2\sigma_{xy}{}^2 \left(\frac{\partial F}{\partial x}\right)\left(\frac{\partial F}{\partial y}\right) \tag{2.20}$$

Where σ_x and σ_y are the standard distributions of x and y. Eq. 2.20 applies if x and y terms are correlated. If both x and y terms are uncorrelated, $\sigma_{xy} = 0$ and the uncertainty is determined by:

$$\frac{\sigma_F}{F} = \sqrt{\sigma_x{}^2 \left(\frac{\partial F}{\partial x}\right)^2 + \sigma_y{}^2 \left(\frac{\partial F}{\partial y}\right)^2} \approx \sqrt{\frac{\sigma_x{}^2}{x} + \frac{\sigma_y{}^2}{y}} \tag{2.21}$$

For calculations associated with the measurement of γ-ray branching ratios, the derivation of the function, F, can be reduced to the uncertainty of the value divided by its value added in quadrature.

2.5.1 Uncertainties in γ-ray Peak Area

A large effort goes into determining the peak area of the γ-ray of interest. The difficulty stems from the large amount of background that is included with the measurement of the sample. A dedicated background measurement performed close to the same time as the source measurement is taken. The background spectrum is normalized, gain-shifted, and peak-broadened so that it aligns with the source spectrum over the region of interest. It is then subtracted from the source spectrum to produce a third spectrum that is almost free of

interference from background peaks. This third spectrum is then analyzed and a peak area is taken by fitting the background region underneath the peak and integrating the counts above it. In each step of this process, the uncertainties are calculated.

2.5.1.1 Statistics and Fitting of Peak Area

For each peak, uncertainties in the number of counts and the randomness of peak fitting were examined. The statistical uncertainty is based upon the number of counts in the peak and is determined by:

$$\sigma_{Statistical} = \sqrt{A} \tag{2.22}$$

Where A is the area of the peak determined by Radware. Radware accounts for the statistical uncertainty in the peak and agreement of the background fit under the peak. Levels of fluctuation between the background and the fit of the background are taken as the uncertainty ($\sigma_{Radware}$).

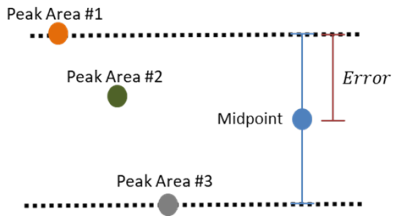

Figure 2.14: Variations in peak fitting result in an uncertainty that is half the midpoint of the two extremes.

An extra uncertainty in the fit is included by fitting the peaks several times (σ_{Fit}). The resulting peak areas are compared for the maximum and minimum values with the error calculated as half of the midpoint value (Fig. 2.14).

2.5.1.2 Gain and Normalization

For comparison of source and background spectra, the values of normalization and gain are varied so that the uncertainties associated with choosing any specific value are determined. Once the true value of normalization and gain is chosen, an assumed shift of roughly $\pm 1\sigma$ is used to determine the uncertainty. This process is performed in order to control the level of

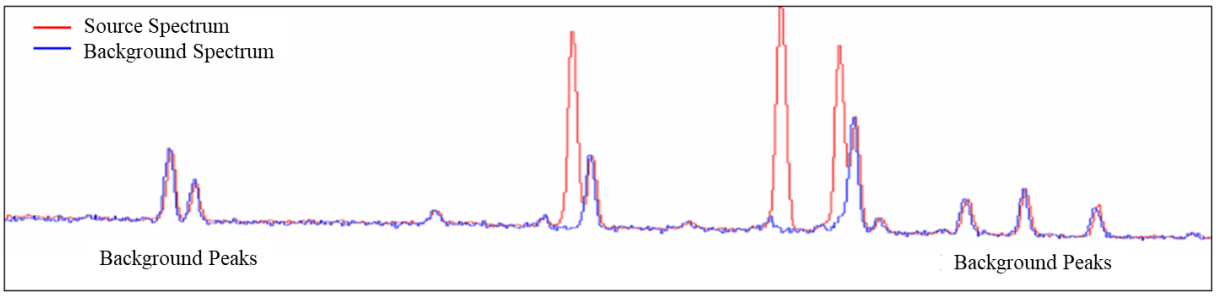

Figure 2.15: Spectra from a source and dedicated background measurement overlaid. To align the peaks of interest, background peaks found in both spectra are fit to determine their center. The dedicated background is then shifted so that proper alignment is achieved.

improper gain shifting and over/under subtraction of the dedicated background spectrum. In general, the uncertainties for each shift calculation are small.

Determining the $\pm 1\sigma$ shift in gain is achieved by identifying the centroid of background peaks which appeared in both the source and dedicated background spectra on the left and right side of the peak of interest (Fig. 2.15). Comparison of the peak centroids of the dedicated background and source spectrum give a good indication of the amount of gain shift that has occurred between the two spectra. The centroid value uncertainty is given by Radware. For multiple fits, the total centroid uncertainty is calculated by:

$$\sigma_{Shift} = \sqrt{\sum_{i=1}^{n} \left(\frac{\sigma_{Centroidi}}{n} \right)^2} \tag{2.23}$$

Where n is the number of peaks on either the left or the right side of the source peaks. Radware shifts a spectrum linearly, accounting for a smaller shift in the low energy region and a larger shift in the high energy region. Manipulations to the background spectrum produced two new spectra (-1σ shift and $+1\sigma$ shift) which were each subtracted from the source spectrum. The peak areas of the resulting subtracted $\pm 1\sigma$ spectra were determined. A total uncertainty attributed to a shift in gain (σ_{Gain}) was calculated by taking half the midpoint between the highest and lowest source peak area values for $\pm 1\sigma$ gain shift spectra (Fig. 2.14).

In a similar fashion, the uncertainty in the normalization value is determined. An initial live time normalization of the dedicated background spectrum is assumed then altered based upon direct comparison of the region of interest of the source and background spectra. A $\pm 1\sigma$ shift is determined based upon the live time ratio. The dedicated background spectrum is altered by a $+1\sigma$ and a -1σ normalization. Both spectra are subtracted from the source spectrum to produce two shifted, normalized subtracted spectra. The resulting source peaks are determined using the same integral region as the previous fits. The peak areas of the shifted normalized spectra are compared and the uncertainty (σ_{Norm}) calculated in a similar fashion to the gain shift (Fig. 2.14).

2.5.1.3 Background Subtraction of γ-ray Spectrum

An additional uncertainty in the overall background subtraction is also needed. For these measurements, there are two types of backgrounds: the background level underneath the peak of interest in the source spectrum (B_s) and the dedicated background measurement with no source (B_b). The two backgrounds are related by:

$$B_s \cong s_c * B_b \tag{2.24}$$

Where s_c is a scaling factor that is equal to the normalization. In the source spectrum, the total number of counts inside the region of interest is made up of:

$$T = P + B_s \cong A + s_c * B_b \tag{2.25}$$

Which has an uncertainty of:

$$\sigma_T \cong \sqrt{{\sigma_A}^2 + {s_c}^2 {\sigma_{B_b}}^2} \tag{2.26}$$

Where P is the counts of the peak without the background (B_s), A is the Radware determined integral of the peak, σ_T is the uncertainty in the total number of counts over the region of interest, σ_A is the Radware generated uncertainty in the peak area, and σ_{B_b} is the uncertainty of the background over the region of interest.

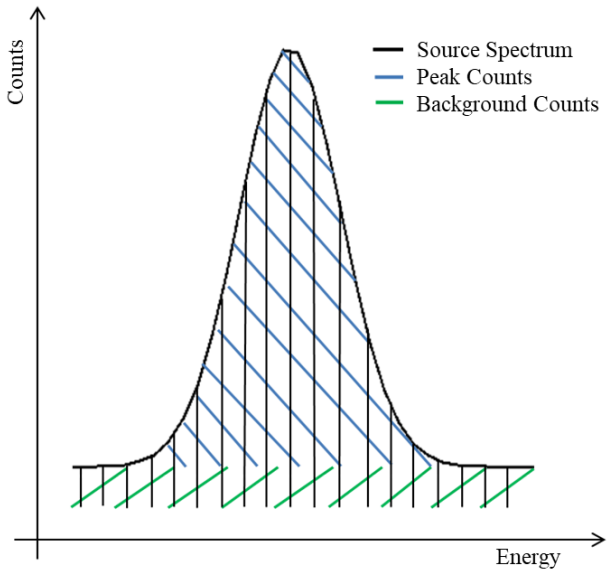

Figure 2.16: Simplification of the qualities that make up a γ-ray peak.

To determine the counts of the peak in the region of interest:

$$P \cong T - s_c * B_b \tag{2.27}$$

With an uncertainty determine by:

$$\sigma_P \cong \sqrt{{\sigma_T}^2 + {s_c}^2 {\sigma_{B_b}}^2} \tag{2.28}$$

Inserting Eq. 2.26 into Eq. 2.28 results in:

$$\sigma_{Sub} = \sigma_P \cong \sqrt{{\sigma_A}^2 + 2{s_c}^2 {\sigma_{B_b}}^2} = \sqrt{{\sigma_A}^2 + 2{s_c}^2 * B_b} \tag{2.29}$$

Using the fact that the uncertainty associated to the dedicated background is purely statistical, σ_{B_b} can be substituted for the integral of the background over the region of interest ($\sigma_{B_b} = \sqrt{B_b}$).

Each of the separate contributions to uncertainties which make up the determination of the γ-ray peak area can be combined in quadrature:

$$\sigma_{R_\gamma} = R_\gamma * \sqrt{{\sigma_{Radware}}^2 + {\sigma_{Fit}}^2 + {\sigma_{Gain}}^2 + {\sigma_{Norm}}^2 + {\sigma_{Sub}}^2} \tag{2.30}$$

2.5.2 Uncertainties in Coincidence Peak Fitting

Unlike the uncertainty determination for peak area of the γ-ray spectrum, the uncertainty associated with the $\beta\gamma$ coincidence peaks are more straightforward. The nature of the $\beta\gamma$ spectrum is simple in that there are no background peaks interfering with the source peaks. The uncertainty can be attributed to the statistical area of the peak, the fit of the background underneath the peak, and possible variations of the fit. Radware determines the statistics and the agreement of the peak fitting, while the variation is calculated by fitting the peak several times and taking the difference between the maximum and minimum peak area values (Fig. 2.14).

2.5.3 Uncertainties in Measured γ-ray and Gas Counter Efficiencies

The uncertainty associated with the γ-ray efficiency is determined by both experimental measurements and Monte Carlo simulations performed by the researchers at TAMU. A major reason to measure the source using the HPGe detector located at TAMU is due to their precision determination of the γ-ray efficiency between the energies of 50 and 1400 keV at a distance of 151.0(1) mm[20,7,23]. A malfunction of the laser system used to measure this distance occurred over the course of the measurements that was assessed after the completion of all the experiments performed for this thesis. The malfunctioning laser was analyzed for fault and a new distance of 152.9(1) mm was determined to have been used for the experiments. Using the precision instrumentation at TAMU adds an uncertainty of 0.3% (increased to account for the malfunction of the laser system) in the measurement of γ-rays over the energy range of this experiment.

Calculation of the gas counter efficiencies is determined by dividing the $\beta\gamma$ peak count rate by the γ-ray peak count rate. The uncertainty associated with this calculation is determined

by adding each of the contributions in quadrature:

$$\sigma_{\varepsilon_\beta} = \varepsilon_\beta * \sqrt{\left(\frac{\sigma_{R_\gamma}}{R_\gamma}\right)^2 + \left(\frac{\sigma_{R_{\beta\gamma}}}{R_{\beta\gamma}}\right)^2} \tag{2.31}$$

2.5.4 Uncertainties in Simulated Gas Counter Efficiencies

Uncertainties associated to gas counter efficiencies are determined by varying simulation parameters so that the uncertainties are comparable with measured data. The two parameters to vary are the simulated source foil thickness and the imposed electronic threshold. According to the manufacture of the carbon foils[45], the thickness of the foil is quoted to $\pm 10\%$. The simulation assumes this variation as true and calculates gas counter efficiencies with foils that are $0.20 \pm 0.02\ \mu m$. The maximum difference of gas counter efficiency from the true thickness of $0.20\ \mu m$ is taken as the uncertainty associated with the foil thickness.

Variations in electronic threshold are also imposed. Threshold uncertainties are calculated by determining the gas counter efficiencies at the experimentally determined threshold and at thresholds that match the gas counter efficiency uncertainty range ($\pm 1\sigma$). The maximum difference between the gas counter efficiencies at the true and variable thresholds are taken as the uncertainty. An additional statistical uncertainty is calculated from the number of simulated events. Each simulation is performed with one million events which result in a statistical uncertainty of 0.1%. The final value which can be assigned to the simulated uncertainty is each contribution added in quadrature:

$$\sigma_{\varepsilon_{\beta_{sim}}} = \varepsilon_{\beta_{sim}} * \sqrt{{\sigma_{Thickness}}^2 + {\sigma_{Threshold}}^2 + {\sigma_{Statistical}}^2} \tag{2.32}$$

These simulated variations can be performed with a specific transition or an entire isotope which includes each possible transition. For determination of γ-ray branching ratio, the simulated gas counter efficiencies are used as they can accurately match the measured values and recreate a total gas counter efficiency for the isotope, something which is unmeasured in this system.

2.5.5 Uncertainty in β Particle Determination

Within the source, radiation is emitted by the isotope of interest, the daughter, and any contamination or isomeric states within the sample. As such, effort is taken to disentangle the contributions of the measured data in coincidence. Isotopic contributions of β particles are determined by theoretical calculations of the source's history of growth during CARIBU implantation and subsequent decay. The uncertainty associated to the number of ions implanted and their decay is dependent on the possible variation of beam intensity over the course of CARIBU collection, half-life uncertainties, and the statistics of the measured β particles.

During source implantation at CARIBU, γ-ray spectroscopy was performed during multi-hour-long intervals and the average rate during the measurement time is taken as the implantation strength of that time period. The variation of implantation comes by assuming all the activity is implanted within the first few minutes of a measurement and decay occurs throughout the remainder of the collection time of each measured time interval. Ratios of the isotopes of interest over the total number of implanted ions are calculated for both average and immediate collection over CARIBU measurement. The maximum differences between the two ratios for specific isotopes are taken as the uncertainty. As literature values of isotopic half-lives are used for determination of decay, uncertainties associated to these values are also included. An additional uncertainty is added to account for the statistics of the measured β particles over length of the measurement at TAMU:

$$\sigma_{\beta_{theoretical}} = \beta_{tot} * \sqrt{\sum_{Isotope} (\sigma_{Ratio})^2 + \sum_{Isotope} \left(\sigma_{t_{1/2}}\right)^2 + (\sigma_{\beta_{stat}})^2} \tag{2.33}$$

Theoretical values are further confirmed by directly calculating the isotopic β contribution from measured $\beta\gamma$ coincidence values and correcting for efficiencies and literature γ-ray branching ratios. The uncertainty associated to this β particle calculation is taken as each

term added in quadrature:

$$\sigma_{\beta_{measured}} = \beta_{tot} * \sqrt{\left(\frac{\sigma_{R_{\beta\gamma}}}{R_{\beta\gamma}}\right)^2 + \left(\frac{\sigma_{\varepsilon_\gamma}}{\varepsilon_\gamma}\right)^2 + \left(\frac{\sigma_{\varepsilon_\beta}}{\varepsilon_\beta}\right)^2 + \left(\frac{\sigma_{BR}}{BR}\right)^2 + \left(\frac{\sigma_{\beta_{bkg}}}{\beta_{bkg}}\right)^2} \tag{2.34}$$

Where $\sigma_{R_{\beta\gamma}}$ is the uncertainty in the rate of the $\beta\gamma$ coincidence value, $\sigma_{\varepsilon_\gamma}$ is the uncertainty in the efficiency of the γ-ray, $\sigma_{\varepsilon_\beta}$ is the uncertainty of the gas counter efficiency for a specific transition, σ_{BR} is the uncertainty associated with the branching ratio, and $\sigma_{\beta_{bkg}}$ is the uncertainty associated to the measured β detector background. The β background is measured several times before and after the measurement, the variation of the background rate is taken as the uncertainty.

2.5.6 Uncertainty in Correlated Terms

There are several terms within the γ-ray branching ratio calculation that are highly correlated in the sense that the terms are greatly dependent on each other; if one term changes, the resulting correlated terms will also change in a similar way. Measurements involving the gas counter are highly dependent on the energy of the β particle and the resulting efficiencies. The most direct way to handle the uncertainties associated to these correlated terms is to calculate the mathematical differences between the γ-ray branching ratio terms that are correlated:

$$\frac{\varepsilon_{\beta tot}}{\varepsilon_\beta * N_{\beta tot}} \tag{2.35}$$

β particles being measured for a specific isotope have a direct effect on the resulting efficiency associated to the gas counter. As discussed, variations in the foil thickness and electronic threshold effect each of these terms and that variation in correlated values can be calculated directly. Simulated gas counter efficiencies are used for this uncertainty calculation.

For uncertainties associated to variations in thickness, Eq. 2.35 is calculated when the thickness is 0.18, 0.20, and 0.22 μm. The difference between calculated Eq. 2.35 value at 0.20 μm

and the variations is chosen as the uncertainty. For uncertainties associated to variations in electronic thresholds, measured gas counter efficiency uncertainties are used as the possible variations and the thresholds imposed on the simulations are set to match. The maximum difference of the variation is taken as the uncertainty attributed to electronic threshold.

For example, a measured efficiency could be 0.90 ± 0.02. Simulated thresholds are set so that the resulting efficiencies are 0.88 and 0.92. A calculation of Eq. 2.35 for efficiencies of 0.88, 0.90, and 0.92 is performed and the uncertainty is taken as the maximum difference between 0.90 and its variation. The final uncertainty associated to correlated terms includes variations in source foil thickness and detector threshold that are added in quadrature.

2.5.7 Uncertainty in the γ-ray Branching Ratio

The final determination of uncertainty associated to the γ-ray branching ratio (Eq. 2.19) takes into account each piece of the calculation including the effect of correlated terms.

$$\sigma_{BR} = BR * \sqrt{\left(\frac{\sigma_{N_{\beta\gamma}}}{N_{\beta\gamma}}\right)^2 + \left(\frac{\sigma_{\varepsilon_\gamma}}{\varepsilon_\gamma}\right)^2 + (\sigma_{\beta_{theoretical}})^2 + \left(\sigma_{\left[\varepsilon_{\beta tot}/\varepsilon_\beta \ * \ N_\beta\right]}\right)^2} \tag{2.36}$$

Chapter 3

Simulations using GEANT4

A large effort of this research was spent developing a simulation to accurately represent experimental measurements. Simulations are an important tool to verify the gas counter response and give confidence to the measurements which use the gas counter. All particles emitted from the source need to be accounted for in order to form an accurate γ-ray branching ratio scheme. This becomes complicated due to the nature of β particles and their interaction with materials. Two main ways β particles can avoid detection are: (1) the deposition of all of its energy and subsequent absorbance within the source foil material and (2) little deposition of energy within the detection gas resulting in a β particle signal that is indistinguishable from the electronic noise of the system. For this reason, accurately modeling the radioactive source inside the detector will give an idea of the overall efficiency[46,47], which can be applied to precision measurements.

For calculation of the γ-ray branching ratio, two gas counter efficiencies are needed: transition-specific and isotope. The transition-specific decay can determine an efficiency for a specific transition with one $E_{\beta_{max}}$ value. The isotope decay takes into account the entire decay scheme (including β particles, CE, and γ-rays) for the isotope, and includes the contribu-

tion of the transition-specific decay. While direct measurement of the source can determine the transition-specific gas counter efficiencies, it cannot identify the total isotopic efficiency due to the lack of identifiable γ-rays in a majority of decays (due to emission of a CE or direct decay to ground state). Thus the need for simulations. With this simulation, both a CARIBU source and a reactor-made source can be modeled.

The GEANT4 simulation toolkit is used to represent the physical system. It is designed to track the energy loss of particles moving through matter using Monte Carlo methods[48,49,50]. The code has applications in high energy environments, such as nuclear and accelerator physics, medical applications relating to radioactivity interacting with biological matter, and space systems such as the effects of solar particles and environments on materials in space. The program uses object-oriented programming in C++ to create objects with specific attributes such as elemental composition, density, shape, orientation in space, and specific responses to particles. The GEANT4 toolkit: creates a system of specific materials, runs a series of decays through that system, tracks the particles throughout the specified materials, records the system response, and creates visualization files. It was essential to learn and understand object-oriented programming and apply it to the simulation code in order to produce a simulation that is representative of the physical system.

3.1 Gas Counter Designs

A simplified GEANT4 detector code was created by the collaborators at Lawrence Livermore National Laboratory (LLNL) in order to get started with a base detector design to become accustomed to the program. The initial simulation design is quite primitive (Fig. 3.1a): a square aluminum foil ($2 \times 2 \times 0.45\ cm^3$) was placed in free space with a radioactive point source located on one side. The detector consisted of a cubic space ($10 \times 10 \times 10\ cm^3$) filled with p-10 gas (mixture of argon and methane). At one side of the foil, a mono-energetic β

emitting point source of 834 keV was simulated. The detection space is within the yellow square and the β particle simulated deposits energy within the detection gas.

As the simulation matured, the dimensions were refined to better reproduce the design of the physical detector. The next variation of the detector introduced housing made out of copper material with a cylindrical cutout that made up the detection space (Fig. 3.1b). Within the center of the detection chamber, a cylindrical carbon foil was placed with a diameter equal to the chamber. A pressure of 1 atm of p-10 gas filled the detection space. A split of the chamber into two equal detection areas (red and green) was implemented for the purpose of monitoring the individual detector response of either side. The division of the detector into two sides is similar to the physical detector, as two sides of the detector can be operated independently. For the CARIBU experiment, the sample is deposited asymmetrically on one side of the foil. As such, one side of the gas counter should see less overall counts because the particles have to travel through more foil material to deposit energy on that side of the chamber. This difference in signal is seen in both simulated and physical detector responses.

Fig. 3.1c shows a reduced foil diameter from 3.65 cm to 0.95 cm with the detection space surrounding the foil on all sides. This change in detector design prompted a new way of coding as the detection space needed to surround the foil without including its volume. With object oriented coding, the steps included: defining an object by giving it dimensions, defining a subtraction solid by giving it dimensions, subtracting the two solids along with any rotational and translational information needed for the subtraction's placement with respect to the object, creating a logical volume by defining the material it is made up of, and placing it within the mother volume along with any rotational and translational information with respect to the mother volume origin. For any solid that is not a typical cylinder or cube shape, these steps are necessary.

Fig. 3.1d introduces a basic aluminum holder which suspends the foil in the middle of the detector. Initially, this holder was designed as a cylinder with a hole having the same

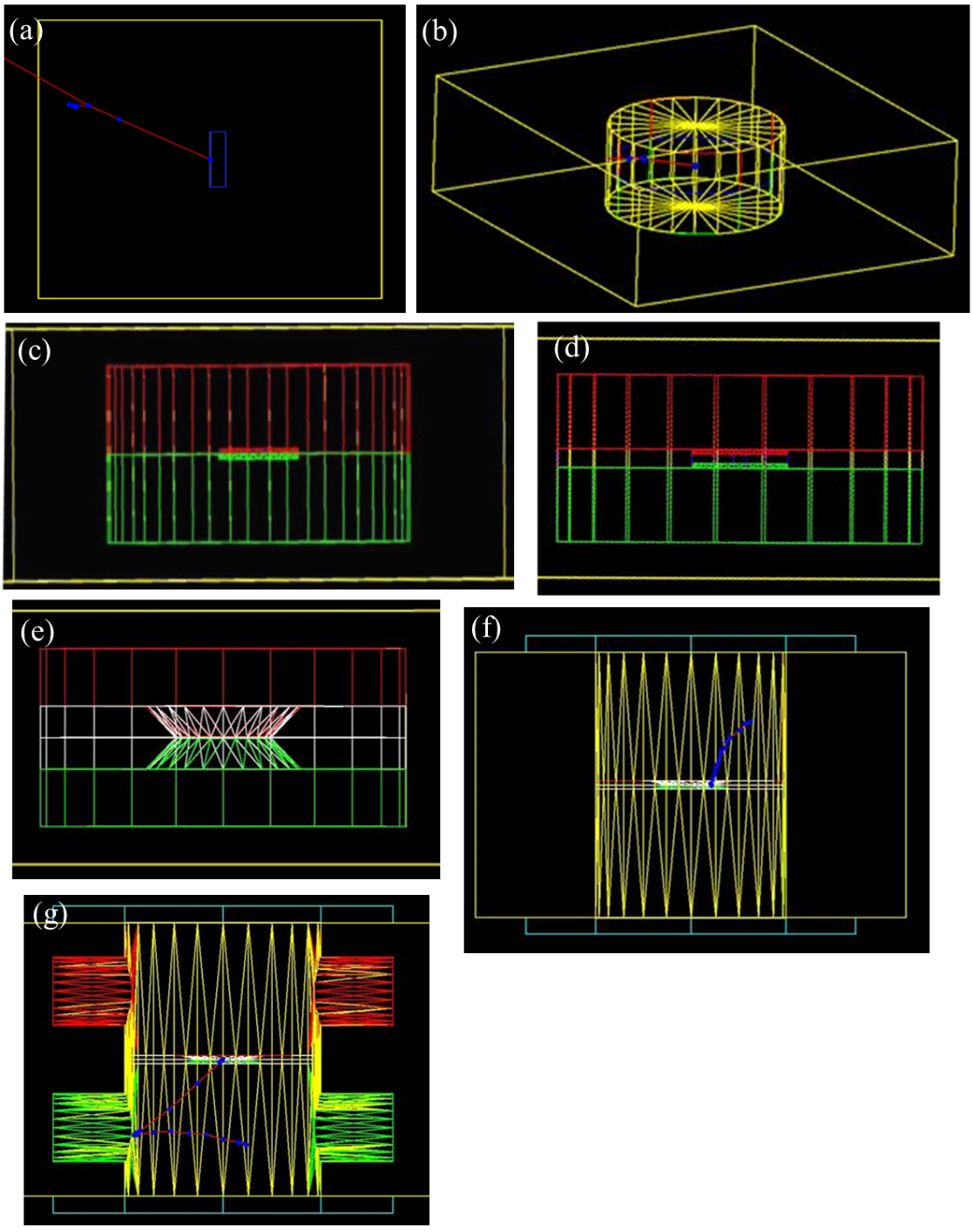

Figure 3.1: Evolution of gas counter designs simulated in GEANT4.

diameter as the foil. Fig. 3.1e shows an exaggerated version of the changes to the aluminum holder so that the inner opening is 0.5 mm bigger than the foil and there is a bevel in the holder angled away from the foil. In the simulation, the foil floats in the center with no support.

The detection chamber was reshaped to the proper dimensions of the actual detector (cutout of the detection space extended through the copper with a height of 5.08 cm) including 12.7 μm-thick Havar windows and aluminum support frames on either side of those openings (Fig. 3.1f). The detection gas was changed from p-10 to methane. Methane gas is ideal for detectors which have the need to dampen the signals produced by γ-rays as methane and γ-rays do not interact in a meaningful way. Methane also quickly dispels the energy absorbed from interactions with β particles, producing fast responses after an event. The detection chamber would be open to the world if not for the windows; the detector housing does not extend to cover the chamber. This design is for the purpose of detecting both β particles and γ-rays emitted in coincidence which is useful when determining gas counter efficiency. The thin Havar windows allows for γ-rays to pass with minimal attenuation.

The final detector dimension change (Fig. 3.1g) was to include four cylindrical inserts to the detector chamber. In the physical detector, these inserts hold the anode wires and keep them in place across the width of the detector. These inserts increase the volume of the detection chamber and could potentially change the energy deposition results. The final design of the gas counter (Fig. 3.2) now takes into account major features of the detector, including all materials and dimensions, and has shown to agree well with experimental analysis for both the CARIBU and the reactor-made sources.

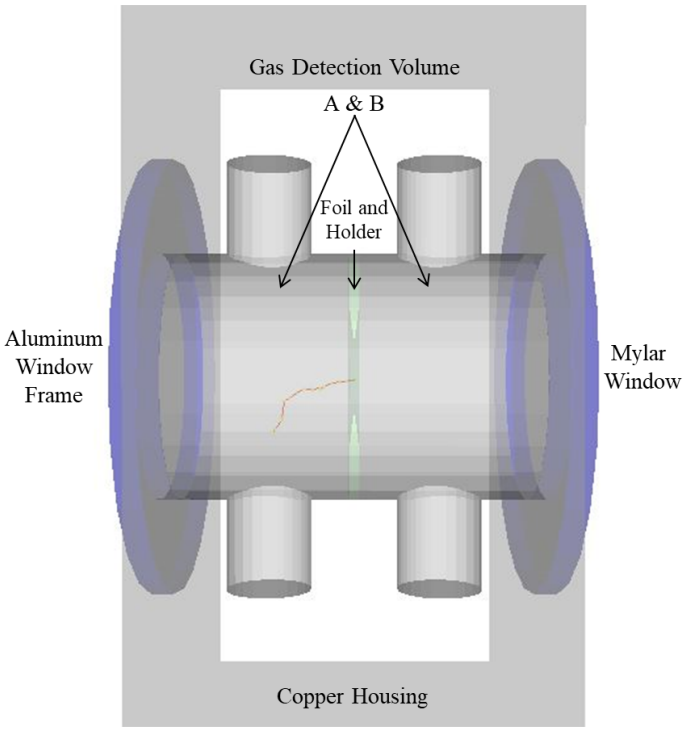

Figure 3.2: Final simulated version of the gas counter representing all the major features of the physical detector.

3.1.1 Differences Between Simulated and Physical Detector Designs

There are some differences between the physical and simulated gas counter. While the physical detector is of a gas flow design, the simulated detector assumes a closed design with the gas at atmospheric pressure. In the physical detector, rather than the foil suspended in space, the carbon foil for the CARIBU source is floated onto the aluminum holder (Fig. 3.3a). The sample foil for the reactor-made source is held by thin tungsten wires having a diameter of 12 μm (Fig. 3.3b). This grid, based on the dimensions and placement of the wires, was calculated to cover 0.6% of the foil surface area. As this is not a large correction, it was assumed to have a negligible effect on the emitting β particles and is not included in the simulation.

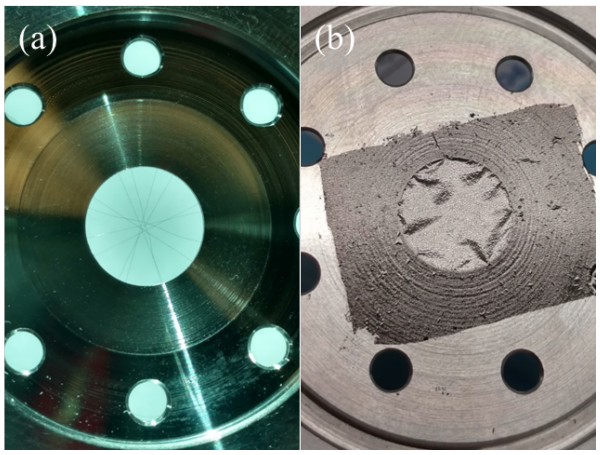

Figure 3.3: Source holders for a reactor-made and CARIBU-made sources. The reactor source (a) is held in place with thin wires while the CARIBU source (b) consists of carbon foil floated on top of the source holder.

There are also no anode wires collecting the free electrons to produce a signal represented in simulations. Rather, the active space detects all energy deposited in the gas and post-simulation analysis imposes electronic threshold cuts that eliminate those particles that deposit less than the threshold energy. Inside the physical detector supporting the anode wires are Teflon inserts that are not included in the simulation, rather these spaces are left as open detection zones. Lastly, the aluminum holder supporting the foil in the simulation does not include small holes to optimize air flow while it is pumped to vacuum during sample implantation in the physical system. These differences between the simulation and physical systems are assumed negligible.

3.2 Evolution of Radiation Source

Along with the detector design changes, the simulated activity also went through several iterations. In the initial simulation, the radioactive source was a mono-energetic electron with 834 keV of energy emitted in a single direction. This source was a point source located either within or on one side of the foil.

The first change to the radiation source was to introduce an extra code which produces an allowed β energy spectrum specific to the isotope and transition. This β Decay Code was produced by the scientists at LLNL for the purpose of automating a predetermined number of events of different energies emitted isotropically. The range of possible energies is dependent on the isotope's Q value (maximum energy released during the decay) and the energy level populated by the daughter isotope after β decay. For each event, a value based upon the β energy spectrum (Fig. 3.4) would be randomly chosen to represent the particle's energy. Depending on the Q value of the reaction and the endpoint energy, the shape of the β spectrum is different for each transition and isotope being simulated. Shown in Fig. 3.4 for isotopes with different Q values, as the maximum β energy increases from 185 to 804 keV, the shape of the β energy spectrum changes, and the most probable value shifts from low energies toward higher energies. This shift is mainly attributed to the β particle's interaction with the nucleus, mathematically represented by the Fermi function.

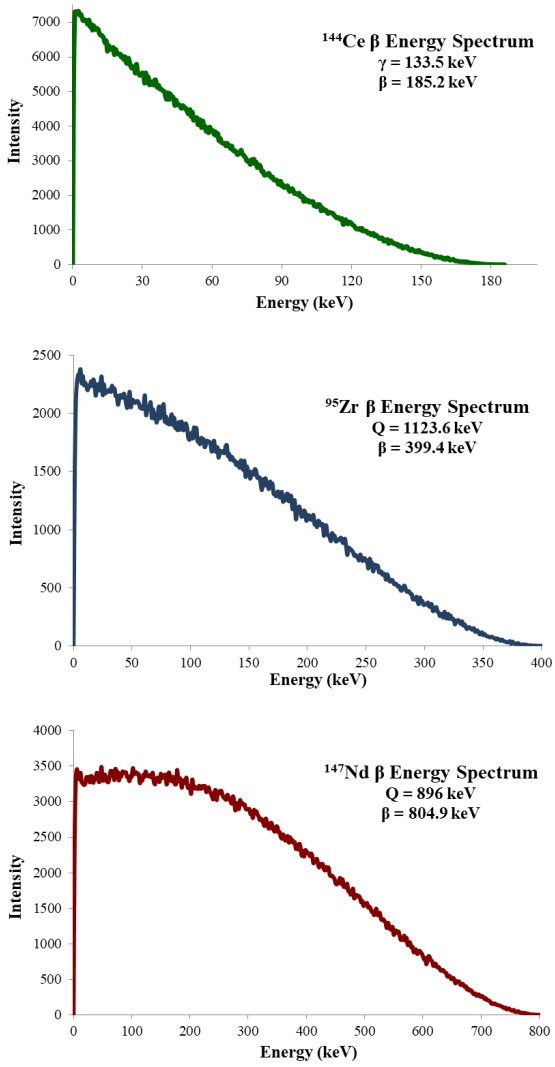

Figure 3.4: β energy spectra for the main transitions of ^{144}Ce, ^{95}Zr, and ^{147}Nd.

3.2.1 The β Decay Code and Fermi Function

The Fermi function of β decay handles the Coulombic interaction between the charge nucleus and the charged electron. If the decay occurs through emission of a β^+, the positive nucleus will accelerate the β^+ away due to the $+/+$ interaction. If the decay occurs through emission of a β^-, the positive nucleus will effectively slow the β^- as the two are attracted toward each other through the $+/-$ interaction. In both cases, the β particle's momentum is too large to be halted by the electromagnetic interaction rather it has the effect of skewing the β energy spectrum. The Coulombic interaction will have a greater effect on those particles emitted at lower energies which alters the shape of the β energy spectrum towards the higher energy if a β^+ or the low energy for a β^-.

The β decay code recreates this interaction between the nucleus and the charged particle by simulating the β energy spectrum unique for each isotope. The specific Fermi function values[51] are input into a text file. Both the screened and non-screened values are input into the code. Screening takes into account the damping of nuclear electrostatic field caused by the surrounding orbital electrons.

The values provided in literature have a minimum momentum of 0.1 ρ, which corresponds to an energy of $\sim$2.5 keV, with the next value occurring at 10 keV. While this minimum energy works for most isotopes, it is not accurate for those isotopes with a Q value below 1.0 MeV that have a large majority of β particles born within this energy range. Large gaps in tabulated values of the Fermi function at low energies lead to improper recreation of the β energy spectrum resulting in discrepancies between measured and simulated gas counter efficiencies.

The last major update to the radiation source was to alter the tabulated Fermi function values to include non-relativistic behavior for those β particles which are born at lower energies. The non-relativistic Fermi function was used to calculate the values at low energies

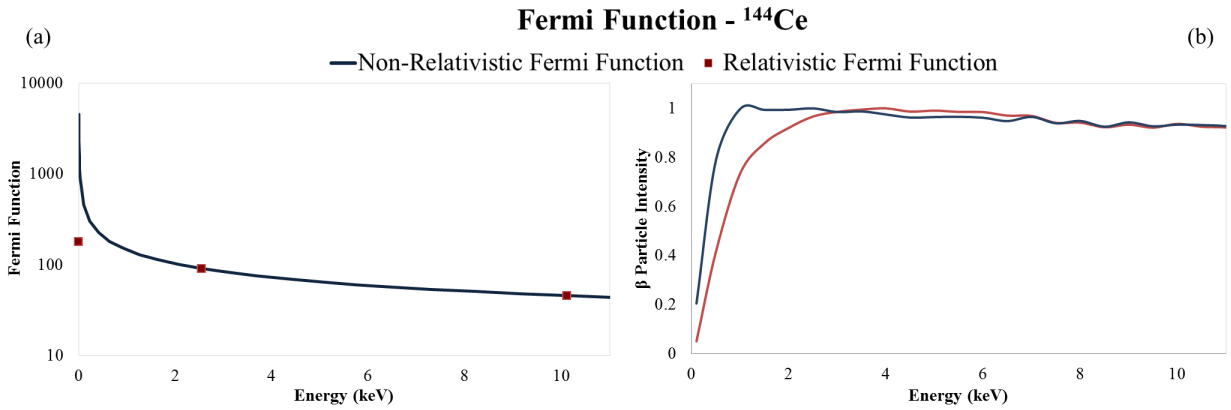

Figure 3.5: (a) Fermi function calculated for non-relativistic and relavistic β particles of ^{144}Ce and (b) the resulting β energy spectra for both relativistic and non-relativistic calculations.

(below 0.1 ρ):

$$F(Z,E) = \frac{2\pi\eta}{1 - e^{-2\pi\eta}} \tag{3.1}$$

Where $\eta = \frac{Ze^2}{\hbar\nu}$, Z is the proton number of the daughter isotope, e is the Coulombic charge in units of $MeV*m$, $\hbar$ is the reduced Planck constant in units of $MeV*s$, and ν is the velocity of the emitted electron. The calculated non-relativistic Fermi function is normalized to match the tabulated values. Shown in Fig. 3.5a, as the momentum decreases towards zero, the non-relativistic Fermi function increases towards infinity while the tabulated Fermi function values ends much earlier.

The resulting effect on the β energy spectrum is to increase the probability of particles born with low energies. Fig. 3.5b compares the non-relativistic and relativistic β energy spectra. One can see the non-relativistic line extending further into the low energy region than the relativistic line. While this is a small difference, the electronic threshold imposed during experimental measurements is within this region of difference, which effects the outcome of the simulations.

Within the β Decay Code, the forbiddenness of the decay is also varied. The level is determined by the spin state and parity of the parent and daughter nuclei. For allowed decays, the

spin state can change by 0 or ± 1 while the parity remains the same. For the first forbidden transition, the spin can change by 0, ± 1, or ± 2 while the parity can change. For specific isotopes, shape factors of the β spectrum can be used to represent allowed or forbidden decays[52,53]. This introduces a small level of skewness in the shape of the β energy spectrum, which is dependent on the specific transition the parent isotope undergoes.

Another feature of the β Decay Code is the ability to alter the type of particle. The most prevalent decay is the β particle emitted with a spectrum of energies. It is also possible for CE to be released during the decay. While both are electrons, the CE is emitted with a discrete energy equal to the excited energy state of the nucleus minus the binding energy of the electron in orbit. These mono-energetic electrons can be simulated alongside the β particle and the detector response recorded. As γ-rays are also released during decay, the simulation has the option to produce γ-rays of specific energies.

3.2.2 Radiation Size and Geometry

Once the details of the physics concerning the particle was determined, the radiation geometry was altered to fit the experiment. Initially, the geometry of the source was a point of radioactivity for the purpose of testing the simulation. The source then evolved to match measured sources created using the reactor and CARIBU facilities. For the reactor source, a foil of a specific material (e.g. zirconium) is irradiated with neutrons producing a foil which emits radiation from its entire volume. The shape of the foil is a cylinder with the diameter fixed at 0.952 cm and the height 1.31 μm.

Alternatively, the CARIBU radiation geometry is a thin, cylinder-sized shape of radiation placed inside a carbon foil a certain distance from one side (Fig. 3.6). The distance of the radiation from the outside of the foil is dependent on the ion travel speed and the isotope being implanted. The program SRIM[54] calculates the distance at which specific ions with

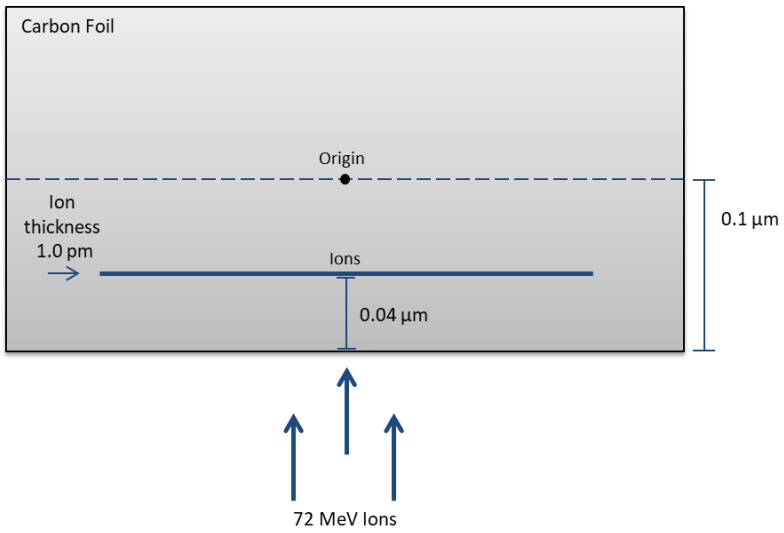

Figure 3.6: Placement of the simulated radioactive isotopes within the foil.

certain energies will travel into material. For the CARIBU sources, the foil material is carbon and the total travel energy is 72 keV (the ions are actually traveling with 36 keV, but have a +2 charge which propels them with 72 keV). The isotope being implanted is based upon the mass of interest and the most probable fission product produced from a ^{252}Cf spontaneous fission source. The diameter of the ion source is assumed to be 7.0 *mm* and is smaller than the foil diameter. During implantation at CARIBU, a 7.0 *mm* aperture is placed over the foil so as to minimize contamination to the sample holder and spread of ions. The thickness of the radiation is arbitrarily chosen to be 1.0 *pm*. In actuality, there is a small amount of depth variation of the sample implantation that is larger than 1.0 *pm*. The uncertainty attributed to the implantation depth is included in the uncertainty calculation of foil thickness.

3.3 Simulated Experiments

The simulation is used not only as confirmation for precision experiments, but also as a tool to further understand characteristics of the physical detector. An early experiment determined the foil material to be used at CARIBU. This foil needed to be made of material

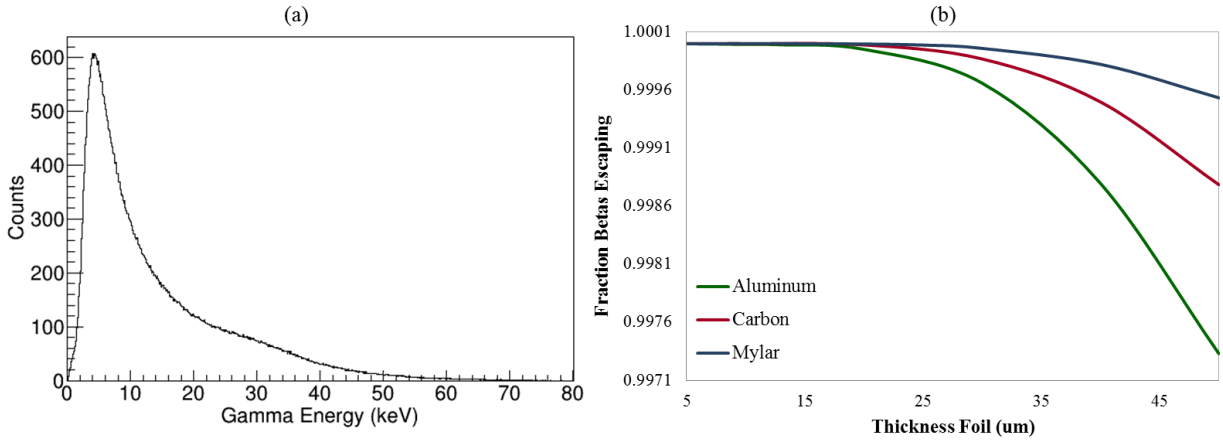

Figure 3.7: (a) Deposition of energy spectrum produced from GEANT4 simulations. (b) Simulation to determine the material response to radioactive ions and the level of attenuation each imposes on β particles.

rugged enough to be pumped from atmospheric pressure to vacuum, but thin enough to emit a large fraction of the particles into the detector space. The most common material used for low attenuation experiments are aluminum, Mylar, and carbon. These foils were simulated using different thicknesses in order to understand the radiation response to these materials. For each simulated event, β particles deposit some energy within the detection space which can be transformed into a histogram to determine the most probable energy being deposited (Fig. 3.7a). Fig. 3.7b shows a graphical representation of entries detected within the gas as a function of foil thickness (μm) for each of the foil materials.

Mylar shows the best response for a given thickness based on its low interaction with β particles. However, in order to optimize the gas counter efficiency, the foil thicknesses must be minimized. At a thickness of less than several micrometers, Mylar becomes difficult to work with and tearing the foil is a large concern. During source collection at the CARIBU facility, the source foil is pumped from atmospheric pressure to vacuum and back again, so it needs to survive pressure changes. Based on these considerations, carbon was chosen as the best material for the sample foil due to its relative ruggedness at micrometer thicknesses under these conditions.

Next, a multiscattering parameter was varied to see the effects on the simulation. The multiscattering parameter determines how the particle behaves after a step[48]. It determines the path length, scattering direction, and lateral displacement based on the Lewis Theory. The carbon foil is less than 1.0 μm, if the particle's step is a large fraction of this thickness, the simulation may not be properly handling the deposition of energy. The multiscattering parameter was varied between 0.005 and 0.5 (default value is 0.04). At low values of multiscattering, the effect is minimal on the gas counter efficiencies. As the value increases toward 0.5, the efficiencies changed more drastically because relatively large steps were taken that miscalculated the energy deposited and direction of the particle within the gas counter. The default value of 0.04 was determined to be sufficient for these calculations.

For the purpose of confirming the results of the simulation, tests were performed with the sample foil: a foil of infinite thinness, a foil with exaggerated thickness, a point source located in the center of the foil, and a point source located on one side of the foil. In all cases, the individual detector sides were compared as well as the total detector response.

For a foil of both infinitely small thickness and exaggerated thickness, the idea was to determine the effects of the self-attenuation between the implanted radiation source and the foil material. Both simulations included a carbon foil with the radiation located at the center and a simulated β energy spectrum with a maximum value of 400 keV. For infinitely small thickness, a simulation was performed with a 1.0 pm thick foil. The results indicate 100% detection efficiency when an electronic threshold was not imposed and equal responses for either side of the chamber. Conversely, for a foil that has an exaggerated thickness of 10.0 mm, no energy was deposited within the detection space because all β particles were absorbed within the thick foil. In both cases, the simulation results agreed with the theorized detector response suggesting, for these basic cases, the simulation is accurately representing the systems it models.

Table 3.1: Gas counter detection efficiency for x-rays and γ-rays of generic energies.

Efficiency of x-rays and γ-rays in Gas Counter				
Energy (keV)	$>$ 1.0 keV	$>$ 1.5 keV	$>$ 2.0 keV	$>$ 3.0 keV
1	7.62%	0.00%	0.00%	0.00%
3	0.99%	0.96%	0.94%	0.91%
5	0.26%	0.25%	0.24%	0.22%
10	0.10%	0.09%	0.09%	0.09%
100	0.01%	0.01%	0.01%	0.01%
500	0.02%	0.02%	0.01%	0.01%
1000	0.03%	0.03%	0.03%	0.02%

Radiation source location with respect to the foil was also investigated in order to compare the responses of the detector sides. An isotropic radiation source located at the center of the foil which is at the center of the detector should emit radiation equally to both sides of the detector. If, however, that radiation source was placed to one side of the foil, half of the radiation would need to traverse the full foil thickness to deposit energy on the far side of the detector. As a result, one side of the detector should have fewer counts than the other side. In both cases, the detector provided simulated results which aligned with the understanding of the system.

One of the last major tests performed investigated the effect of x-rays and γ-rays during detection. γ-rays are emitted with discrete energies and are not affected by Coulombic interactions like β particles. As such, they do not interact with the nucleus after emission. The energy deposited is independent of the state of the nucleus. Methane gas was specifically chosen as the detection gas due to its minimal interactions with x-rays and γ-rays. A simulation was performed with monoenergetic x-rays and γ-rays of varying energies from 1.0 to 1,000.0 keV emitted from a 0.2 μm-thick carbon foil (Table 3.1). The interaction between x-rays and methane gas is minimal. Interactions with γ-rays are even less. These simulations confirm the majority of energy deposited within the gas counter is not largely attributed to x-rays and γ-rays.

3.4 Analysis of Simulated Output

In order to gain useful knowledge which can be directly compared to measured results, the output of the simulation requires further analysis. Electronic thresholds, feeding states, CEs, and detector responses of individual sides need to be included when comparing simulated and measured results.

The output of the simulation gives a list of energies and a histogram of either side of the detector displaying the energy deposited per each simulated event. The list of energies is summed to give the total energy deposited per event. Thresholds are imposed on the energy deposition restricting those energies which would not be detected in the measurement due to some electronic threshold specific to the system. The threshold of the simulation would be altered to best align with the measured data. Those events which deposit energy above the threshold are counted then divided by the total events simulated to determine the gas counter efficiency. Simulated efficiencies are compared with measured gas counter efficiencies for different transitions.

In the simplest case, a β particle populates an energy level and decays to the ground state by emission of a γ-ray. As γ-rays do not deposit an appreciable amount of energy in the detector, they are effectively ignored. This transition can be recreated by a single simulation of which the analysis has been described in the previous paragraph.

In more complex decays, a β particle may populate an excited state which then may feed into other excited states and/or release conversion electrons. There are multiple pathways for the decay to occur by and each specific pathway needs to be simulated and analyzed separately. Also, conversion electrons are detected by the gas counter and generally have much higher energies than β particles as they are emitted with discrete energies instead of a spectrum of energies.

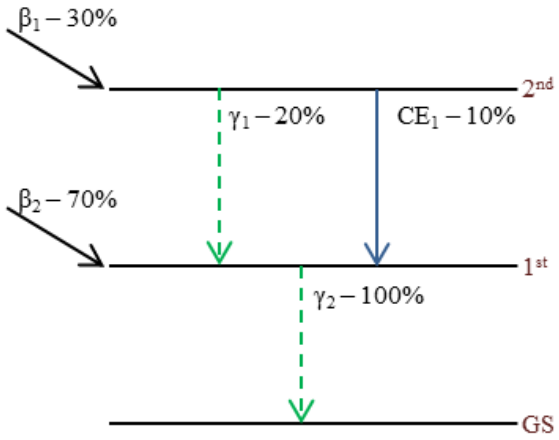

Figure 3.8: Simplified example of a decay scheme and possible pathways to ground state (GS).

In cases where there are multiple possible pathways for a decay to populate to the ground state (GS), transition specific probabilities are calculated. This is performed by attributing a specific probability to each possible transition. For example, Fig. 3.8 shows a simplified decay scheme in which a β decay (β_1 or β_2) can populate two excited states (2^{nd} and 1^{st}). The 2^{nd} excited state can decay by emission of a γ-ray (γ_1) or a CE (CE_1) to 1^{st} excited state which decays to the GS by emission of a different γ-ray (γ_2). In total, there are three possible transitions:

$$(1)\ \beta_1 \rightarrow \gamma_1 \rightarrow \gamma_2 \rightarrow GS\ 20\%$$

$$(2)\ \beta_1 \rightarrow CE_1 \rightarrow \gamma_2 \rightarrow GS\ 10\%$$

$$(3)\ \beta_2 \rightarrow \gamma_2 \rightarrow GS\ 70\%$$

whose absolute probability depends on combinations of each individual probabilities. One major distinction should be made between feeding and direct population of the 1^{st} excited state. Those β particles which populate the 2^{nd} excited state will have a different β energy than those β particles which populate the 1^{st} excited state, and they will also have different gas counter efficiencies. Thus, if one wants to determine the simulated efficiency and compare it to the measured efficiency ($\varepsilon_\beta = R_{\beta\gamma}/R_\gamma$), the specific combinations of different β particles need to be accurately taken into account.

A separate simulation is required for β particles with different end-point energies and CEs. CEs have discrete energies unlike β particles that are emitted with a variety of possible energies according to the β energy spectrum. In the example discussed above, β_1 and CE_1 would be simulated separately then both energy depositions would be added to create the total energy deposited per event. The physical detector does not have the ability to resolve a single transition which emits both a β particle and a CE (because they are emitted close in time), resulting in the total energy deposition being a sum of the β particle and CE energy. Effectively, CE_1 offers another opportunity to detect an event if β_1 was missed. This will increase the gas counter efficiency for the transition. Generally, a CE will have a high probability of being detected due to its discrete energy and its high probability to overcome attenuation within the carbon foil.

Analysis is performed for both individual sides and the sum of both sides. During the experimental measurement, the gas counter is unable to resolve one event that deposits energy in both sides of the gas counter. For example, if a β decay populates an energy level which then emits a CE causing energy to be deposited in both detector sides, the total energy deposition is summed. The total number of detector events (those events which have deposited some energy in either side of the detector) is divided by the total events simulated to determine the β efficiency of the simulated transition. Throughout the measurements, either detector side could be powered resulting in β efficiencies of a 2π system rather than a 4π system. While not used strictly for the calculation of γ-ray branching ratios, it is a good use of diagnostics of the system and source. The simulation is used to validate several responses detected during measurement such as discrepancies between detector sides and radioactive source depth within the carbon foil.

Chapter 4

Method Viability - ^{95}Zr

^{95}Zr is routinely used as cladding for nuclear reactor fuel due to its relatively low cross section for neutron absorption[55], anti-corrosive properties, and reliable strength at high temperatures[56]. Furthermore, its desirable properties also have applications in the field of pyrotechnics[57,58], structural materials[59], armament[60], and chemistry[61,62].

4.1 ^{95}Zr/^{95}Nb Overview

^{95}Zr was chosen to test this method due to its well-known branching ratios of both parent and daughter (^{95}Zr and ^{95}Nb), relatively long half-lives of 64 days and 35 days, and simple decay schemes. These isotopes can help determine the level of precision available through the implementation of this technique to more complex isotopes. Mass chain 95 is produced from fission of ^{252}Cf and can be readily created at the CARIBU facility at ANL. Calculations of γ-ray branching ratios can be determined from measurements of only γ-rays, without the need of more complex measurements to further confirm the results of the experiment.

4.1.1 CARIBU Source Production

The fission yield of mass 95 (Fig. 4.1) from ^{252}Cf is relatively high, with a total deliverable rate from CARIBU of 3×10^6 ions/sec[3]. The highest directly-yielding isotopes are ^{95}Rb, ^{95}Sr, and ^{95}Y which make up 1.24% fission yield[1]. The half-lives of each isotope are on the order of 10.3 minutes or less[9]. After a few hours, the only isotope remaining will be ^{95}Zr and its daughters. The CARIBU beam delivers +2 ions at a speed of 72 keV to the implantation foil. Using the program SRIM[54], the calculated penetration depth of ^{95}Sr ions into a carbon foil is 23.2%.

An HPGe is set up to measure the cross attached to the beam at the junction where the ions are implanted. Before the measurement, calibration sources of ^{152}Eu, ^{60}Co, and ^{137}Cs are placed inside the cross and the efficiency of the HPGe at this position is determined. These measurements are used to gauge the beam intensity and total amount of ions deposited at the implantation site over the course of collection. The most intense peaks from the decay of ^{95}Sr and ^{95}Y are monitored. ^{95}Sr has a γ-ray peak at 685.6 keV with intensity of 22.6% and ^{95}Y has a γ-ray peak at 954 keV with intensity of 15.8%[9]. From peak areas, one can determine the activity of the sample during collection:

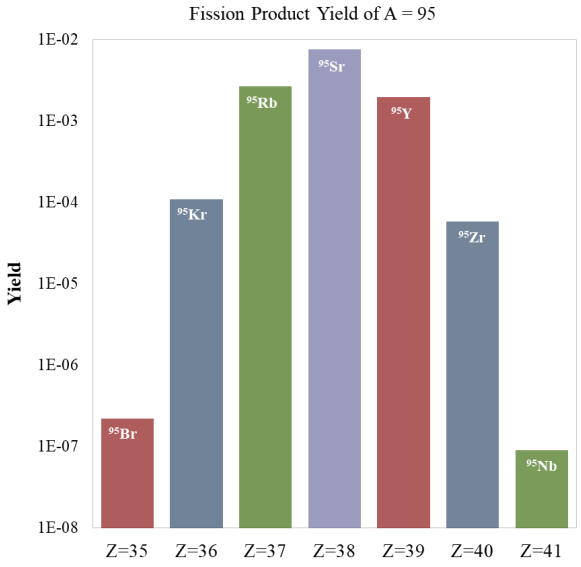

Figure 4.1: Mass 95 fission product yield from ^{252}Cf[8].

$$A_{Zr} = \frac{Peak\ Area}{I_\gamma * \varepsilon_\gamma} * \lambda_{Zr} = N_{Zr}\lambda_{Zr} \tag{4.1}$$

Where I_γ is the γ-ray intensity, ε_γ is the detector efficiency for the specific γ-ray, and λ_{Zr} is the decay constant. Depending on the beam strength at CARIBU and the desired activity of the sample ($\sim$ 100+ Bq), collection can take from one to five days of constant implantation.

Table 4.1: Literature branching ratios for γ-rays and β particles[9].

	γ-ray Energy (keV)	γ-ray Branching Ratio	$E_{\beta_{max}}$ Energy (keV)	β Branching Ratio
^{95}Zr	724.192	0.4427(22)	399.4	0.4434(22)
^{95}Zr	756.725	0.5438(22)	366.9	0.5446(22)
^{95}Zr			887.9	0.0108(7)
^{95}Nb	765.803	0.99808(7)	159.8	0.99970(6)

4.1.2 Decay Scheme

The simplicity of the decay scheme is one of the key reasons this isotope was chosen to validate this method. Both γ-ray and β particle intensities are large and well-known, requiring little difficulty for detection and analysis. Listed in Table 4.1 are the main γ-ray and β particle transitions, which are accounted for in both measurement and simulations.

Looking at the decay scheme for ^{95}Zr (Fig. 4.2, $t_{1/2}$ = 64.032(6) days), each of the decays populate the ground state with no feeding from higher states. The majority of the β particles from the decay of ^{95}Zr are released with energies 366.9 and 399.4 keV. From these emissions, two excited states are populated, 756.78 and 724.2 keV. These excited states decay to the ground state and release the full energy in the form of a γ-ray. These two transitions make up 98.80% of all ^{95}Zr decays. The next most probable transition is β decay to an isomeric state at 235.7 keV, which decays at a different rate ($t_{1/2}$ = 3.61(3) days). Within this isomeric state decay, 94.4% of the emissions decay by isomeric transition (IT) and the remaining 5.6% decay directly to the ground state of ^{95}Mo. Of those transitions that decay by IT, 69.43% release a conversion electron in place of a γ-ray and 24.8% release a γ-ray. Those internal conversion transitions go on to populate the ground state of ^{95}Nb, which further decays to stable ^{95}Mo. The overall interference from the isomeric state is minimal with the correction to the overall scheme totaling 1.08%. Finally, within the ^{95}Zr decay scheme, there is a small percent of the decays that populate the ground state directly, releasing only the original β particle and no γ-ray (0.103%).

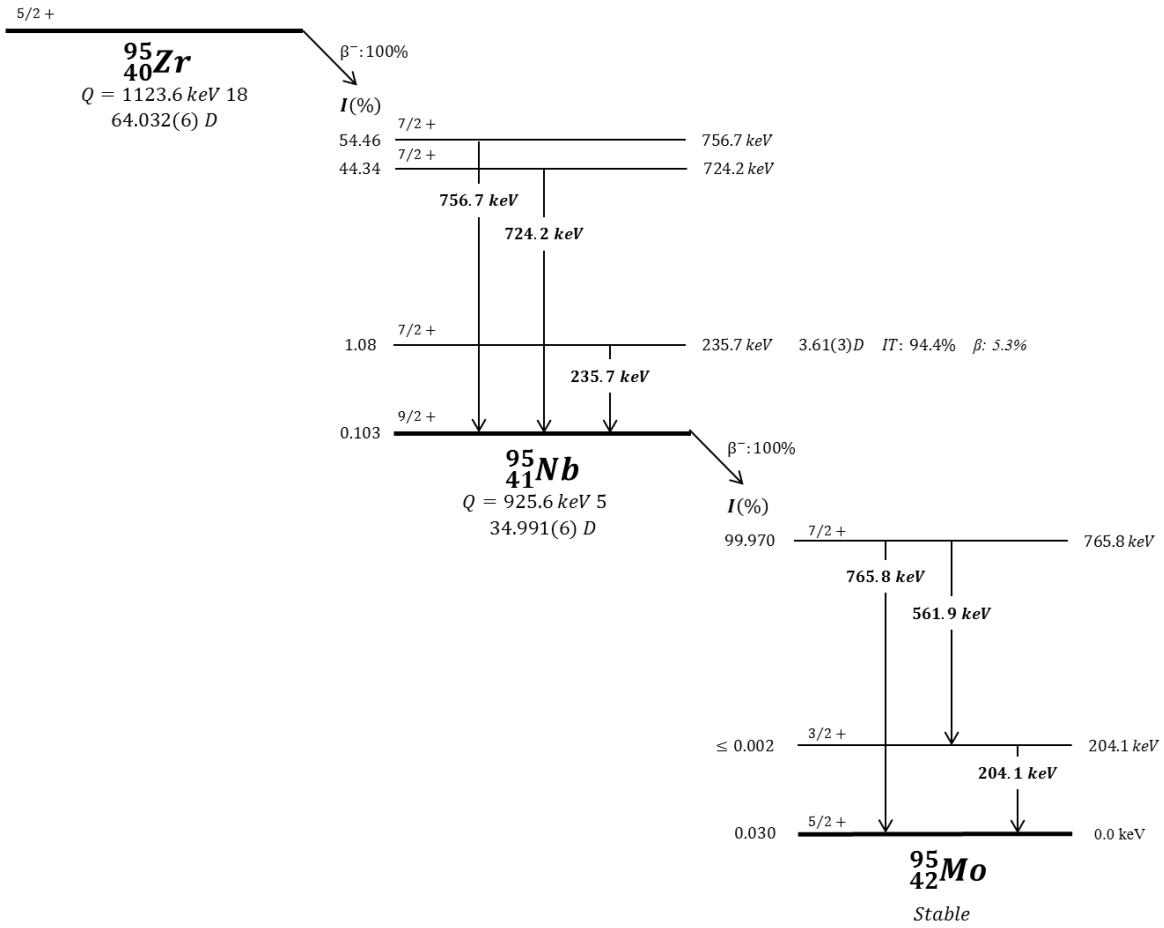

Figure 4.2: A simplified decay scheme exhibiting the major transitions of ^{95}Zr decaying to ^{95}Nb decaying to ^{95}Mo. The decay to the isomeric state of ^{95m}Nb is also seen at the 235.7 keV energy level.

The daughter, ^{95}Nb, is readily detected from its main transition of a γ-ray with a similar energy to that of the ^{95}Zr γ-rays. The Q value of ^{95}Nb is 925.6 keV with a half-life of 34.991(6) days. The main population of the 765.8 keV excited state comes from emission of a 159.8 keV β particle (99.970(6)%). De-excitation to ground state occurs by emission of a 765.8 keV γ-ray. There are two other transitions, one which comes as a result of β decay population of the excited energy level and another which is a result of feeding from a higher state energy level. In either case, the transitions occur with a probability of less than 0.1% and are not readily detected.

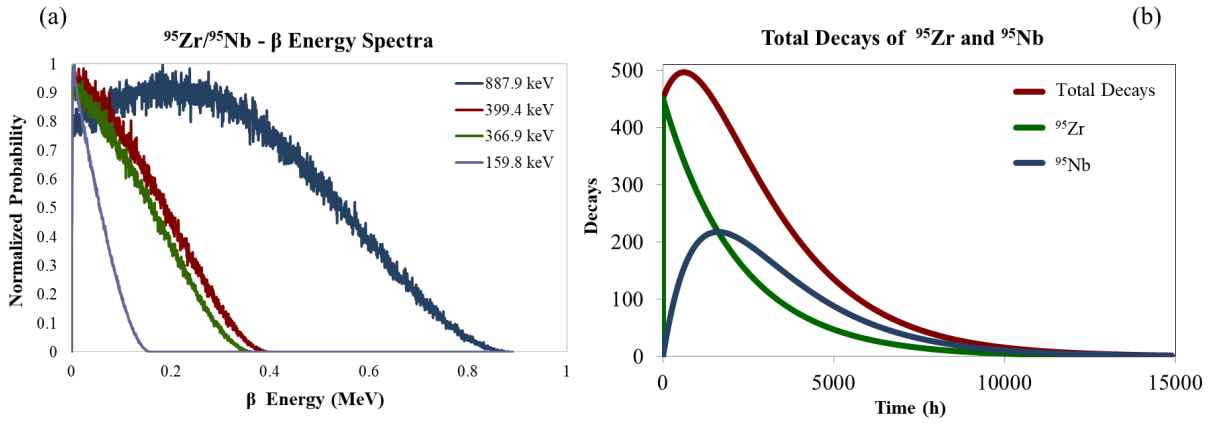

Figure 4.3: (a) Major β transitions for ^{95}Zr and ^{95}Nb and (b) decay of the source over time.

4.1.3 Simulated β Energy Spectrum

Due to transitions which populate various energy levels, different end-point energies occur in the decay of ^{95}Zr/^{95}Nb resulting in different shapes of the β energy spectra. In general, the higher the end-point energy the more skewed the spectrum will be toward higher energies. Simulated β energy spectra of the four major transitions are shown in Fig. 4.3a. For those transitions with low end-point energies (e.g. $E_{\beta_{max}} = 159$ keV), a large number of β particles are born at low energies resulting in a spectrum that is skewed toward the low energy. Conversely, those transitions with large end-point energies (e.g. $E_{\beta_{max}} = 889.7$ keV) result in a spectrum whose most probable energy is much higher.

4.1.4 Half-lives of ^{95}Zr/^{95}Nb

Both ^{95}Zr and ^{95}Nb have relatively long half-lives allowing for multiple measurements to take place before the source decays. ^{95}Nb decays into a stable ^{95}Mo at which point, no further radioactivity is emitted. Depending on the time between collection and measurement, the ratio between the daughter and parent can differ. Transient equilibrium is reached after about 200 days (Fig. 4.3b). Before this occurs, ^{95}Zr decays into ^{95}Nb, which will decay at

a faster rate. Effectively, the source can become more active than when it was first created due to the growth of the more active daughter, after which, the source will decay with a half-live that is a combination of the parent and daughter.

4.1.5 Simulated Gas Counter Efficiency

Simulated results are used to predict the gas counter's efficiency for measuring β particles and CE emitted by the source. Experimental determination of gas counter efficiency relies on $\beta\gamma$ coincidence and γ-ray measurements which give transition-specific gas counter efficiencies. There are two sets of simulated results for the two different types of ^{95}Zr sources: reactor-produced and CARIBU-produced. The two differ substantially in source thickness, source material, and radiation geometry. The irradiated source was made by putting enriched ^{94}Zr foil of 1.31 μm thickness into a nuclear reactor thereby creating an entire radioactive zone which encompasses the metal foil. The CARIBU source was created by implanting mass 95 ions into an ultra-thin carbon foil thereby localizing the radiation to a small fraction of the thin carbon foil. In either case, the results of the simulation vary depending on the type of source being used.

4.1.6 Reactor-Produced Source

The simulation assumes an irradiated foil of ^{95}Zr with an experimentally determined thickness (as opposed to manufacturer quoted thickness) with radiation originating at any point within the foil geometry. Various thresholds were imposed on the simulated data so that it better matched measured values. Three main transitions were simulated: $E_{\beta_{max}} = 366.9$ keV β particle gated on a 756.7 keV γ-ray, $E_{\beta_{max}} = 399.4$ keV β particle gated on a 724.2 keV γ-ray, and $E_{\beta_{max}} = 159.8$ keV β particle gated on a 765.8 keV γ-ray. Less intense transitions

Table 4.2: Simulated results for gas counter efficiency of a 1.31 μm reactor-made ^{95}Zr source.

	Total Entries	$\geq$ 0.5 keV	$\geq$ 1.0 keV	$\geq$ 1.5 keV	$\geq$ 2.0 keV
Efficiency when Gated on 724.2 keV γ-ray	0.8917	0.8910	0.8900	0.8877	0.8797
Efficiency when Gated on 756.7keV γ-ray	0.8791	0.8784	0.8774	0.8754	0.8691
Efficiency when Gated on 765.8 keV γ-ray	0.6953	0.6948	0.6941	0.6930	0.6914

were negated for the purposes of this simulation. The results of the simulation are shown in Table 4.2.

With a foil thickness of 1.31 μm and no threshold, gas counter efficiencies are immediately reduced. This suggests the β particles are highly attenuated by the zirconium foil material. The efficiencies for both ^{95}Zr and ^{95}Nb decrease when thresholds are placed on the data, but more so for the higher energy β particles of ^{95}Zr. This trend suggests that for higher energy β particles, the total amount of energy deposited within the chamber per event is low and unable to overcome the threshold. Conversely, the lower energy β particle of ^{95}Nb is less affected by the increasing threshold suggesting more total energy is deposited per event.

4.1.7 CARIBU-Produced Source

The source created at CARIBU consists of a carbon foil of thickness 40 ± 4 $\mu g/cm^2$ with radiation of 7.0 mm diameter implanted 41.2 nm into one side. The simulation assumes a radiation implantation thickness of 1.0 fm. In addition to the three main β particle transitions ($E_{\beta_{max}}$ = 366.9 keV particle gated on 756.7 keV γ-ray, $E_{\beta_{max}}$ = 399.4 keV particle gated on 724.2 keV γ-ray, and $E_{\beta_{max}}$ = 159.8 keV particle gated on 765.8 keV γ-ray), the β population of the isomeric state of ^{95m}Nb was also taken into account. This transition pro-

Table 4.3: Simulated results for gas counter efficiency of a 0.2 μm CARIBU-made ^{95}Zr source.

Total Detector Response	0.0 keV	$\geq$ 0.5 keV	$\geq$ 1.0 keV	$\geq$ 1.5 keV	$\geq$ 2.0 keV
Efficiency when Gated on 724.2 keV γ-ray	0.9783	0.9770	0.9739	0.9689	0.9571
Efficiency when Gated on 756.7 keV γ-ray	0.9757	0.9745	0.9715	0.9667	0.9568
Efficiency when Gated on 765.8 keV γ-ray	0.9338	0.9327	0.9300	0.9251	0.9188
Efficiency when Gated on 887.9 keV γ-ray	0.9934	0.9911	0.9852	0.9635	0.9100
Side A	0.0 keV	$\geq$ 0.5 keV	$\geq$ 1.0 keV	$\geq$ 1.5 keV	$\geq$ 2.0 keV
Efficiency when Gated on 724.2 keV γ-ray	0.5182	0.5163	0.5129	0.5084	0.5006
Efficiency when Gated on 756.7 keV γ-ray	0.5185	0.5165	0.5132	0.5086	0.5015
Efficiency when Gated on 765.8 keV γ-ray	0.5175	0.5152	0.5110	0.5045	0.4975
Efficiency when Gated on 887.9 keV γ-ray	0.5152	0.5126	0.5085	0.4963	0.4684
Side B	0.0 keV	$\geq$ 0.5 keV	$\geq$ 1.0 keV	$\geq$ 1.5 keV	$\geq$ 2.0 keV
Efficiency when Gated on 724.2 keV γ-ray	0.4872	0.4859	0.4838	0.4806	0.4742
Efficiency when Gated on 756.7 keV γ-ray	0.4853	0.4841	0.4820	0.4790	0.4735
Efficiency when Gated on 765.8 keV γ-ray	0.4592	0.4579	0.4556	0.4521	0.4481
Efficiency when Gated on 887.9 keV γ-ray	0.4969	0.4950	0.4918	0.4807	0.4537

duces a β particle with an end-point energy of 887.9 keV (1.08%), which is not in coincidence with a γ-ray due to the population of an isomeric state. This isomeric state can decay by emission of an additional CE with roughly 216 keV discrete energy or a γ-ray of energy 235.7 keV. A small fraction will emit another β particle that is not included in the simulations as the absolute probability of emission is small ($\sim$0.06%). Effectively, these transitions are not seen (no coincident $\beta\gamma$ correlation) in the measured coincidence data and only contribute to the total number of counts in the gas counter and total source efficiency.

The results of the simulation are shown in Table 4.3. Several thresholds are imposed on the simulated data so that it represents the measured data with more accuracy. Included with the gas counter efficiencies for the total detector are the efficiencies for each side of the detector. The CARIBU source has the radioactive ions implanted in a small fraction of the foil's thickness. As such, there is an asymmetry between the different sides of the detector. This can be an important check during the measurement to verify the accuracy of the gas counter response.

4.2 ^{95}Zr Reactor-Produced Source Measurement

Production of radioactive sources using nuclear reactors are initially used to study the gas counter before CARIBU experiments are performed. An enriched source of ^{94}Zr was created using the TAMU nuclear reactor. The main benefit of a reactor-made source is the high level of activity that can be produced. However, there are several limitations of this method of production that result in higher uncertainties. Any contamination present within the enriched source as a result of its production method could interfere with the measurement resulting in large corrections to the final values. Furthermore, the density and thickness of the Zr foil add to the uncertainties. A higher density of the foil causes more attenuation of the β particles causing lower detection efficiencies. Thicknesses of manufactured thin foils are

quoted with uncertainties of ±25%! Regardless of the limitations, these initial measurements go a long way to characterize the gas counter and simulated responses.

Natural zirconium has several stable isotopes (^{90}Zr, ^{91}Zr, ^{92}Zr, ^{94}Zr, and ^{96}Zr) that can become radioactive when exposed to neutron radiation. ^{94}Zr has a fractional abundance of 0.1738(28)[63] and becomes ^{95}Zr after absorption of a neutron. While activation of natural Zr does result in neutron absorption of all natural isotopes, only ^{93}Zr, ^{95}Zr, and ^{97}Zr become radioactive. Of these, ^{93}Zr has the longest half-live of $1.53\,(10) \times 10^6$ years, which can be corrected for and will not contribute much activity over a measurement period. The other activated isotope, ^{97}Zr, has a half-life of 16.744(11) hours requiring about a week to fully decay. While several irradiations were performed using natural Zr, the low fractional abundance and the relatively large amount of Zr needed make this source inefficient for initial measurements.

Enriched ^{94}Zr was purchased for reactor source production. Neutron capture cross sections for thermal and resonance neutrons are 0.052± 0.003 and 0.30± 0.03 barns[55], which is quite low and would require 24 hours of irradiation at TAMU reactor to produce 0.2 μCi of activity. The TAMU nuclear reactor was selected for this experiment due to the large neutron flux and relatively short irradiation time needed to produce a high activity source.

An enriched ^{94}Zr sheet (25×25 mm) was purchased from the company Goodfellow at a quoted thickness of 1.00(25) μm with 99.2% purity. A collaborator from the University of California Berkeley, B. Champine, performed additional tests[64] on the thickness of the foils and found an absolute thicknesses of 1.31(10) μm. From the enriched sheet, a small circle was punched creating a foil with a diameter of 0.9525 mm. This foil was punched to this size so that it would sit within the source holder open space of 1.0 cm without any overlap between the holder and foil. The foil was held in place by 12.7 μm gold-plated tungsten wires.

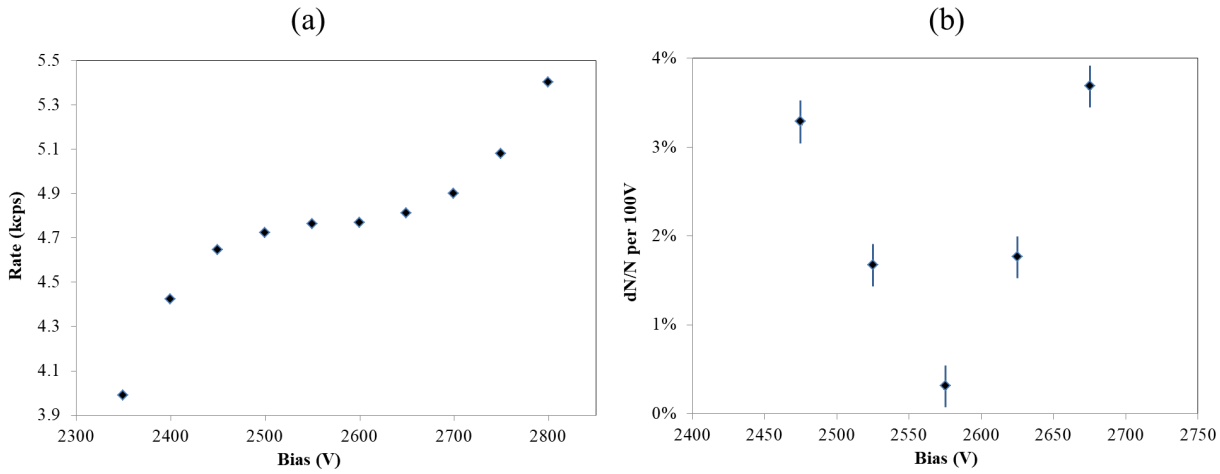

Figure 4.4: (a) Voltage plateau and (b) change in counts per 100V.

Table 4.4: Manufacturer quoted limits of contaminates within an enriched ^{94}Zr foil.

Element	ppm
C	250
Hf	2500
Fe	200
Cr	200
N	100
O	1000
H	10

Quoted contaminants within the foil are shown in Table 4.4. Of these elements, the most worrisome arises from irradiation of hafnium. While several isotopes of natural Hf exist, only ^{180}Hf would activate to a large degree due to its relatively high fractional abundance (∼35%) and large thermal neutron capture cross section (104.5 barns)[1]. Its half-life of 42.4 days is comparable to ^{95}Zr which implies it will decay at a similar rate. The level of impurity within the source can be quantified by measuring the emitted γ-ray at 133.0 keV with a γ-ray branching ratio of 43.3(5)%[9].

With this in mind, the enriched foil of ^{94}Zr was irradiated for 24 hours, left to decay for 15 days, and measured for 1.6 days. The activity of the source was determined to be 2.67 kBq from measurements of the source within the gas counter.

Just before the measurement, the gas counter's optimal voltage was determined by performing a voltage plateau (Fig. 4.4a). The voltage was increased by 50 V and measured for 5

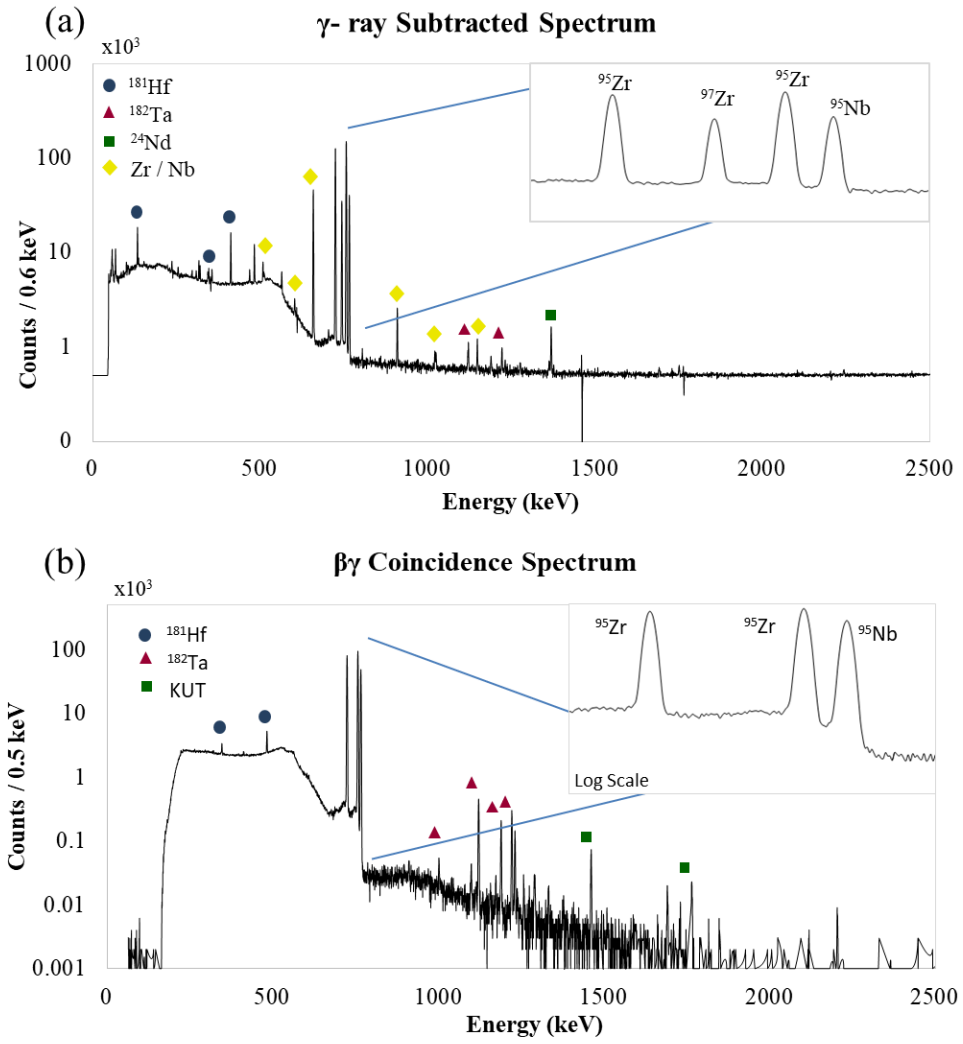

Figure 4.5: (a) Background-subtracted γ-ray spectrum and (b) $\beta\gamma$ coincidence spectrum measurement of a reactor-produced source.

minutes over the range of $2350 - 2800\ V$. The rate of change over $100\ V$ was calculated (Fig. 4.4b). The center of the voltage plateau occurs at $2575\ V$ and was the voltage chosen to perform the measurements.

Fig. 4.5a shows the measured γ-ray spectrum after background subtraction and Fig. 4.5b shows the $\beta\gamma$ coincidence spectrum. Many isotopes were discovered along with the ^{95}Zr/^{95}Nb lines including ^{59}Fe, ^{181}Hf, ^{182}Ta, ^{192}Ir, ^{194}Ir, ^{197}Au, and small traces of ^{97}Zr/^{97}Nb. These contaminates reduce the benefits of a reactor-produced source to determine the γ-ray branching

Table 4.5: Simulated and measured results for gas counter efficiency of a 1.31 μm reactor-made ^{95}Zr source. A threshold of 1.5 keV was imposed on the simulation results to best match measured results.

	β Energy (keV)	GEANT4	Measured
Efficiency when Gated on 724.2 keV γ-ray	399.4	0.8877	0.8807(87)
Efficiency when Gated on 756.7keV γ-ray	366.9	0.8754	0.8733(74)
Efficiency when Gated on 765.8 keV γ-ray	159.8	0.6930	0.7099(164)

ratio with high certainty and is the main reason it was not chosen as the source to validate this method. The corrections that would have to be applied to determine the contribution to the measured β values associated to only ^{95}Zr would have been too challenging and low uncertainties would not be achieved. Further source processing could be performed to isolate the ^{95}Zr/^{95}Nb series by dissolving the source and separating out the Zr content, however, this was not further pursued.

While this source is not ideal for γ-ray branching ratios calculations, useful information can be gained from measurement of this source. Taking the ratio of $\beta\gamma$ coincidences to γ-ray peak areas, gas counter efficiencies can be calculated and compared to GEANT4 simulations for the three major transitions of ^{95}Zr/^{95}Nb (Table 4.5). An electronic threshold of 1.5 keV was imposed on the simulated data, which includes only those events that deposited 1.5 keV of energy or greater. Comparing the two sets of efficiencies, there is rather good agreement considering the large amount of variables mentioned previously. These efficiency values suggest that both the model created by GEANT4 and the gas counter are responding in a realistic manner.

The use of a Zr foil with a density of 6.49 g/cm^3 and Z value of 94 result in relatively low gas counter efficiency values due to the greater attenuation of β particles unable to escape the foil

material before being absorbed. Looking at the trend of β energy to efficiency, one can see the efficiency goes down as the $E_{\beta_{max}}$ energy decreases. Again, this can be attributed to more interactions of the low energy β particles with the Zr foil leading to higher attenuation. The electronic threshold plays a small role in eliminating those β particles that deposit energy indistinguishable with noise at low energy levels.

Confirmation of literature γ-ray branching ratios can be indirectly compared by calculating the ratios of the two ^{95}Zr peaks 724.2 and 756.7 keV. The literature values and the peak areas found in the measured γ-ray spectrum (corrected for γ-ray efficiencies) should agree well if the literature values are to be believed. The measured γ-rays are relatively unaffected by attenuation in the surrounding material and the high certainty of the HPGe lead to a reliable measurement of the γ-ray ratios. Literature values for the 724/767 ratio are 0.8110(24)[65] and measured values are determined to be 0.8112(28), which is in exact agreement.

For the isomeric state of ^{95m}Nb, there are questionable literature values for the β and γ-ray branches that may be improperly assigned. Using the γ-ray spectrum, it is possible to see a peak at 204.1 keV with a 2.30% γ-ray branching ratio attributed to the isomeric β decay de-excitation populating the ground state of ^{95}Mo and a peak at 235.7 keV with a 24.8% γ-ray branching ratio attributed to isomeric de-excitation populating ^{95m}Nb ground state. Literature values[9] give a 204/235 ratio of 0.094(34) and measured data results in a ratio of 0.061(41), which assigns a limit to the contribution of ^{95m}Nb and confirms literature values are in the proper range. The contribution of the isomeric state is not over exaggerated in literature.

4.3 ^{95}Zr CARIBU-Produced Source Measurements

4.3.1 Initial Measurement of ^{95}Zr

The first measured source created at CARIBU was an initial test of the full method and the systems involved. It confirmed the viability of the technique and gave a preview of the analysis needed to calculate the γ-ray branching ratios for a CARIBU source using instrumentation intended for precision analysis.

From ^{252}Cf spontaneous fission, the majority of mass 95 ions are produced as ^{95}Sr and ^{95}Y, which will then fully decay to ^{95}Zr after a few hours. Beam implantation of mass 95 spanned 33 hours starting March 20, 2016. A spectrum was taken every 15 minutes and the peak areas of the most intense peaks from ^{95}Sr and ^{95}Y were monitored. ^{95}Sr has a γ-ray peak at 685.6 keV with a decay intensity of 22.6(12)% and ^{95}Y has a γ-ray peak at 954 keV with a decay intensity of 15.8(7)%. Fig. 4.6a shows the summed spectra taken over the length of implantation, with the two main γ-ray lines used to monitor the beam labeled in blue.

Analysis of this monitoring spectrum suggests there are no contaminates other than the mass 95 chain and background. A search was performed for low intensity γ-ray emitting isotopes of similar masses with half-lives of 10 days to 100 years. The few isotopes possible (^{85}Kr, ^{86}Rb, ^{89}Sr, ^{91}Y, and ^{90}Sr) were then analyzed for their parent activities in order to determine if any signatures were seen within the CARIBU online spectra collected at CARIBU. An alternative search was performed to include all possible fission products below mass 95, which could have passed through the mass separator by way of ionic combinations with smaller species that combine to equal a mass of 95, the results of which produced no conclusive evidence due to the lack of γ-ray peaks or incorrect ratios of multiple identifiable γ-rays. It had been concluded there were no obvious contaminants within the sample.

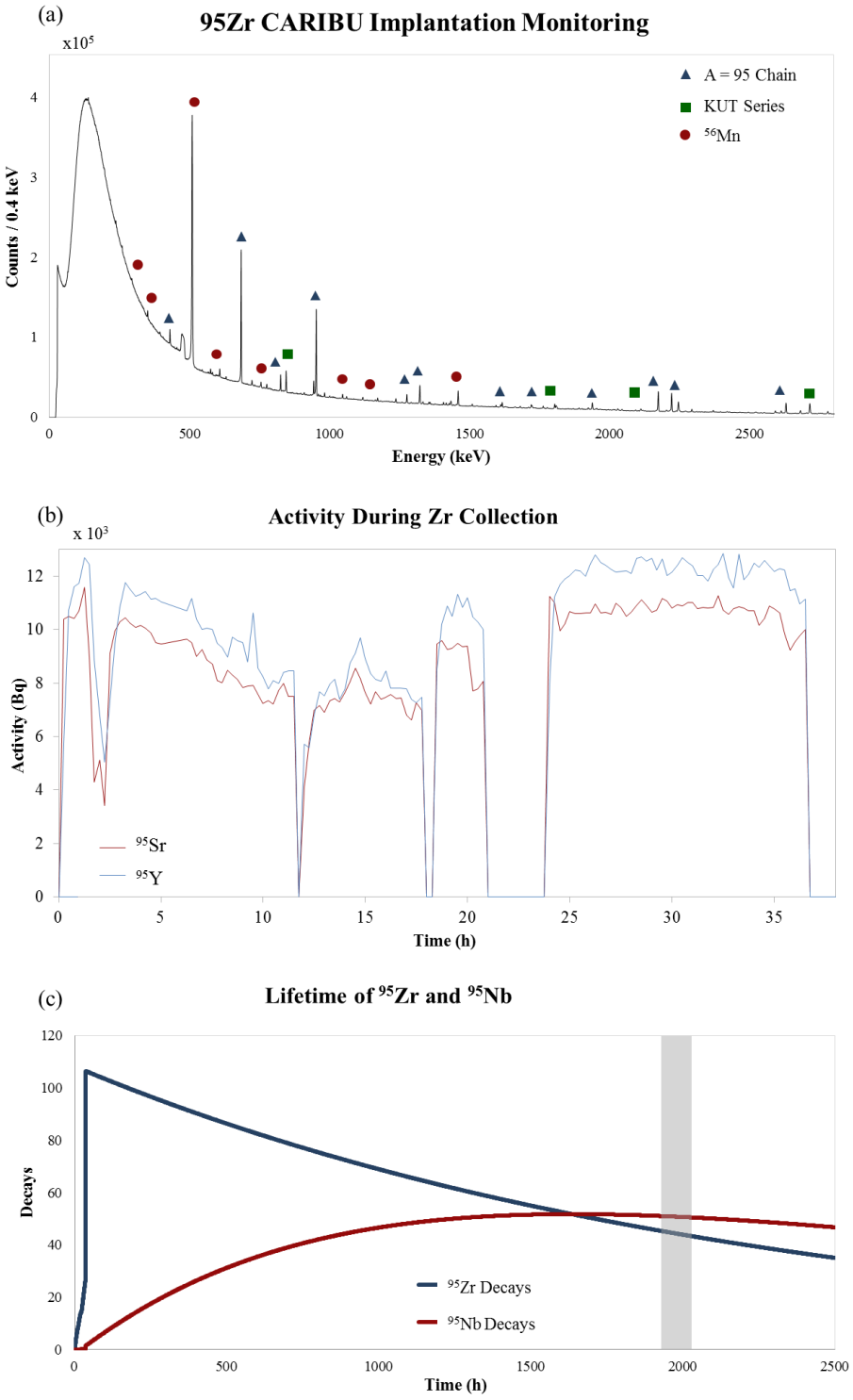

Figure 4.6: (a) γ-ray spectrum of the CARIBU beam monitoring of mass 95 isotopes. (b) Beam intensity over the length of the measurement. (c) Growth and decay of ^{95}Zr and ^{95}Nb source. The gray section indicates the duration of the measurement performed at TAMU.

Taking the peak area of the strongest ^{95}Sr and ^{95}Y peaks over each of the measured spectra, an indirect beam intensity is determined (Fig. 4.6b). The beam varied in intensity and was taken offline for tuning several times, which is clearly seen from the beam monitoring spectrum. Upon completion of implantation, the source was taken out of the beam line and left to decay for a few hours to let the more active species die away. The activity of the sample produced after 33 hours of beam was ∼220 Bq.

The ^{95}Zr source was transported to TAMU roughly 80 days after implantation. A voltage plateau was performed using a nuclear reactor-produced source (discussed in Chapter 4.2) and was set at 2575 V. The activity of the source was determined to be 93 Bq during measurement at TAMU.

All sources were removed from the room and a background measurement was performed over a period of 45 hours. Once completed, the ^{95}Zr source was loaded into the detector and positioned 152.9(1) mm from the head of the HPGe.

The CARIBU-produced ^{95}Zr measurement began on June 13, 2016. In total, the γ-ray measurement lasted 96 hours and the $\beta\gamma$ coincidence measurement lasted 71 hours. Fig. 4.6c shows the creation, decay, and measurement timeline of the first CARIBU source over its lifetime taking into account both ^{95}Zr and ^{95}Nb isotopes.

The measured γ-ray and $\beta\gamma$ coincidence spectra are shown in Fig. 4.7. The γ-ray spectrum has an overlaid background spectrum included (Fig. 4.7a). During this measurement, the detector is un-shielded in a high background area causing a large amount of background peaks to be detected in addition to the radiation present within the sample itself. The background peaks are natural sources of radiation within the room. Due to the low source strength at the time of measurement, the background peaks almost drown out the source's emitted radiation.

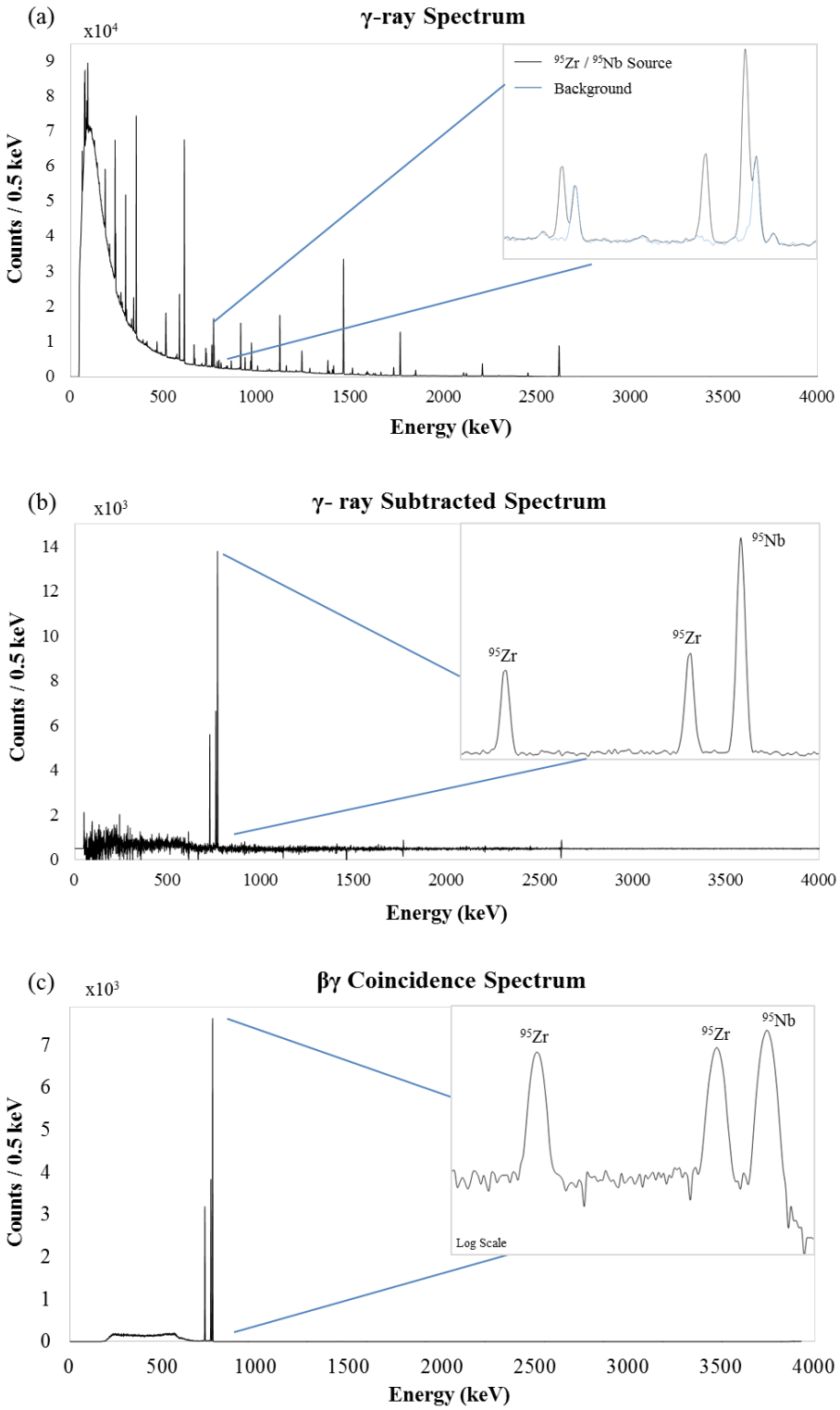

Figure 4.7: (a) γ-ray spectra of the source and background measurements overlaid, (b) background-subtracted γ-ray source spectrum, and (c) $\beta\gamma$ coincidence spectrum of a ^{95}Zr/^{95}Nb CARIBU-made source.

For this reason, a large effort is involved with subtracting the background from the source spectrum (Fig. 4.7b). The procedure most effective is as follows: focus on the area surrounding the three peaks of interest, align the closest background peaks found in both the source spectrum and the dedicated background spectrum, optimize the normalization factor calculated from the ratio of live time to real time, then subtract the altered background spectrum from the source spectrum. The remaining γ-ray spectrum is virtually free of interfering background peaks, especially in the region of interest. A live time normalization factor of 2.12 was applied to the background measurement to make it comparable to the γ-ray spectrum. If necessary, the peaks in either spectra are broadened in order to achieve agreement between FWHM of background peaks found within both measured spectra.

In contrast, the measured $\beta\gamma$ coincidence spectrum (Fig. 4.7c) produces a measurement of the source without background radiation. The spectrum is clean, with only the three expected peaks visible (two from the decay of ^{95}Zr and one from ^{95}Nb). This clean coincidence spectrum is a good indication of the lack of radioactive contaminants within the source.

Measured values for rates of the γ-ray and $\beta\gamma$ coincidence peaks of the three main transitions are shown in Table 4.6. Contributions to uncertainties associated to the measurement of the γ-rays are shown in Table 4.7. The peak rates of the source are quite low and the statistics achieved during the measurement are at the sub-percent level. However, the background subtraction of the γ-ray spectrum resulted in increased levels of uncertainty which almost doubled the total uncertainty value associated to peak rates. Other uncertainties include the difference in fits of the peaks and aligning the background to the γ-ray spectrum by way of gain shifting and normalization. Uncertainties associated to the $\beta\gamma$ coincidence peak areas are a combination of the statistics of the fit and the differences in fitting procedures of the peaks. The uncertainties achieved with the $\beta\gamma$ coincidence peak areas are much smaller as there is no interference from background.

Table 4.6: Measured peak rates for ^{95}Zr/^{95}Nb CARIBU source. The rates listed are those detected by the instruments which measured them.

γ Energy (keV)	γ-rays	$\beta\gamma$ Coincidence
724.2	0.0552(11)	0.0543(05)
756.7	0.0661(12)	0.0653(05)
765.8	0.1383(16)	0.1301(12)

Table 4.7: Uncertainty contributions associated to the γ-ray peak analysis for ^{95}Zr/^{95}Nb CARIBU source.

	724 keV	**756 keV**	**765 keV**
Radware	1.04%	0.87%	0.52%
Subtraction of Background Spectrum	1.70%	1.38%	0.81%
Different fits of peak	0.24%	0.43%	0.37%
1σ Shifts in Gain	0.36%	0.42%	0.47%
0.5% Change in Normalization	0.13%	0.27%	0.05%
Absolute Uncertainty in γ-ray Peak	**2.04%**	**1.76%**	**1.13%**

In order to calculate gas counter efficiencies of the transitions of interest, a decay correction needed to be applied to both γ-ray and coincidence measurements to account for the differences in measurement times (Eq. 2.13). This correction calculates the rates at a specific reference time where the values are comparable. The correction applied directly to the peak areas for γ-rays and $\beta\gamma$ coincidences were calculated to be 3.35×10^{-6} and 4.15×10^{-6} respectively. This correction accurately accounts for the coincidence measurement duration to be 74% to that of the γ-ray measurement duration. This correction uses the measured half-lives of ^{95}Zr and ^{95}Nb which are known very well ($t_{1/2}$ = 64.032(6) d and 34.991(6) d) and result in a negligible uncertainty contribution.

Comparing gas counter efficiencies for measured and simulated data (Table 4.8), there is good agreement. The simulations are accurately representing the measurement. A threshold is imposed on the simulations based upon measurement results, limiting the detected deposition of energy to 1.1 keV or greater.

Table 4.8: Gas counter efficiencies for the main transitions of ^{95}Zr/^{95}Nb CARIBU source for GEANT4 simulations and measured data. A threshold of 1.1 keV was applied to these simulations.

Isotope	β Energy (keV)	GEANT4	Measured
^{95}Zr	366.9	0.973	0.972(22)
^{95}Zr	399.4	0.971	0.976(19)
^{95}Nb	159.8	0.929	0.929(12)

Another key piece of information required is the total isotopic efficiencies. Calculated values of isotopic gas counter efficiencies are determined through simulations by combining the possible transitions that make up an isotope using literature β branching values. Calculations give isotopic efficiencies of 0.973(4) for ^{95}Zr, 0.931(3) for ^{95}Nb, and 0.748(1) for ^{95m}Nb. Using these isotopic efficiencies, a total gas counter efficiency for the source was determined to be 0.966(5). This value takes into account the ratios of the different isotopes within the source and assumes no contamination present.

Calculated dead times of the system are minimal, as the activity of the source during the measurement is quite low. The γ-ray dead time is determined to be 0.56% of the total time of measurement. The dead times associated to the coincidence measurement is a sum of the dead times to process a β, γ-ray, and coincidence event. This value is determined to be 0.08% of the total time of measurement. Differences between the γ-ray and coincidence dead times can be attributed to the large γ-ray background radiation that is detected throughout the γ-ray measurement, but not during the coincidence measurement. The dead time associated to the measurement of β particles in the gas counter is $4.4*10^{-3}$ %. The low dead time of the gas counter is a result of the low activity of source and the quick dissipation of the electrons moving through the gas. The avalanche electrons produced in the gas from the radiation are quickly transported through the gas to the anode wire, resulting in narrow pulse of about 10 μs (before any signal processing).

Specific isotopic contributions to the measured β particles are determined by calculating the source's growth and decay over time. The total β particle activity was determined to be 93.04(43) Bq. This value is calculated by taking the measured β rate, subtracting gas counter background, and correcting for total gas counter efficiency of the source. This activity includes all detected radiation from the source which includes only ^{95}Zr, ^{95}Nb, and ^{95m}Nb as there is no detectable contamination. The specifics of the CARIBU measurement (duration and beam intensity) and the decay of the source before and during the measurement are incorporated into the calculation. The ratio of Zr to total source activity is 45.6%, the ratio of Nb to total source activity is 54.0%, and the ratio of ^{95m}Nb isomer (including conversion electrons, β particles, and γ-rays) to total source activity is 0.5%. The majority of the radiation given off from the source can be attributed to the decay of ^{95}Nb. This is a result of the relatively long time between source production and source measurement, whereby ^{95}Zr is constantly contributing to the growth of ^{95}Nb (Fig. 4.7c).

The observed contribution of each isotope is determined by correcting the activities for gas counter efficiencies. These rates are the detected amount of radiation emitted from the source at the time of measurement. The total measured gas counter rate was 88.37(4) *cps*, of which 41.3 *cps* is ^{95}Zr, 46.7 *cps* is ^{95}Nb, and 0.36 *cps* is ^{95m}Nb. These values are used in the γ-ray branching ratio calculation.

γ-ray branching ratios, contributions, and uncertainties are listed in Table 4.9. Several important discoveries were gained by performing this initial experiment. The correction subtraction of the background to the γ-ray spectrum introduced a large level of uncertainty. This could be further reduced if the length of the background measurement is comparable to the source measurement. The source strength, while effectively achieving a result, should also be increased to reduce the uncertainty associated to peak statistics.

While performing background measurements of the gas counter, it was discovered that the Mylar windows were charging up and releasing electrons due to improper insulation[66,67].

Table 4.9: γ-ray branching ratio contributions, uncertainties, and final values for ^{95}Zr/^{95}Nb decay.

	724.2 keV	756.7 keV	765.8 keV
$R_{\beta\gamma}$	0.0543(5) cps	0.0653(5) cps	0.1301(7) cps
R_{β}	41.30(25) cps		46.70(25) cps
ϵ_{γ}	0.002977(9)	0.002884(9)	0.002860(9)
$\epsilon_{\beta_{isotope}}$ / ϵ_{β_i}	0.9986(6)	1.0011(6)	1.0000(6)
γ-ray Branching Ratio	0.4410(44)	0.5491(51)	0.9741(71)
NNDC	0.4427(22)	0.5438(22)	0.99808(7)

This can be seen by placing a β source next to the windows for a time, removing the source, and measuring the background rate in short increments. The rate of the background was found to be high then would slowly decrease over time. This Malter effect could result in unstable and un-quantifiable background rate during measurements (when a radiation source is placed inside the chamber) potentially adding false counts to the measurement that are indistinguishable from real counts. The problem was resolved by changing the windows from Mylar to Havar, which is non-magnetic, and attaching them to the detector using conductive silver epoxy.

The growth of the daughter, ^{95}Nb is extremely sensitive to the CARIBU implantation and the subsequent ratios of Zr and Nb within the source. A low value of the γ-ray branching ratio for ^{95}Nb suggests the value assigned to the number of β particles for ^{95}Nb is not accurate. The source was allowed to decay for a long period of time resulting in the majority of activity originating from the decay of ^{95}Nb. This is not an ideal case because the calculation relies on ^{95}Zr as the primary source of radiation. Time between source creation and source measurement must decrease in order for the correction of the daughter to be minimized.

The measured voltage plateau (Fig. 4.4) produced a small region of stability ($\sim$ 100 V), which suggests the gas counter is not operating at optimal efficiency. Potential changes in

temperature, pressure, applied voltage, etc. could affect the measured count rate of the source. Upon further analysis of gas counter operation, several issues were discovered which decreased the initial confidence of the system for precision measurements.

The exhaust outlet of the gas counter can be placed underwater to see the rate of gas flow. Generally, the rate is set to one bubble per second. For this measurement, it was discovered there was a leak in the system whereby no gas was visually detected from the exhaust underwater. While gas is being supplied to the counter, multiple sources of gas exhaust is undesirable as air could enter the chamber due to both internal and external environments being at atmospheric pressure. Oxygen's high electron affinity could cause smaller avalanche intensities within the gas counter causing instabilities within the system.

Another issue causing a limited plateau region was the cleanliness of the anode wires. The uniformity of the electric field produced by applying bias to the anode wires is greatly determined by the uniformity of the wire itself. If the wire is not properly cleaned or bias is applied in the presence of particulates found in the air/gas, dust and other solids could affect the uniformity of the wire resulting in discrepancies of the electric field. A good indication of the wire's cleanliness is the look of the wire both with the eye and under a microscope. To the eye, if the wire has lost its gold color and looks gray, there is good indication that particles are stuck to the wire. Under a microscope, the wire should appear as one continuous string without jagged edges or spots. Once this was discovered, both wires were replaced and cleaned before the next experiment.

4.3.2 Final Measurement of ^{95}Zr

Once corrections were made to the gas counter, an additional ^{95}Zr CARIBU-made source was produced and measured. This experiment applied all of the information gained and corrected the problems encountered with earlier measurements. The basic steps were as

before: create a source with acceptable strength using radioactive beams at the CARIBU facility, transfer the source to TAMU and measure source using precision instrumentation, compare gas counter response with GEANT4 simulations, and calculate high precision γ-ray branching ratio values for ^{95}Zr and ^{95}Nb.

The source collection occurred between December 4-11, 2017 over a period of 154 h. Measured γ-ray spectra during beam collection are summed and shown in Fig. 4.8a. Similar to the previous collection, the resulting spectrum is free from obvious contamination outside of the A=95 chain, uranium/thorium decay chains, and room background of ^{56}Mn and ^{40}K. The activity of the peaks of interest from ^{95}Zr and ^{95}Nb are not visible due to the high amount of radioactivity emitted from other mass 95 isotopes.

Isotope ^{95}Sr, with a γ-ray peak at 685.6 keV and a decay intensity of 22.6%, was taken as an indirect measurement of the CARIBU beam intensity during implantation. Fig. 4.8b visually represents the beam intensity over the length of the 154 h implantation. Upon completion of implantation, the source was taken out of the beam line and left to decay for a few hours to let the more active species die away. It was then immediately shipped to TAMU for measurement.

Before start of the measurement, a voltage plateau was determined for the gas counter using a stronger ^{147}Nd source. The resulting measurement was almost ideal. The plateau region extended over 250 V (Fig. 4.9a) with changes less than 1% over the entire range (Fig. 4.9b). Everything about this voltage plateau measurement confirms the gas counter is operating as expected and is a marked improvement over the first ^{95}Zr/^{95}Nb voltage measurement (Fig. 4.4). The operating voltage was set at 2400 V.

All sources were removed from the vicinity and a background of both the γ-rays and gas counter instruments were performed. The γ-ray background was measured over a period of

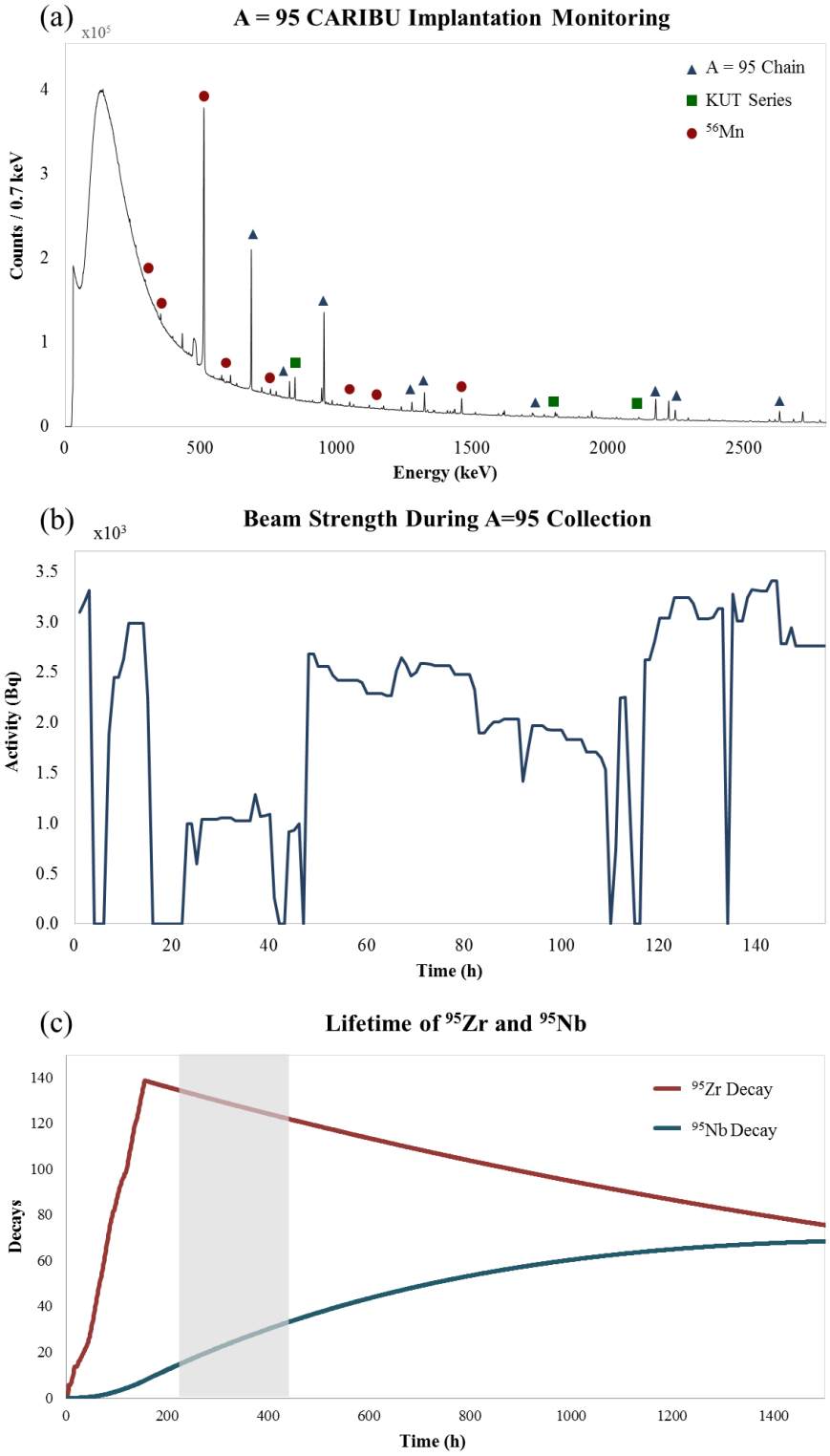

Figure 4.8: (a) γ-ray spectrum of the CARIBU beam monitoring of mass 95 isotopes. (b) Beam strength over the duration of the measurement. (c) Growth and decay of ^{95}Zr and ^{95}Nb. The gray section indicates the length of the measurement.

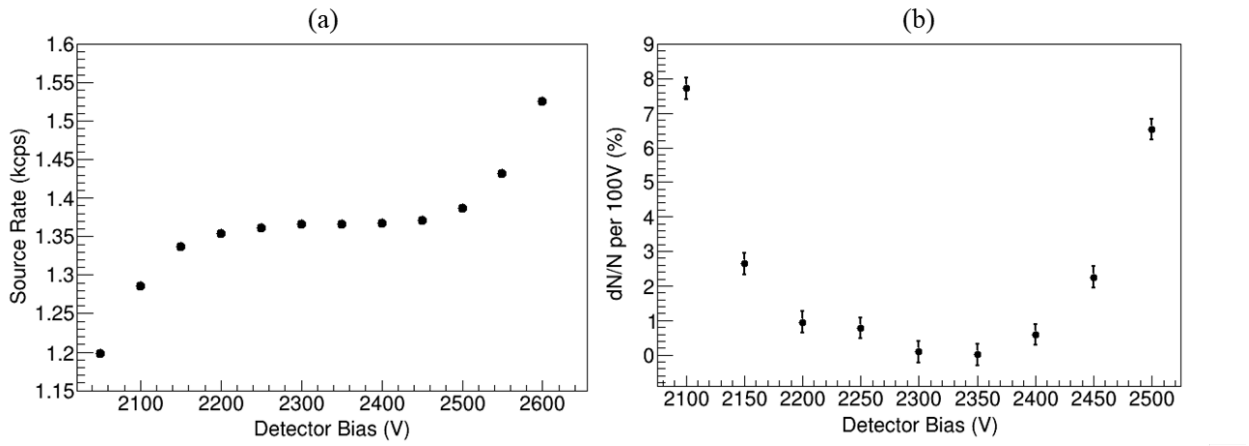

Figure 4.9: (a) A measured voltage plateau using a ^{147}Nd source and (b) the change in counts per 100 V.

9.75 days. One additional change from previous measurements was to include a shield over the HPGe detector head so as to reduce the γ-ray background interference.

This shield consisted of a thin layer of lead to reduce the γ-rays and an inner layer of copper to reduce the x-rays emitted from γ-ray interactions with the lead. The face of the HPGe detector facing the gas counter remained un-shielded so as to not attenuate any γ-rays emitted from the source inside the gas counter. Several gas counter backgrounds were measured over this period to confirm the lack of the Malter effect that was seen in previous measurements. The resulting gas counter background was determined to be 0.70(5) *cps*.

Once gas counter performance was tested for reliability, the ^{95}Zr/^{95}Nb source was loaded into the chamber. The gas counter window facing the HPGe was removed so as to accurately position the source foil 152.9(1) *mm* distance to the detector head. Once this distance was achieved, the window was replaced and the gas counter was left to expel the air introduced to the system for a period of 10 hours. The rate of exhaust of the gas counter underwater confirmed no leaks were present in the system.

Measurement of the γ-rays, β particles, and coincidence events of the ^{95}Zr/^{95}Nb source occurred over 7.5 continuous days. Fig. 4.10a shows the measured γ-ray spectrum with

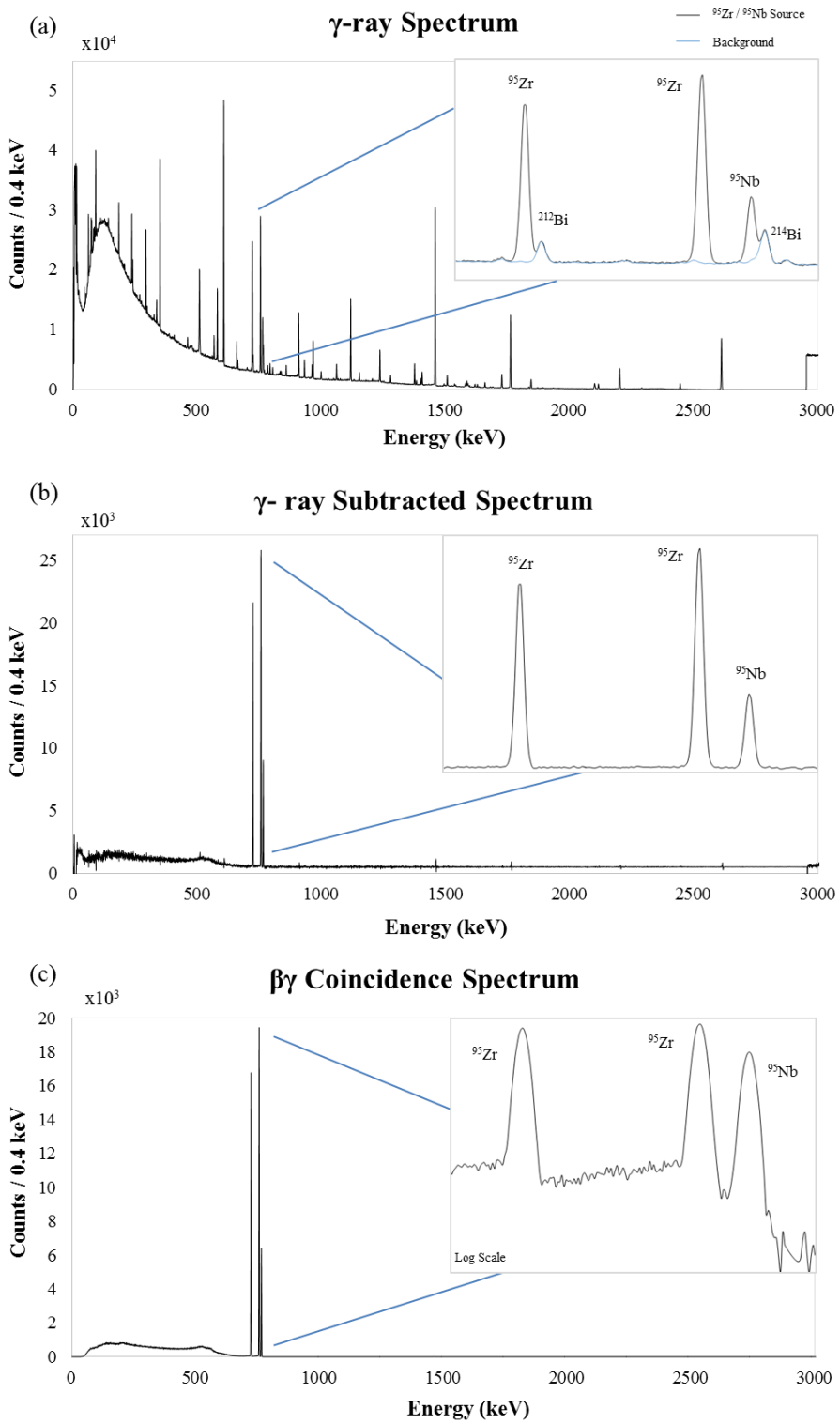

Figure 4.10: (a) γ-ray spectrum, (b) background subtracted γ-ray spectrum, and (c) measured coincidence spectrum of the CARIBU ^{95}Zr/^{95}Nb source.

Table 4.10: Peak rates for γ-ray and $\beta\gamma$ coincidence measurements of ^{95}Zr/^{95}Nb CARIBU source.

γ Energy (keV)	γ-ray	$\beta\gamma$ Coincidence
724.2	0.1678(7)	0.1636(8)
756.7	0.2033(7)	0.1967(8)
765.8	0.0696(8)	0.0644(5)

Table 4.11: Uncertainty contributions associated to the γ-ray peak analysis for ^{95}Zr/^{95}Nb CARIBU source.

	724 keV	**756 keV**	**765 keV**
Radware	0.32%	0.29%	0.49%
Subtraction of Background Spectrum	0.20%	0.17%	0.49%
Peak Fit Variation	0.12%	0.13%	0.14%
1σ Shifts in Gain	0.18%	0.02%	0.51%
0.5% Change in Normalization	0.08%	0.07%	0.70%
Absolute Uncertainty in γ-ray Peak	**0.45%**	**0.37%**	**1.12%**

the dedicated background spectrum overlaid. The three peaks of interest at 724.2, 756.7, and 765.8 keV are clearly visible in the almost noise-deafening spectrum. After aligning and normalizing (live time normalization factor of 0.768) the dedicated background with the γ-ray spectrum, the background was subtracted from the source measurement spectrum to produce a fairly clean spectrum with the ^{95}Zr and ^{95}Nb peaks of interest identifiable (Fig. 4.10b). A few small peaks can be seen within the spectrum that do not belong to ^{95}Zr or ^{95}Nb caused by a slight misalignment of the background spectrum to the source spectrum over energy ranges that are not of interest. These peaks are not contamination within the source and no further corrections were applied. The measured $\beta\gamma$ coincidence spectrum is also displayed (Fig. 4.10c) showing an incredibly clean spectrum with no obvious contamination.

Measured values for rates of the γ-ray and $\beta\gamma$ coincidence peaks of the three main transitions are shown in Table 4.10. Sample fits of both γ-ray and $\beta\gamma$ peaks are shown in Fig. 4.11.

Contributions to uncertainties associated to the measurement of the γ-rays are shown in Table 4.11. Uncertainties which make up the quoted peak area involve Radware uncertainties (statistical and fit of the background below peak), the general uncertainty associated to subtracting one spectrum from another, the variations in possible fitting techniques, small gain shifting uncertainties, and normalization uncertainties associating with scaling the background to the source spectrum. Uncertainties associated to the measurement of coincidence events are a combination of statistics and various fits of the peak.

All of the components which make up the uncertainty associated to the γ-ray measurement and analysis have been minimized, resulting in a total uncertainty of less than 1% for transitions involving ^{95}Zr and just over 1% for transitions involving ^{95}Nb. The γ-ray associated to ^{95}Nb at 765.8 keV has the highest error largely due to statistical reasons. Several days between source creation and measurement result in small amounts of ^{95}Nb being produced from the decay of ^{95}Zr ($t_{1/2}$ = 64 days). This, coupled with the relatively large interfering background peak of ^{214}Bi, results in an uncertainty greater than 1%.

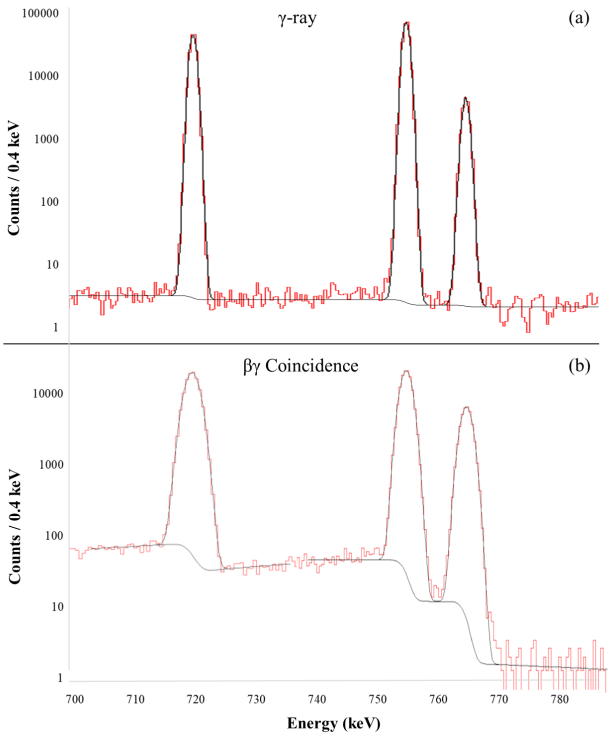

Figure 4.11: Fits of both (a) γ-ray and (b) $\beta\gamma$ coincidence peaks.

Using information gained from the measurement of $\beta\gamma$ coincidences, a TDC spectrum can be recreated (Fig. 4.12). It is triggered by the detection of a γ-ray that opens a window 2.0 μs in time. A hit occurs if the gas counter detects a particle within that time limit, populating a bin of this histogram. Collection of all hits during the measurement creates this TDC

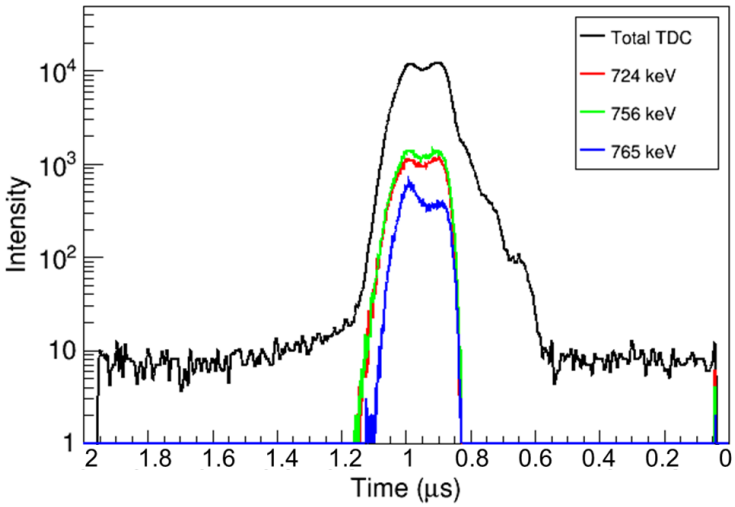

Figure 4.12: The TDC spectrum of the source and its individual contributions.

spectrum showing the correlation of γ-ray and β events in time. A total TDC and the main transitions of ^{95}Zr/^{95}Nb are shown. The signal from the gas counter has been delayed such that its arrival occurs at the center of the 2.0 μs window. There is some deviation between the total TDC and the main transitions. It is possible this arises due to the isomeric state decaying by internal conversions that are uncorrelated in time with the decay of ^{95}Zr. The difference in half-lives between the decays could result in this extra, un-centered in time, contribution to the TDC spectrum.

The deposition of energy within the gas counter was performed for measurement and simulation data (Fig. 4.13a). A β particle born with some energy will deposit a fraction of that energy within the gas counter as it interacts with the gas. Combining the various possible β transitions for ^{95}Zr, ^{95}Nb, and ^{95m}Nb from the simulation into a total energy deposition of the source allows for a direct comparison to be made with measured data. Energy calibrations can be extracted from the simulated energy deposition that can be applied to the measured energy deposition. Overlaying the two and shifting the measured spectrum to align with the simulated spectrum gives an average energy deposit of 4.1 keV. Focusing at the low energy range, the electronic threshold of the gas counter appears to be set at 1.1 keV, which agrees with the simulated electronic threshold set for determination of gas counter efficiencies.

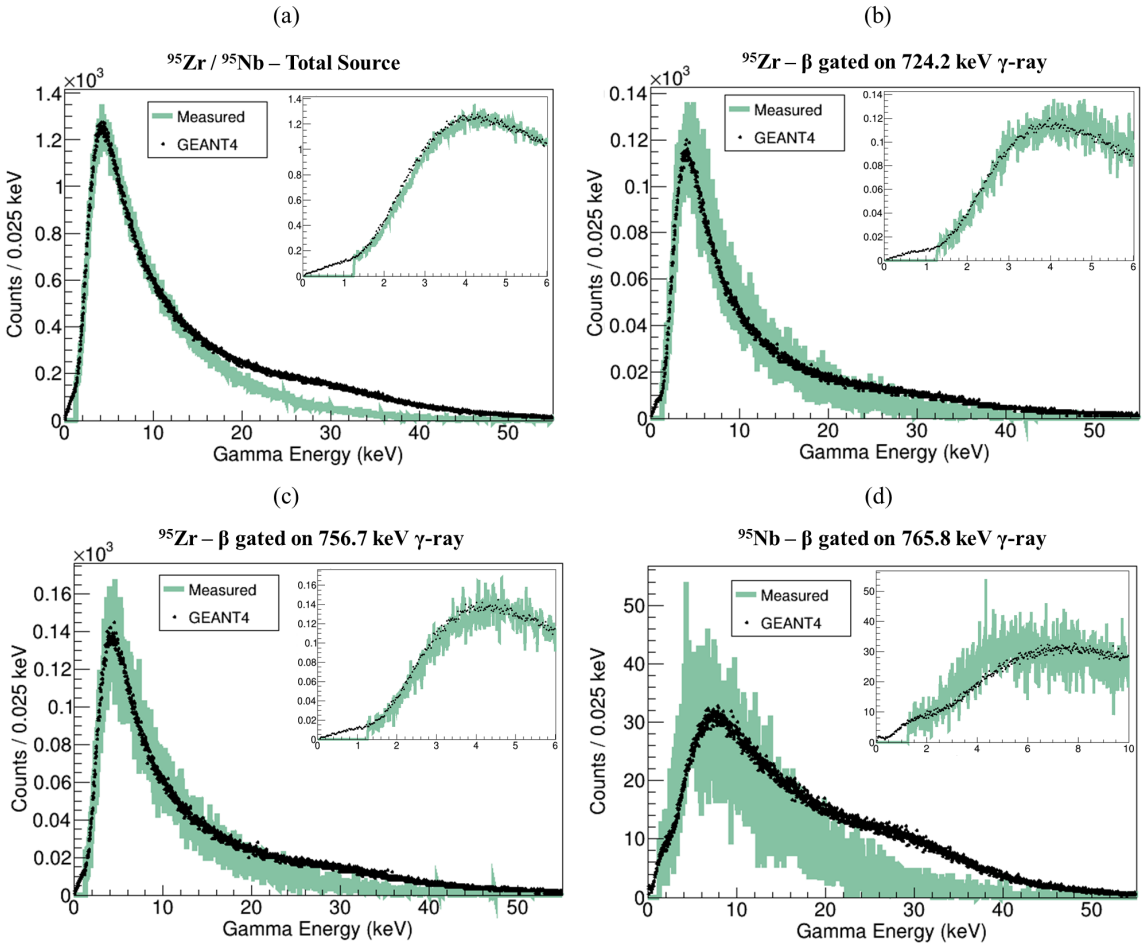

Figure 4.13: (a) A comparison of the deposition of energy spectra between measured and GEANT4 simulated data for the total ^{95}Zr/^{95}Nb source. The zoomed region shows an average deposited energy of 4.1 keV and a threshold of 1.1 keV. In addition, specific transition deposition of energy spectra are shown for β particles gated on (b) 724.2, (c) 756.7, and (d) 765.8 keV γ-rays.

Deposition of energy spectra are also compared for the three main transitions. Good agreement is seen between simulated and measured data for both ^{95}Zr transitions (Fig. 4.13b and Fig. 4.13c). The main transition that makes up ^{95}Nb decay (Fig. 4.13d) is somewhat inconsistent with simulated values, however, this is likely a result of statistical fluctuations in the measured data.

Deviations between measured and simulated data occur at the higher energies (20 - 40 keV) of the deposition energy spectrum. The most probable reason could be design differences

Table 4.12: Measured and GEANT4 simulated gas counter efficiency values for a ^{95}Zr/^{95}Nb CARIBU source.

Isotope	$E_{\beta_{max}}$ (keV)	GEANT4	Measured
^{95}Zr	399.4	0.973	0.976(5)
^{95}Zr	366.9	0.971	0.969(5)
^{95}Nb	159.8	0.929	0.927(10)

between the simulation and measurement. The simulation represents an ideal case of the measurement of β particles in the gas counter. Ideal cases are never seen in physical systems. Design differences such as the lack of anode wires and Teflon pieces securing the wires inside the physical detector could play a role at these higher energies. Imperfections in charge collection in the odd corners of the detector coupled with a nonlinear response of the electronics could also cause this discrepancy at the higher energy range.

Taking the ratio of $\beta\gamma$ coincidence to γ-ray rates, a gas counter efficiency for the transition of interest is determined. These values are shown in Table 4.12. Based upon the information gained from measurement of the deposition of energy spectrum, an electronic threshold of 1.1 keV was imposed on the simulated gas counter efficiencies. Good agreement was found between simulated and measured efficiencies, further confirming the simulations are accurately representing the gas counter response.

Calculated values of isotopic gas counter efficiencies are determined through simulated efficiencies by combining the possible transitions that make up an isotope using literature β branching values. Isotopic efficiencies are 0.972(4) for ^{95}Zr, 0.929(3) for ^{95}Nb, and 0.748(1) for ^{95m}Nb. Using these isotopic efficiencies, a total gas counter efficiency for the source was determined to be 0.963(5). This value takes into account the ratios of the different isotopes within the source and assumes no contamination present.

Dead times associated to the measurement of the source were relatively low as the activity of the source is only ∼154 Bq. Measurement of the γ-rays result in a dead time of 0.56%, with the majority of the contribution arising from measurement in the presence of high background radiation. Measurements of the gas counter result in a dead time of 0.007%. The dead times associated to the coincidence measurement is a sum of the dead times to process a β, γ-ray, and coincidence event. This value was determined to be 0.09%. These dead times have minimal effects on the measurement.

Isotopic-specific contributions to the measured β particles were determined by calculating the source's growth and decay over time (Fig. 4.8c). The total β particle activity was 154.32(4) Bq. This value was calculated by taking the measured β rate, subtracting gas counter background, and correcting for total gas counter efficiency of the source. This activity includes all detected radiation from the source which arise from the decay of ^{95}Zr, ^{95}Nb, and ^{95m}Nb. The specifics of the CARIBU measurement (duration and beam intensity) and the decay of the source before and during the measurement were incorporated into the calculation. The ratio of Zr to total source activity is 83.5%, the ratio of Nb to total source activity is 15.7%, and the ratio of ^{95m}Nb isomer (including emitted conversion electrons, β particles, and γ-rays) to total source activity is 0.6%. The majority of the radiation given off from the source can be attributed to the decay of ^{95}Zr. The short amount of time between creation and measurement does not allow ^{95}Nb to be in equilibrium with ^{95}Zr due to their comparable half-lives.

The observed contribution of each isotope is determined by correcting the activities for gas counter efficiencies. These values are the detected amount of radiation given off from the source. The total measured gas counter rate is 148.66(4) cps, of which 125.2(3) cps is ^{95}Zr, 22.6(1) cps is ^{95}Nb, and 0.899(4) cps is ^{95m}Nb. These values are used in the calculation of γ-ray branching ratios.

Table 4.13: Calculated γ-ray branching ratio values for a ^{95}Zr/^{95}Nb CARIBU source.

	724.2 keV	756.7 keV	765.8 keV
$R_{\beta\gamma}$	0.1636(8) cps	0.1967(8) cps	0.0644(5) cps
R_{β}	125.20(45) cps		22.57(8) cps
ϵ_{γ}	0.002977(9)	0.002884(9)	0.002860(9)
$\epsilon_{\beta_{total}}$ / ϵ_{β_i}	0.99862(63)	1.00109(63)	1.00002(63)
γ-ray Branching Ratio	0.4384(29)	0.5454(35)	0.9982(91)
NNDC	0.4427(22)	0.5438(22)	0.99808(7)

Calculated γ-ray branching ratios are shown in Table 4.13 along with the contributions to uncertainties (Table 4.13). The uncertainties associated to the measurement are comparable to literature values for ^{95}Zr suggesting that this method is an accurate way to reduce uncertainties to the level of $\sim$1% for fission products. These values confirm the validity of this method, as earlier issues have been resolved, and give confidence to its application of more complex fission products.

Chapter 5

Method Application - ^{144}Ce

^{144}Ce is most often used as a source of antineutrinos in the search for sterile neutrinos[68,69], a long-lived fission product in spent nuclear fuel for safeguard applications[70], and as a teaching aid for understanding nuclear principals and applications[71]. Cerium is the most common lanthanide[72] and used in processes such as glass polishing[73,74], catalytic converters[75,76], oxidation[77,78], and glass manufacturing[79].

5.1 ^{144}Ce/^{144}Pr Overview

The fission product ^{144}Ce decays by emission of low energy β particles and γ-rays to the ground state of ^{144}Pr, which then decays to stable ^{144}Nd. Its relatively long half-life ($t_{1/2}$ = 284.91(5) d) allows for multiple measurements of the same source. Mass 144 is readily produced from the fission of ^{252}Cf and can be created using radioactive beams from the CARIBU facility at ANL. The proper reaction to produce ^{144}Ce using a nuclear reactor is not feasible, so all sources of ^{144}Ce were created using the CARIBU radioactive beam.

5.1.1 CARIBU Source Production

^{144}Ce is a major fission product in spontaneous fission of ^{252}Cf. Its mass chain can be delivered as a low energy beam to the implantation site at a rate of 1.6×10^7 ions/sec[3]. Main fission products of mass 144 are ^{144}Ba, ^{144}La, and ^{144}Cs with direct absolute yields of 3.37%, 1.86%, and 0.55% respectfully (Fig. 5.1). The half-lives of these isotopes are less than a minute, which essentially results in a pure ^{144}Ce/^{144}Pr source in under an hour. The radioactive beam of mass 144 delivers +2 charged ions at a speed of 72 keV. Using ^{144}Ba, the implanting ions would penetrate 20.5% into the carbon foil[54].

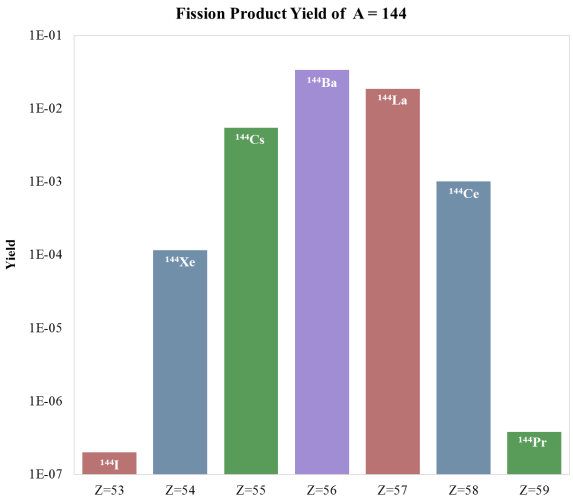

Figure 5.1: Mass 144 fission product yield from ^{252}Cf[8].

Similar to other sources produced at CARIBU for these experiments, an HPGe is set up to measure γ-rays deposited on the foil which is positioned toward the center of the cross that is attached to the beam line. An energy and efficiency calibration is performed using ^{152}Eu, ^{60}Co, and ^{137}Cs calibration sources at this specific geometry. During implantation, measurements are made to monitor the implantation and beam intensity. Several γ-rays were monitored throughout the collection: 103.9 keV (23.3%) from the decay of ^{144}Ba, and 397.4 keV (94.3%) and 844.8 keV (22.3%) from the decay of ^{144}La. Using measured peak areas, the activity of the isotope can be determined by Eq. 4.1. This specific formula is a first approximation of isotopic activity as there are two competing sources of isotopic growth: direct fission product yield and decaying parent isotopes. Absolute activity is not the main concern during beam monitoring.

Table 5.1: Literature branching ratios for γ-rays and β particles[10].

	γ Energy (keV)	γ Branching Ratio	$E_{\beta_{max}}$ Energy (keV)	β Branching Ratio
^{144}Ce	80.120	0.0136(6)	238.6	0.039(20)
^{144}Ce	133.515	0.1109(19)	185.2	0.196(40)
^{144}Ce			318.7	0.7650(50)
^{144}Pr	696.510	0.01342(14)	2301.0	0.0104(2)
^{144}Pr	2185.662	0.00694(13)	811.8	0.0105(4)
^{144}Pr			2997.5	0.9790(40)

5.1.2 Decay Scheme

Unlike the simplicity of the ^{95}Zr decay scheme (Fig. 4.2), ^{144}Ce has several complex transitions that make recreation using simulations challenging. The Q value of ^{144}Ce is 318.7 keV, which is relatively low when compared to the test source (^{95}Zr, Q = ~1.0 MeV). Table 5.1 lists literature branching ratios for γ-rays and β particles. ^{144}Ce has three main β transitions which populate two excited states levels, 133.5 and 80.1 keV, and the ground state of ^{144}Pr. The ground state is populated the majority of the time, releasing a β particle and no γ-ray. There are two other excited states (100 and 59 keV), which get populated from feeding of higher energy states.

The lowest excited state at 59 keV is an isomeric state, which is populated ~0.257% from feeding. This isomeric state decays by internal conversion 99.93% populating the ground state ^{144}Pr and by β decay 0.07% populating the ground state of ^{144}Nd.

The complexity in the decay scheme arises due to the highly converted nature of many of the decays. In place of a detectable γ-ray, a conversion electron (CE) and x-ray are emitted. There are a total of 19 CEs which make up 12.23% of the emitted decays compared to 13.05% emission of γ-rays. Table 5.2 lists the γ-ray energies and their intensities emitted by ^{144}Ce along with the intensities of those CEs which are emitted instead of the listed γ-ray.

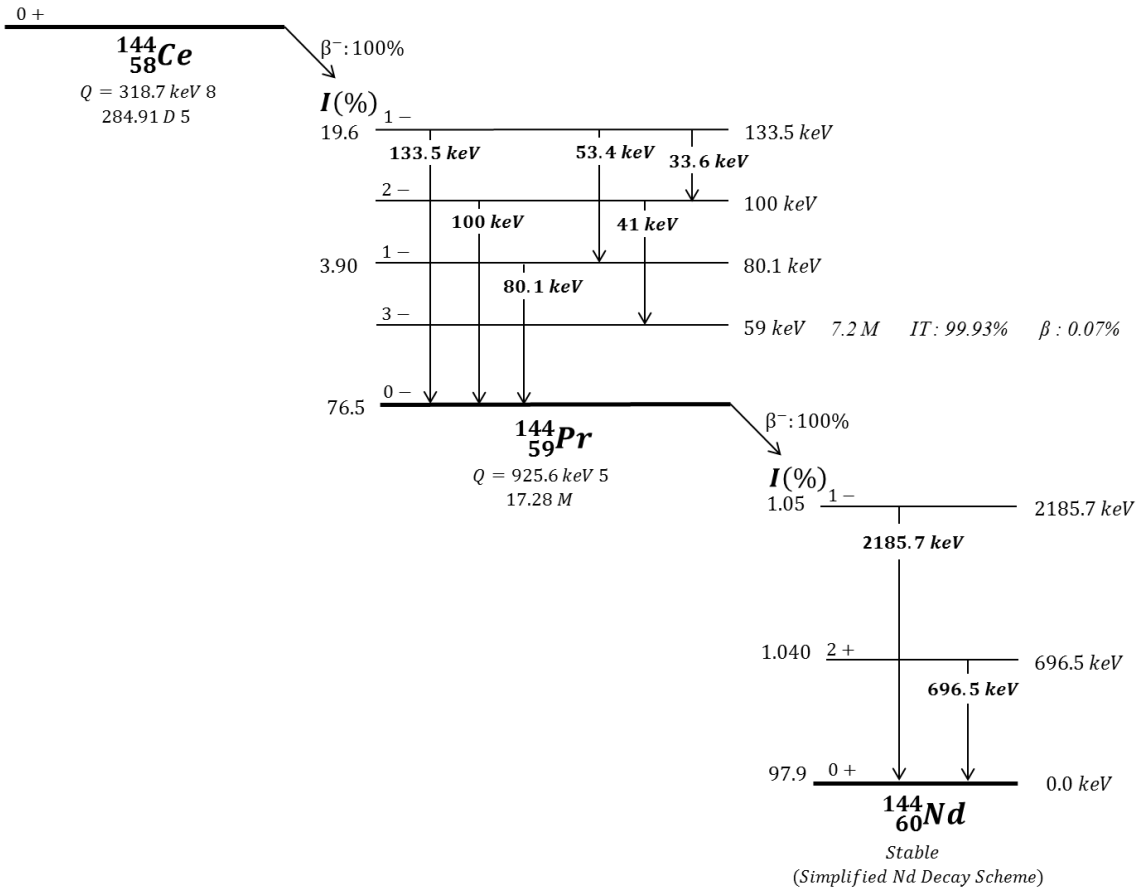

Figure 5.2: A simplified decay scheme exhibiting the major transitions of ^{144}Ce decaying to ^{144}Pr decaying to ^{144}Nd. The decay to the isomeric state of ^{144m}Pr is also seen at the 59 keV energy level.

The decay of ^{144}Ce results in growth of the daughter, ^{144}Pr. In contrast to ^{144}Ce, ^{144}Pr has a high Q value of 2997.5 keV and a short half-life of 17.28 m. As a result, the ratio of ^{144}Ce/^{144}Pr quickly reaches secular equilibrium. Fig. 5.2 shows a simplified decay scheme with all of the decays of ^{144}Ce represented and the main transitions of ^{144}Pr displayed. The vast majority of the ^{144}Pr β decays directly populate the ground state releasing no measurable γ-ray. This simplified decay scheme of ^{144}Pr recreates 99.99% of β decays.

Table 5.2: Literature branching ratios for γ-rays and CE emissions associated to the decay of ^{144}Ce[9]. This isotope is highly converted.

γ Energy (keV)	% γ Branching Ratio	% CE Emission
133.515	11.09	6.378
99.961	0.040	0.084
80.120	1.36	3.374
53.395	0.100	0.806
40.98	0.257	0.678
33.568	0.200	0.907

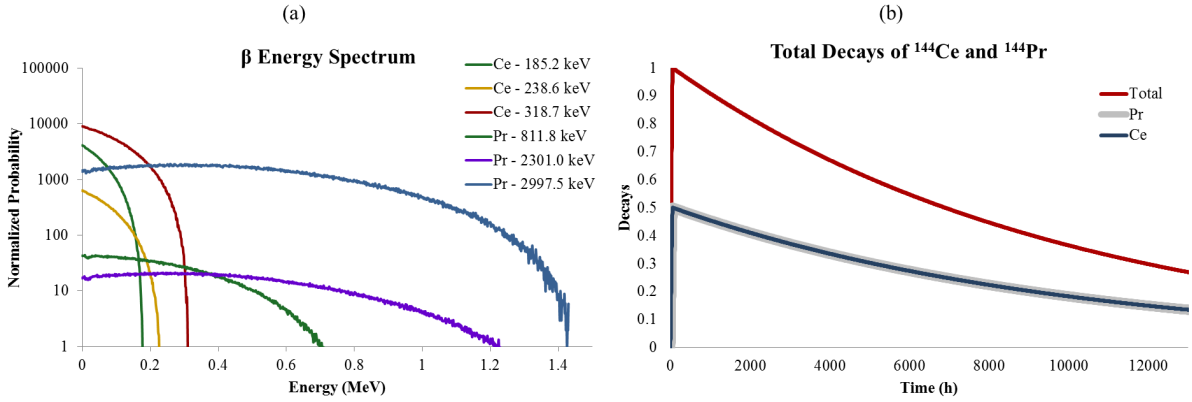

Figure 5.3: (a) Major β transitions for ^{144}Ce and ^{144}Pr and (b) decay of the source over time.

5.1.3 Simulated β Energy Spectrum

As a result of the different end-point energies between ^{144}Ce and ^{144}Pr, the β energy spectra for the different possible transitions are widely different. Fig. 5.3a displays the main three transitions for both ^{144}Ce and ^{144}Pr. Due to the low end-point energy of ^{144}Ce, the β energy spectra are skewed toward the low energy with a large percentage of β particles being born at low energies. Conversely, β particles of ^{144}Pr have their energy spectra skewed toward higher energies with the majority of β particles being born at energies greater than 100 keV.

5.1.4 Half-Lives of ^{144}Ce/^{144}Pr

Both isotopes come into secular equilibrium quickly as a result of the long half-life of the parent ($t_{1/2} = 284.91(5)\ d$) and the short half-life of the daughter ($t_{1/2} = 17.28(5)\ m$). The isomeric state, ^{144m}Pr also has a short half-life ($t_{1/2} = 7.2(3)\ m$). This has several benefits: relative stability of source strength over the duration of the measurement, constant ratio of parent to daughter, and ability of multiple measurements to be made with the same source. In a manner of a few hours, the total activity of the source is reached and its decay time is dependent on the parent half-life.

5.1.5 Simulated Gas Counter Efficiency

Simulations were performed taking into account the decay scheme shown in Fig. 5.2. A total of six β transitions were simulated and combined in ways so as to accurately represent specific transitions. The gas counter response greatly depends on the energy of the emitted β particle and CE, which varies according to the specific transition. During the $\beta\gamma$ coincidence measurement, a β particle (or CE) and a γ-ray need to be detected. It follows that in order to detect a specific γ-ray in coincidence with an event in the gas counter, both the efficiency of the γ-ray and β particle (or a CE) are important. Most often, the emission of a specific γ-ray is made up of multiple transitions, all of which need to be accounted for when determining the probability of an event occurring in the gas counter.

Unlike ^{95}Zr, the ^{144}Ce simulation is only of the CARIBU-type source. It is difficult to irradiate a cerium source with neutrons in an effective manner to produce the ^{144}Ce isotope in large quantities. The CARIBU source has radioactive ions deposited 20.5% into a carbon foil of thickness 40 $\mu g/cm^2$. The radiation is dispersed over a diameter of 7.0 mm with a radiation thickness of 1.0 fm.

Transitions involving ^{144}Pr are straightforward. A simplified version of ^{144}Pr decay scheme is used which represents 99.99(4)% of the total decay scheme found in literature[9]. There are two transitions that populate excited states and decay to the ground state, which is also directly populated by β decay. Three β particles are simulated with energies: 811.8, 2301.0, and 2997.5 keV. The resulting gas counter efficiency for the ground state is calculated by determining the number of events detected in the gas counter divided by the number of β particles simulated. For the two excited state transitions, the β efficiency is calculated similarly with additional simulations to account for those γ-rays which may have deposited energy in the gas counter. These excited state transitions are seen in a $\beta\gamma$ coincidence spectrum. However, for the majority of the decays that populate the ground state directly, a measurable gas counter efficiency can not achieved due to lack of emitted γ-rays. As a result, the simulated results for ^{144}Pr are relied upon heavily.

The decay of ^{144m}Pr occurs on a timescale of 7.2 m and is treated as a separate decay. The majority of ^{144m}Pr decays by internal conversion and release CEs. These CEs will deposit energy in the β detector with high probability as a result of their discrete energy. The average energy of a CE emitted in the decay of ^{144m}Pr is 50 keV.

For the decay of ^{144}Ce, simulations are heavily relied upon due to direct β decay population of the ground state with a probability of 76.5(5)%[9]. These decays do not emit a γ-ray and a gas counter efficiency for this transition using measurements is not possible. Rather, simulations of the gas counter response are heavily relied upon for this transition. In addition, while the decay scheme of ^{144}Ce looks relatively simple, it is made complicated due to a large percentage of decays feeding excited states. The 80.1 keV energy level is populated by both direct β decay and feeding from higher excited states resulting in a gas counter efficiency that is made up of a combination of different β energies. The decays from these excited states can also occur through emission of a CE or a γ-ray, which further increase the number of possible transitions.

Table 5.3: List of possible decay pathways to ground state (GS) or isomeric state of ^{144}Ce including emitted β particles, CEs, and γ-rays.

#	Transition (keV)	Energy Level (keV)	Transition (keV)	Energy Level (keV)	Transition (keV)	Energy Level (keV)	Absolute Probability
1	β - 185.2	133.5	γ - 133.5	GS			11.158%
2			CE - 132.004	GS			0.159%
3			CE - 126.6802	GS			0.763%
4			CE -91.5244	GS			5.495%
5	β - 185.2	133.5	γ - 53.4	80.1	γ - 80.1	GS	0.029%
6					CE - 78.609	GS	0.002%
7					CE - 73.285	GS	0.009%
8					CE - 38.129	GS	0.061%
9	β - 185.2	133.5	CE - 51.884	80.1	γ - 80.1	GS	0.006%
10					CE - 78.609	GS	0.000%
11					CE - 73.285	GS	0.002%
12					CE - 38.129	GS	0.012%
13	β - 185.2	133.5	CE - 46.560	80.1	γ - 80.1	GS	0.028%
14					CE - 78.609	GS	0.002%
15					CE - 73.285	GS	0.008%
16					CE - 38.129	GS	0.059%
17	β - 185.2	133.5	CE - 11.404	80.1	γ - 80.1	GS	0.199%
18					CE - 78.609	GS	0.012%
19					CE - 73.285	GS	0.059%
20					CE - 38.129	GS	0.424%
21	β - 185.2	133.5	γ - 33.6	100	γ - 100	GS	0.008%
22					CE - 98.450	GS	0.001%
23					CE - 93.126	GS	0.006%
24					CE - 57.970	GS	0.009%
25	β - 185.2	133.5	γ - 33.6	100	γ - 41	59 Iso	0.049%
26					CE - 39.47	59 Iso	0.022%
27					CE - 34.15	59 Iso	0.106%

Continued on next page

Table 5.3 – continued from previous page

#	Transition (keV)	Energy Level (keV)	Transition (keV)	Energy Level (keV)	Transition (keV)	Energy Level (keV)	Absolute Probability
28	β - 185.2		CE - 32.057	100	γ - 100	GS	0.006%
29					CE - 98.450	GS	0.001%
30					CE - 93.126	GS	0.004%
31					CE - 57.970	GS	0.007%
32	β - 185.2	133.5	CE - 32.057	100	γ - 41	59 Iso	0.038%
33					CE - 39.47	59 Iso	0.018%
34					CE - 34.15	59 Iso	0.083%
35	β - 185.2	133.5	CE - 26.733	100	γ - 100	GS	0.028%
36					CE - 98.450	GS	0.005%
37					CE - 93.126	GS	0.021%
38					CE - 57.970	GS	0.035%
39	β - 185.2	133.5	CE - 26.733	100	γ - 41	59 Iso	0.183%
40					CE - 39.47	59 Iso	0.084%
41					CE - 34.15	59 Iso	0.399%
42	β - 238.6	80.1	γ - 80.1	GS			1.120%
43			CE - 78.609	GS			0.069%
44			CE - 73.285	GS			0.330%
45			CE - 38.129	GS			2.381%
46	β - 318.7	GS					76.500%

For example, the transition which results in emission of a 133.5 keV γ-ray occurs by emission of a β particle with an end-point energy of 185.2 keV that populates the 133.5 keV energy level, which then decays by emission of the 133.5 keV γ-ray. This is a simple transition whereby the gas counter efficiency is made up of a combination of the energy deposited by the β particle and γ-ray. In contrast, the possible transitions which result in emission of an 80.1 keV are many. Emission of a β particle with end-point energy of 185.2 keV populates the 133.5 keV energy level that can then decay to the 80.1 keV energy level by emission of a γ-ray or a CE and then emit the 80.1 keV γ-ray. Another possibility is the direct population

of the 80.1 keV energy level by a β particle with an end-point energy of 238.6 keV and then emission of the 80.1 keV γ-ray. Each possible transition has a different β efficiency, with the total efficiency of the gas counter gated on an 80.1 keV γ-ray being made up of a combination of the different transition probabilities.

Table 5.3 lists all of the 46 transitions which make up the ^{144}Ce decay scheme. Due to the fact that a large number of transitions have a small absolute probability of occurring, only those transitions which have a probability >0.1% are recreated. These transitions reproduce 99.22% of the total decay scheme.

In order to compare simulations with measured data, the exact combination of simulated gas counter efficiencies is determined by the measurement. The measurement of gas counter efficiencies is dependent on the ability to detect a specific γ-ray which is in coincidence with a β particle (or CE). As such, the β particle transition must be accompanied by a γ-ray. Those transitions which do not emit a γ-ray are used to determine the total isotope gas counter efficiency, but do not play a role in determining efficiencies for a $\beta\gamma$ coincidence event. For example, to calculate the gas counter efficiency of an event which is gated on an 80.1 keV γ-ray, those transitions which specifically emit an 80.1 keV γ-ray are combined in a way that is proportional to their probability of emission. In Table 5.3, these would be transitions numbered: 5, 9, 13, 17, and 42. These specific decays which emit an 80.1 keV γ-ray make up 1.38% of the total decays of ^{144}Ce.

The simulated results for the total gas counter efficiencies and the specific transitions for ^{144}Ce, ^{144}Pr, and ^{144m}Pr are shown in Table 5.4. Due to measurement limitations of the physical system, the results are shown with various thresholds imposed, the exact value of which is determined during the measurement. The efficiencies of the majority of transitions in ^{144}Ce are greatly influenced by self-attenuation effects between the emitted β particles and the sample foil. This effect causes an immediate reduction of the gas counter efficiency at the low threshold and slight changes in efficiencies at higher thresholds. Conversely, due

Table 5.4: Simulated results for gas counter efficiency of a 0.2 μm CARIBU-produced ^{144}Ce source.

Gas Counter Efficiency for ^{144}Ce				
	>0.5 keV	>1.0 keV	>1.5 keV	>2.0 keV
Total Gas Counter Efficiency for ^{144}Ce	0.9614	0.9588	0.9547	0.9481
β Gated on 133.5 keV γ-ray	0.9426	0.9399	0.9351	0.9290
β Gated on 80.1 keV γ-ray	0.9635	0.9611	0.9271	0.9223
β Decay to Ground State	0.9694	0.9665	0.9619	0.9544
Gas Counter Efficiency for ^{144}Pr				
	>0.5 keV	>1.0 keV	>1.5 keV	>2.0 keV
Total Gas Counter Efficiency for ^{144}Pr	0.9961	0.9826	0.9128	0.7814
β Gated on 696.5 keV γ-ray	0.9934	0.9827	0.9300	0.8261
β Gated on 2185.7 keV γ-ray	0.9896	0.9843	0.9664	0.9214
β Decay to Ground State	0.9896	0.9835	0.9130	0.7804
Gas Counter Efficiency for ^{144m}Pr				
	>0.5 keV	>1.0 keV	>1.5 keV	>2.0 keV
Total Gas Counter Efficiency for ^{144m}Pr	0.9997	0.9991	0.9993	0.9989

to the higher overall energies of β particles associated with ^{144}Pr, the gas counter efficiencies are greatly affected by increasing thresholds and less with self-attenuation of the sample foil. For those transitions that are highly converted or decay through isomeric transition (^{144m}Pr), gas counter efficiencies are high regardless of threshold due to the discrete energies of the CE.

5.2 ^{144}Ce CARIBU-Produced Source Measurements

For ^{144}Ce, one source of ^{144}Ce was produced at CARIBU and two measurements of the source were made. However, contamination was present within the source in the form of ^{103}Ru ($t_{1/2}$ = 39.2 d). Due to the relatively long half-live of the ^{144}Ce ($t_{1/2}$ = 284.9 d), it was decided to negate the first measurement in place of a measurement of the source with no activity present ($\sim$1 year later).

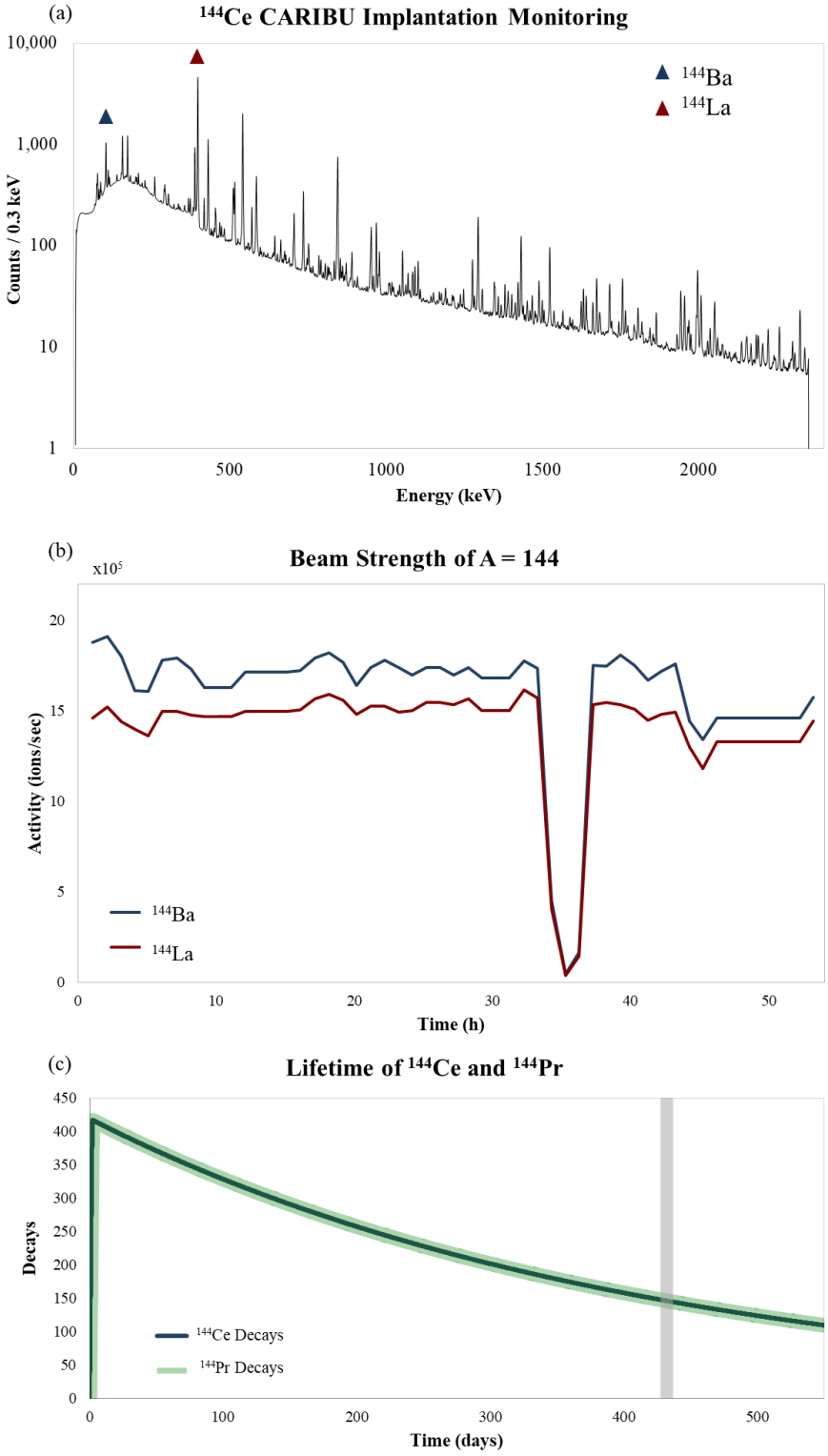

Figure 5.4: (a) γ-ray spectrum of the CARIBU beam monitoring of mass 144 isotopes. (b) Beam strength over the length of the measurement. (c) Growth and decay of ^{144}Ce and ^{144}Pr. The gray section indicates the length of the measurement.

From ^{252}Cf spontaneous fission, the majority of mass 144 ions are made up of ^{144}Cs, ^{144}Ba, and ^{144}La. The longest half-life of the three is ^{144}La ($t_{1/2}$ = 40.8 s). After about an hour, all A=144 ions will be attributed to ^{144}Ce and its daughter. Beam implantation of A=144 occurred over a period of 52 h starting September 16, 2016.

Looking at the CARIBU spectra summed over the length of the implantation (Fig. 5.4a), many peaks are detected. All of the major peaks present within the spectrum have been identified to an isotope along the mass 144 chain. ^{144}Ba, ^{144}La, and ^{144}Cs give off many detectable peaks with high activity due to their relatively short half-lives. The most intense peaks given off from ^{144}Ba and ^{144}La are identified. From this measurement, it is difficult to draw conclusions about potential contamination present within this source.

The most intense peak of ^{144}Ba (103.9 keV) and ^{144}La (397.4 keV) were monitored to determine the intensity of the beam over time (Fig. 5.4b). A relatively stable beam was achieved for this collection with one dip in beam intensity when the system was taken offline to fill the cooling systems. At the end of collection, a source of 840 Bq was created.

Once collection terminated, the source was removed from the beam and left to decay for a few hours so that the majority of these short-lived isotopes could decay. Due to the wildly different half-lives of ^{144}Ce ($t_{1/2}$ = 285 d) and ^{144}Pr ($t_{1/2}$ = 17.3 m), secular equilibrium is achieved quickly such that the activity emitted from the source is equally split between parent and daughter (Fig. 5.4c). The growth during CARIBU implantation can be seen in the beginning hours of the lifetime of the source and subsequent decay over time. The gray section is the period of time when the final measurement took place.

5.2.1 Initial Measurement of ^{144}Ce

The source was transported to TAMU for the initial measurement using the full method to reduce γ-ray branching ratios about 50 days after implantation. However, contamination within the ^{144}Ce/^{144}Pr source was discovered in the form of ^{103}Ru ($t_{1/2} = 34.2\ d$). A measurement of the $\beta\gamma$ coincidences of the source is shown in Fig. 5.5. The low energy peaks can be attributed to the decay of ^{144}Ce and the highest energy peaks associated to ^{144}Pr. In the center at 497 keV, a ^{103}Ru peak is clearly visible. This contamination requires corrections to the data which would increase the uncertainties associated to the γ-ray branching ratios.

In addition to the corrections necessary to the analyze the source, a stable voltage plateau for this measurement was not achieved. A plateau region was identified (Fig. 5.6a), but it was no more that 2% stable in the region (Fig. 5.6b), which is a signal that the detector has some operating issues that had not been identified. Also during this measurement, the detector's windows were not properly grounded resulting in a Malter effect which increased the background rate of the gas counter. This effect was not detected throughout this mea-

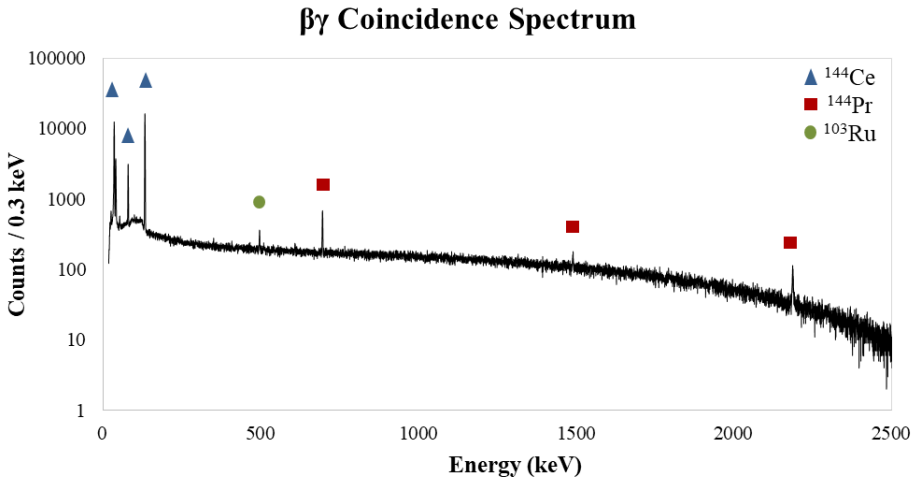

Figure 5.5: First measurement of $\beta\gamma$ coincidences of ^{144}Ce source showing the presence of ^{103}Ru contamination.

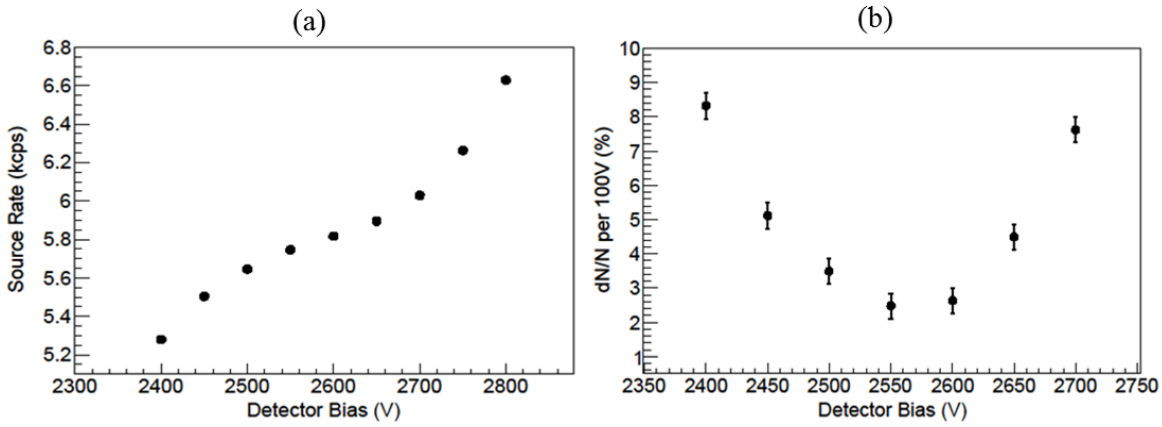

Figure 5.6: (a) Voltage plateau and (b) change in counts per 100 V measured during the first ^{144}Ce source experiment.

surement until a later time. For these reasons, it was decided that this measurement would not be used in the calculations of γ-ray branching ratios for ^{144}Ce.

5.2.2 Final Measurement of ^{144}Ce

The final source measurement occurred 470 d from source production at CARIBU. This amount of time was sufficient to allow for full decay of ^{103}Ru contaminant present within the source at the original time of creation.

Before start of the measurement, a voltage plateau was determined for the gas counter using a stronger ^{147}Nd source. The resulting measurement was almost ideal. The plateau region extended over 250 V (Fig. 4.9a) with changes less than 1% over the entire range (Fig. 4.9b). Everything about this measurement confirms the gas counter is operating without issue and was a marked improvement over the first voltage plateau performed during the first source measurement (Fig. 5.6). The operating voltage was set at 2400 V.

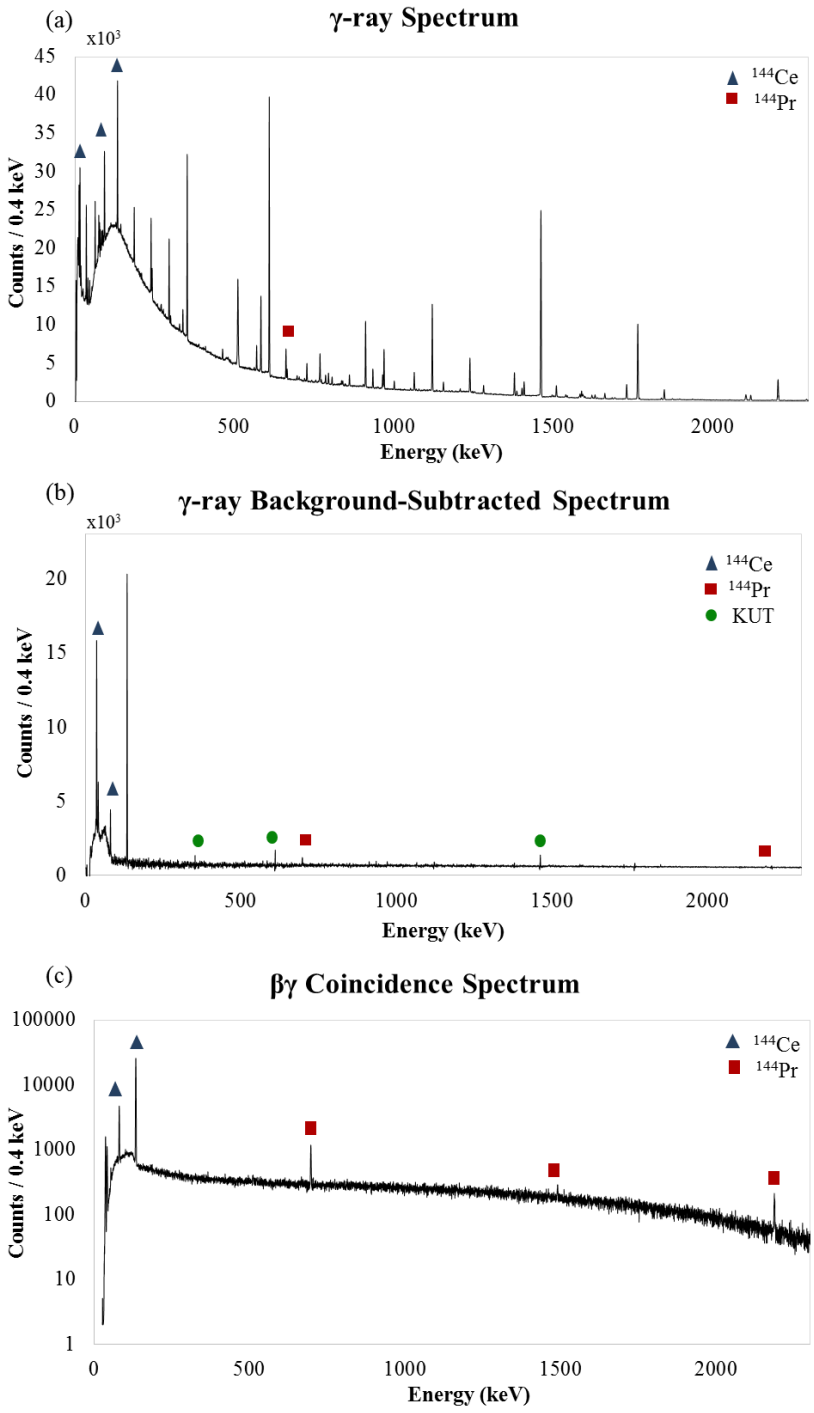

Figure 5.7: (a) γ-ray spectrum, (b) background subtracted γ-ray spectrum, and (c) measured coincidence spectrum of the CARIBU ^{144}Ce/^{144}Pr source after over a year of decay. Each spectrum shows the lack of contamination present within the source.

All sources were removed from the vicinity and a background of both the γ-rays and gas counter detectors was performed. The γ-ray background was performed over a period of 9.75 d. A shield was placed over the HPGe detector head so as to reduce the γ-ray background interference. The head of the HPGe detector facing the gas counter remained un-shielded so as to not attenuate any γ-rays emitted from the source. Several gas counter backgrounds were measured over this period to confirm the lack of the Malter effect that was seen in previous measurements. The resulting gas counter background was determined to be 0.70(5) cps. This consistently low gas counter background is a good indication the gas counter is free of loose radioactive contamination.

The ^{144}Ce source was placed inside the gas counter and the distance between the source and HPGe detector head was measured at 152.9(1) mm. Measurements of the γ-rays, β

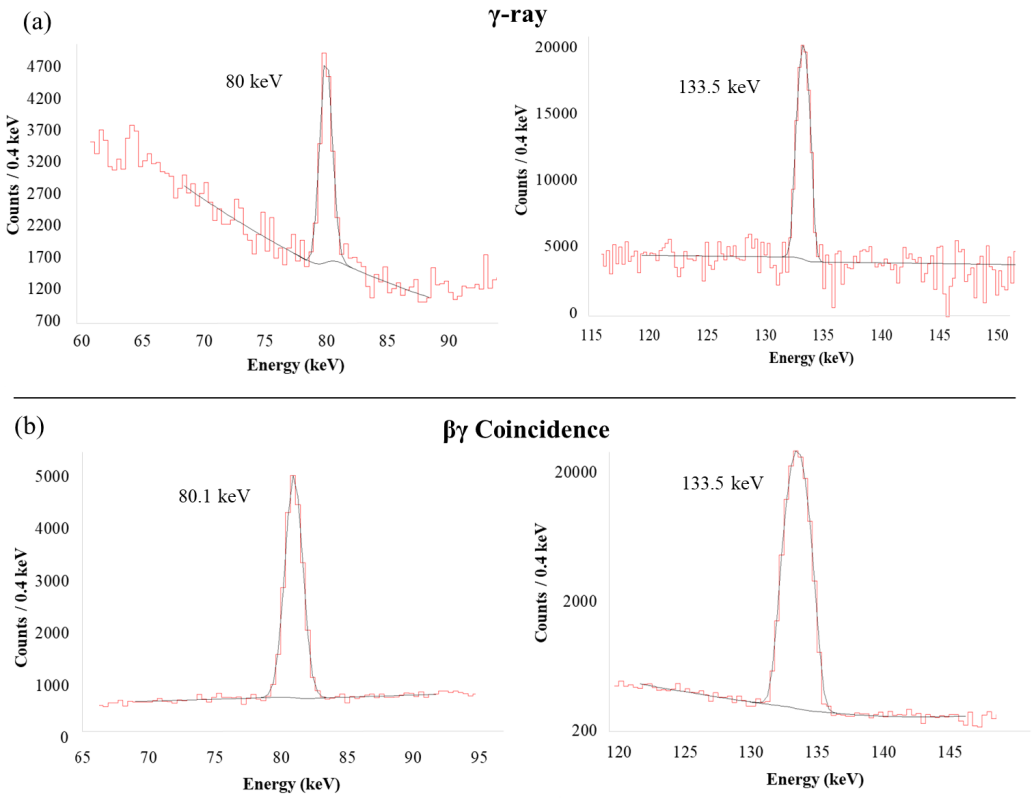

Figure 5.8: (a) γ-ray and (b) $\beta\gamma$ coincidence peak fits of 80.1 and 133.5 keV peaks.

particles, and $\beta\gamma$ coincidence events were performed on January 1-8, 2018 over a period of 6.5 days with a source activity of 263 Bq. Looking at the γ-ray spectrum (Fig. 5.7a), the main ^{144}Ce peaks are visible over the background peaks, but the ^{144}Pr are almost drowned out. Literature γ-ray branching ratios are small for the main ^{144}Pr peaks (696.5 keV at 1.342(14)% and 2185.7 keV at 0.694(13)%[10]) which explains the relative peak sizes between ^{144}Ce and ^{144}Pr regardless of the comparable activities between the two isotopes.

Subtracting the dedicated background spectrum from the source γ-ray spectrum, a new γ-ray spectrum is calculated (Fig. 5.7b) which prominently displays the ^{144}Ce peaks free from interference. Several other peaks are present within the spectrum in the form of isotopes belonging to ^{40}K or daughters of the uranium-thorium decay series. These peaks were not able to be fully subtracted due to differences in the FWHM between the source and background spectra. The majority of background peaks have been suppressed in the γ-ray background-subtracted spectrum.

γ-rays in coincidence with β particles are shown in Fig. 5.7c. Only those peaks belonging to ^{144}Ce and ^{144}Pr are identifiable. Decay calculations of ^{103}Ru over the span of 470 d confirm the lack of any measurable contamination within the source during this measurement.

Peak rates for γ and $\beta\gamma$ coincidences are shown in Table 5.5. Rates for both isotopes are relatively low due to the small probability of a decay emitting a γ-ray. Sample peak fits for γ-ray and $\beta\gamma$ coincidence are shown for the 80.1 and 133.5 keV transitions (Fig. 5.8). The breakdown of uncertainty contributions is shown in Table 5.6. The peaks belonging to ^{144}Ce (80.1 and 133.5 keV) are in the low energy region of the spectrum which has a high, non-linear background. As a result, the method by which the background is handled result in high uncertainties. The values associated to the fit of ^{144}Pr peaks (697 and 2185 keV) have high uncertainties as a result of low peak rates. The peaks are relatively small causing a lot of variation in the fit and the method by which the background is handled.

Table 5.5: Measured peak rates for γ-ray and $\beta\gamma$ coincidence measurements of ^{144}Ce/^{144}Pr CARIBU source.

γ Energy (keV)	γ-ray	$\beta\gamma$ Coincidence
80.1	0.0196(9)	0.0189(2)
133.5	0.1304(18)	0.1241(5)
696	0.0053(6)	0.0052(1)
2185	0.0011(2)	0.0011(1)

Table 5.6: Uncertainty contributions associated to the γ-ray peak analysis for ^{144}Ce/^{144}Pr CARIBU source.

	80.1 keV	**133.5 keV**	**697 keV**	**2185 keV**
Radware	1.27%	0.41%	6.31%	11.95%
Subtraction of Background Spectrum	3.59%	0.59%	5.47%	8.20%
Peak Fit Variations	1.92%	0.85%	1.07%	13.12%
1σ Shifts in Gain	0.21%	0.72%	7.85%	4.12%
0.5% Change in Normalization	1.70%	0.46%	2.45%	6.22%
Absolute Uncertainty in γ-ray Peak	**4.59%**	**1.40%**	**11.77%**	**20.93%**

The TDC spectrum generated from the $\beta\gamma$ coincidence measurement analysis is shown in Fig. 5.9. This TDC spectrum illustrates the timing of a gas counter event relative to a γ-ray event. The γ-ray event triggers a gate of 2.0 μs in length. If a coincidence event occurs within that time window, it will add a count to the histogram at the specific time it was detected relative to the start of the gate (the trigger of the γ-ray event). Those transitions that are highly converted (80.1 and 133.5 keV) show a spread in the timing range which suggests the emission of a CE occurs on a slightly different time scale then that of a pure β emission. Conversely, those decays that are not converted (696 and 2185 keV) show a narrow range of time to detect a β particle.

Measured and simulated deposition of energy spectra within the gas counter can be compared. The resulting overlaid spectrum (Fig. 5.10a) shows the measured and simulated data

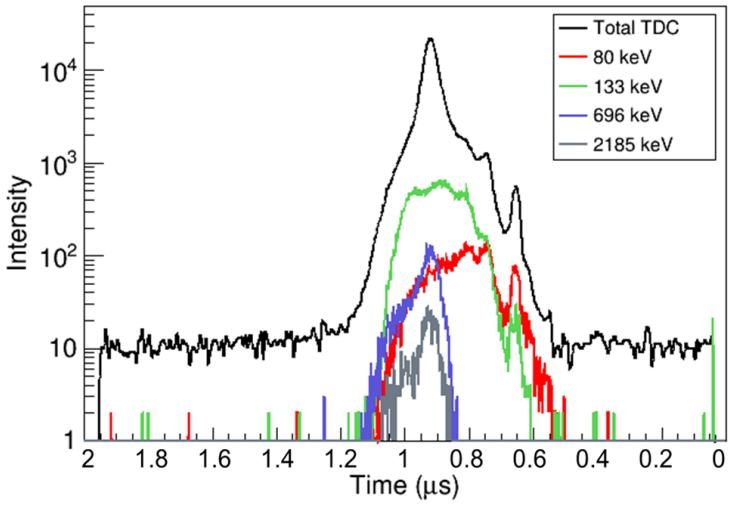

Figure 5.9: The TDC spectrum generated from $\beta\gamma$ coincidence measurement of ^{144}Ce.

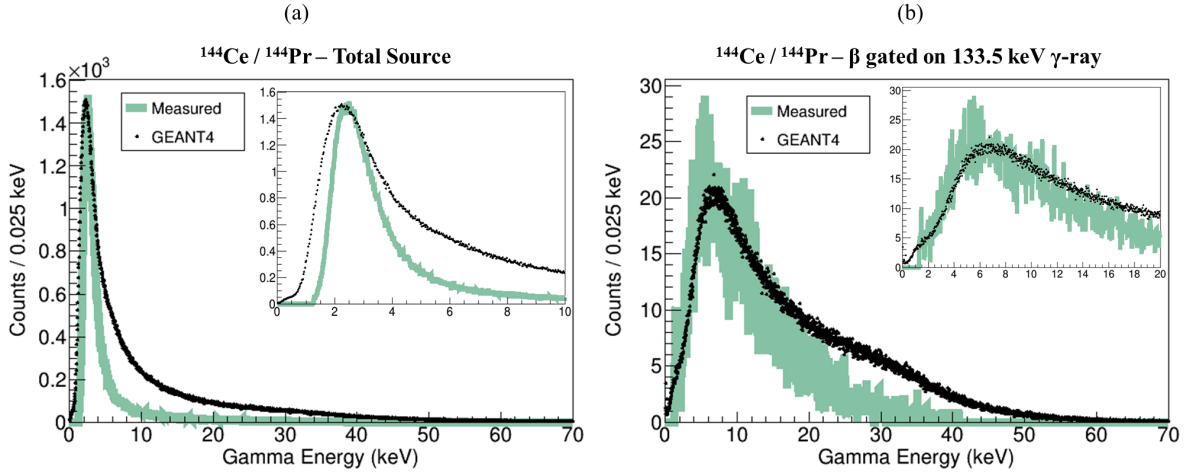

Figure 5.10: (a) A comparison of the deposition of energy spectra between measured and GEANT4 simulated data. The zoomed region shows an average deposited energy of 2.7 keV and a threshold of 1.1 keV. (b) A transition-specific deposition of energy spectrum is shown for β particles gated on 133.5 keV γ-ray.

are not in good agreement. The discrepancy is a result of true coincidence summing effects by the daughter ^{144}Pr ($E_{\beta_{max}}$ = ~3 MeV). A β particle emitted by the decay of the daughter deposits some energy in the gas counter, exits the system, and deposits some energy in the HPGe, effectively resulting in a $\beta\beta$ coincidence with itself. These β particles have high energy and are traveling at relativistic speeds, successfully depositing energies within the time window of a 2 μs coincidence event. These β particles emitted by the daughter deposit

minimal energy within the gas counter as a result of their short travel length from foil to gas counter window and high β energy.

A similar discrepancy between measured and simulated data at energies of 20 – 40 keV is seen for ^{144}Ce, which is also present in the ^{95}Zr energy deposition spectrum. This discrepancy is most likely the result of the simulation being an ideal measurement of the source whereas the experimental data is not. Imperfections in charge collection in the odd corners of the detector coupled with a nonlinear response of the electronics could result in this discrepancy at the higher energy range. Using these spectra, an average energy of the deposition of a particle within the gas counter is determined to be 2.7 keV and an electronic threshold is determined to be 1.1 keV.

Taking the ratio of $\beta\gamma$ coincidence to γ-ray rates, a gas counter efficiency for a transition of interest can be determined. These values are shown in Table 5.7. Based upon information from the measurement of the deposition of energy spectrum, an electronic threshold of 1.1 keV was imposed on the simulated gas counter efficiencies. Good agreement was found between simulated and measured efficiencies suggesting the simulation is accurately representing the measurement. Uncertainties in gas counter efficiencies for ^{144}Pr are large as a result of the statistical uncertainty of the peaks.

Table 5.7: Measured and GEANT4 simulated gas counter efficiency values for a ^{144}Ce/^{144}Pr CARIBU source.

Isotope	β Energy (keV)	GEANT4	Measured
^{144}Ce	238.7	0.961	0.960(48)
^{144}Ce	185.2	0.939	0.947(15)
^{144}Pr	2301	0.977	0.982(98)
^{144}Pr	811.8	0.982	0.989(210)

Calculated values of isotopic gas counter efficiencies are determined through combinations of simulated transition efficiencies by combining the possible transitions that make up an isotope using literature β branching values. Calculations result in isotopic efficiencies of 0.958(2) for ^{144}Ce and 0.975(3) for ^{144}Pr. A total source gas counter efficiency was calculated to be 0.966(4). The β particles being emitted from the decay of ^{144}Ce have relatively low $E_{\beta_{max}}$ values, however, the emission of a CE in those decays which populate an excited state result in relatively high efficiencies for the ^{144}Ce isotope. For ^{144}Pr, the combination of a large percentage of β decays ($E_{\beta_{max}}$=2997.5 keV) directly populating the ground state and a low electronic threshold of detection produce a high gas counter efficiency.

Dead times associated to the measurement are minimal as the source activity is relatively low. Measurements of the γ-rays result in a dead time of 0.45%, with the majority of the contribution arising from performing the measurement in a high background radiation location. Measurements of the gas counter result in a dead time of 0.006%. The dead times associated to the coincidence measurement are a sum of the dead times to process a β, γ-ray, and coincidence event. This value was determined to be 0.09%. These dead times have minimal effects on the measurement.

Isotopic-specific contributions to the measured β particles were determined by calculating the source's growth and decay over time (Fig. 5.4c). The total β singles activity during the measurement was 266.073(3) Bq. This value was calculated by taking the measured β rate, subtracting gas counter background (0.70(5) cps), and correcting for total gas counter efficiency of the source. This activity includes all detected radiation from the source which includes those contributions from ^{144}Ce, ^{144}Pr, and ^{144m}Pr as there is no detectable contamination.

The specifics of the CARIBU measurement (duration and beam intensity) and the decay of the source before and during the measurement were incorporated into the calculation. The ratio of Ce to total source activity is 49.51%, the ratio of Pr to total source activity is

Table 5.8: Calculated γ-ray branching ratio values including the contributions and uncertainties associated to the measurement for a ^{144}Ce/^{144}Pr CARIBU source.

	80.1 keV	133.5 keV	696 keV	2185 keV
$R_{\beta\gamma}$	0.0189(2) cps	0.1241(5) cps	0.0052(1) cps	0.0011(1) cps
R_{β}	127.287(17) cps		129.496(17) cps	
ϵ_{γ}	0.00985(3)	0.00894(3)	0.003050(9)	0.001343(7)
$\epsilon_{\beta_{total}}$ / ϵ_{β_i}	0.9975(30)	1.0203(31)	0.9975(30)	0.9921(30)
γ-ray Branching Ratio	0.0151(2)	0.1112(7)	0.01323(36)	0.00635(39)
NNDC	0.0136(6)	0.1109(19)	0.01342(14)	0.00964(13)

49.94%, and the ratio of ^{144m}Pr isomer (including β, CEs, and γ) to total source activity is 0.13%. Half-life of the daughter isotope ($t_{1/2}$ = 17.3 m) compared to the parent ($t_{1/2}$ = 284.9 d) is much smaller resulting in almost equal contributions to activity of the source as the two are in equilibrium. The small difference is due to the decay of the isomer ^{144m}Pr ($t_{1/2}$ = 7.2 m) which populates the daughter and adds an extra source of feeding to ^{144}Pr.

The observed contribution of each isotope is determined by correcting the activities for gas counter efficiencies. These values are the detected amount of radiation emitted from the source. The total measured source rate was 257.12(3) *cps*, of which 127.3(2) *cps* was ^{144}Ce, 129.50(2) *cps* was ^{144}Pr, and 0.3411(1) *cps* was ^{144m}Pr. These values for isotopic contribution of the source are used in the γ-ray branching ratio calculation.

Calculated γ-ray branching ratios are shown in along with the contributions to uncertainties Table 5.8. In both ^{144}Ce decays, the γ-ray branching ratio uncertainties were reduced compared with literature values. Those transitions of the daughter, ^{144}Pr, were not reduced as these transitions were not the focus of this experiment. Longer measurement of the source could produce enough statistics to make these calculations comparable or better to literature values.

Chapter 6

Method Application - ^{147}Nd

As a high yield fission product, ^{147}Nd has many uses: absolute fission yield determinations[80,81], energy and efficiency calibration standards[82,83], fuel burnup indicators[84], and many geological studies[85,86]. Natural neodymium has applications as magnets[87,88], glass coloring[89,90], and lasers[91,92].

6.1 ^{147}Nd/^{147}Pm Overview

^{147}Nd is readily remaining after a fission event as a result of its 10.98(1) *d* half-life and is easily characterized by detection of a 531 keV γ-ray. The intensity of this γ-ray is in question as literature databases, ENDF/B-VII.1[1,93] and Laboratoire National Henri Becquerel (LNHB) Table de Radionucléides[94], differ by over 5%. This 531 keV γ-ray intensity is known with an 8% uncertainty, which gives measurements of fission yields based upon γ-ray spectroscopy of this isotope an 8% uncertainty. This uncertainty is currently limiting some of the conclusions that can be drawn about environments where fission chain reactions occur.

Most ^{147}Nd decays occur by emission of a β particle to an excited state of ^{147}Pm. The majority of these decays are highly converted, producing conversion electrons (CE) in large quantities in place of γ-rays. The Q value for this reaction is 896 keV, with the average $E_{\beta_{max}}$ of ~805 keV[9]. Several studies have attempted to determine the decay scheme with high accuracy[95,96,97,98,99,100,101].

6.1.1 CARIBU Source Production

^{147}Nd is a major fission product of the spontaneous fission of ^{252}Cf and its mass chain can be produced at a rate of 1×10^7 $ions/_{sec}$[3]. Isotopes which make up the majority of the radioactive beam include ^{147}Ba, ^{147}La, ^{147}Ce, and ^{147}Pr with yields of 0.24%, 1.94%, 1.91%, and 0.18% respectively (Fig. 6.1)[1]. Each of these isotopes decay with half-lives of a few minutes, leaving only ^{147}Nd and ^{147}Pm remaining as sources of decay within the source after a few hours. The radioactive beam of mass 147 delivers +2 charged ions at a speed of 72 keV. Using these specifications, an ion of ^{147}La would penetrate 20.4% into a carbon foil[54].

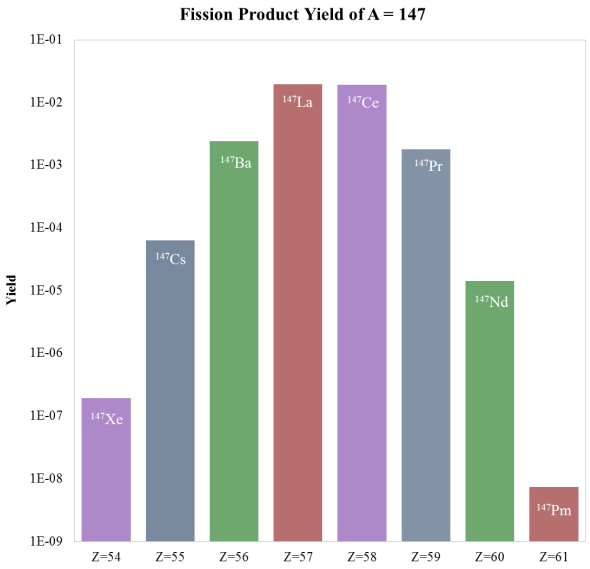

Figure 6.1: Mass 147 fission product yield from ^{252}Cf[8].

Similar to other sources produced at CARIBU for these experiments, an HPGe is set up to measure γ-rays deposited on the foil, which is positioned toward the center of the cross that is attached to the beam line. An energy and efficiency calibration is performed using ^{152}Eu, ^{60}Co, and ^{137}Cs calibration sources at this specific geometry. Several γ-rays were monitored

throughout the collection: 117.7 keV (17.6(19)%) from the decay of ^{147}La, and 580.0 keV (5.5(5)%), and 701.1 keV (2.5(2)%) from the decay of ^{147}Ce[9]. Using measured peak areas, the activity of the isotope can be determined by Eq. 4.1. This specific formula is a first approximation of isotopic activities as there are two competing sources of isotopic growth: direct fission product yield and decaying parent isotopes. Absolute activity of the sample is not the main concern during beam monitoring, rather the relative intensity of the beam is of greatest importance.

6.1.2 Decay Scheme

Of the isotopes measured using this method, ^{147}Nd is the most challenging due to a combination of a large amount of transitions, feeding from higher excited states, and high probability of the excited state transitions being converted. Shown in Fig. 6.2 is a simplified decay scheme showing only those transitions that are detected during the measurements and have a probability of over 0.019%[9]. Nine additional transitions were not detected due to the low probability of γ-ray emission.

The half-life of ^{147}Nd is a relatively short 10.98(1) *d*. The specific transitions of the β particles and γ-rays visible in the measurement are listed in Table 6.1. The lowest energy β particle has an end-point energy of 210.1 keV. In this simplified decay scheme, there are eight β transitions which populate excited energy levels of ^{147}Pm. Seven de-excitations to ground state occur by releasing a γ-ray equal to that of the energy level. Other γ-ray transitions occur: six that decay to the 91.1 keV energy level, two that decay to the 410.5 keV energy level, and one decays to the 489.3 keV energy level. These nine transitions feed into other energy levels and effectively increasing the total number of transitions from these states.

In addition to γ-ray transitions, Table 6.2 shows those transitions that are converted and release a CE instead of the listed γ-ray. The 91.1 keV excited state transition is highly

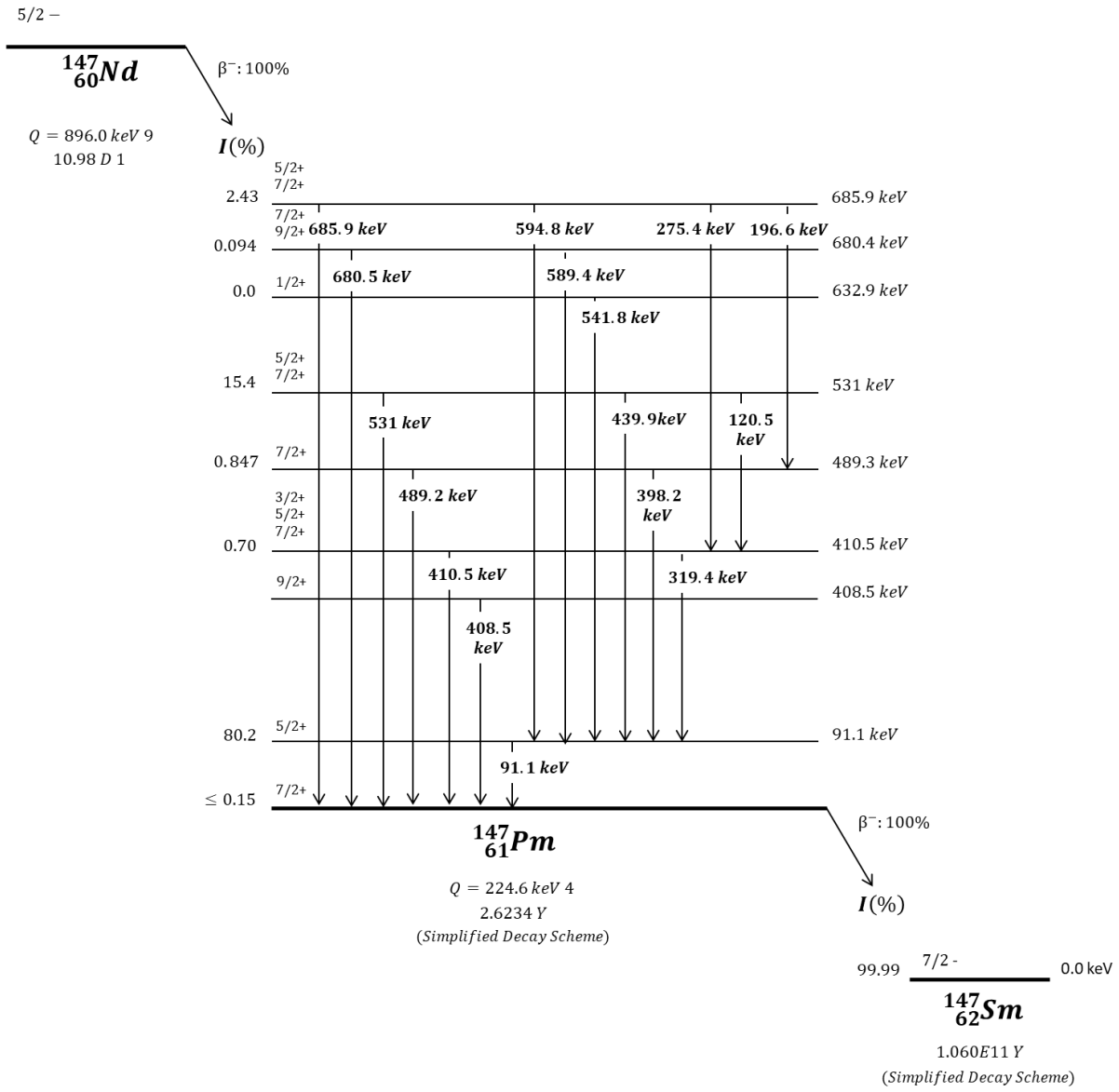

Figure 6.2: A simplified decay scheme exhibiting the major transitions of ^{147}Nd decaying to ^{147}Pm decaying to ^{147}Sm.

converted, with ∼57% of all decays emitting a conversion electron and 28.1% of the decays emitting a 91.1 keV γ-ray. The β decay of ^{147}Nd populates the 91.1 keV energy level 80.2% and feeding from higher energy levels populates the 91.1 keV energy level an additional ∼4.8%. From the 91.1 keV energy level, there are four conversion electrons of various energies that are emitted.

Table 6.1: Literature branching ratios for γ-rays and β particles from the decay of ^{147}Nd[9].

$E_{\beta_{max}}$ Energy (keV)	β Branching Ratio	γ Energy (keV)	γ Branching Ratio
210.1	0.0243(5)	685.9	0.00886(18)
		594.8	0.00283(6)
		275.374	0.00910(19)
		196.64	0.00190(4)
215.6	0.00094(4)	680.52	0.000294(14)
		589.35	0.00039(3)
		271.87	0.000132(10)
247	0.0016(16)	240.5	0.00043(3)
263.1	0(5)	541.83	0.00019(3)
		117.98	0.000160(14)
365	0.154(3)	531.016	0.134(3)
		439.895	0.0128(3)
		120.48	0.00376(9)
406.7	0.00847(19)	489.24	0.00155(3)
		398.155	0.00912(19)
485.5	0.0070(3)	410.48	0.00150(3)
		319.411	0.0213(4)
804.9	0.802(24)	91.105	0.281(7)
896	0.0008(8)	GS	
No Direct β		541.83	0.00019(3)

6.1.3 Simulated β Energy Spectrum

Three major β transitions for ^{147}Nd are shown in the β energy spectrum in Fig. 6.3a that make up ~98.0% of the β transitions. Each of these transitions have different end-point energies resulting in spectra that have quite different shapes. The most intense transition, with an $E_{\beta_{max}}$ of ~805 keV, has the majority of β particles born at higher energies relative to the smallest $E_{\beta_{max}}$ of 210 keV has the majority of β particles born with low energies.

Table 6.2: γ-ray and conversion electron emissions from excited states associated to the decay of ^{147}Nd[9]. This isotope is highly converted.

Energy Level (keV)	γ-ray Emission (%)	CE Emission (%)
531	15.06	0.34
410.5	2.28	0.11
91.1	28.1	57.043

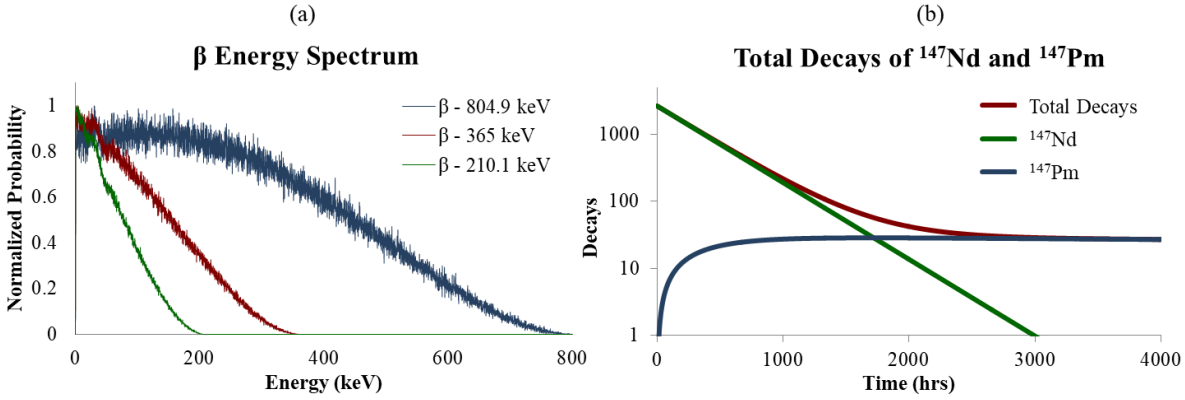

Figure 6.3: (a) Major β transitions for ^{147}Nd and (b) decay of the source over time.

6.1.4 Half-lives of ^{147}Nd/^{147}Pm

Unlike the parent-daughter combinations of the other two sets of isotopes, the relatively short half-life of ^{147}Nd and long half-live of ^{147}Pm result in no achievable equilibrium. The ratios of ^{147}Nd/^{147}Pm are constantly changing until only ^{147}Pm remains. This is rather important because the decay of ^{147}Pm produces no measurable γ-ray due to the majority of decays (99.99%) populating the ground state of ^{147}Sm directly. Identifying the amount of daughter that has grown in during the decay of ^{147}Nd is rather difficult and must rely on theoretical calculations. The granddaughter, ^{147}Sm, is also radioactive and decays by emission of an α particle. However, the half-life associated to this decay is incredibly long ($t_{1/2} = 1.060 \times 10^{11}$ y) and is essentially considered stable over the course of this measurment.

The total decay combination of a ^{147}Nd/^{147}Pm source is shown in Fig. 6.3b. Initially, the total source decay is a result of the more active ^{147}Nd decay. Once the majority of ^{147}Nd has

decayed, the longer-lived daughter is the main source of activity. The daughter decays at a much slower rate due to its long half-life. The measurement of ^{147}Nd occurs shortly after source creation in order to reduce the correction that has to be made to the growth of the daughter.

6.1.5 Simulated Gas Counter Efficiency

Experimental determination of gas counter efficiencies rely on ratios of $\beta\gamma$ coincidence and γ-ray measurements producing transition-specific gas counter efficiencies. Simulated results can calculate both transitions-specific and isotopic gas counter efficiencies that can then be compared to confirm the experimental measurement. Previous efforts concerning measurements of ^{95}Zr (Chapter 4) have already confirmed the validity of the simulation and its reliability for accurate representations of the gas counter.

The CARIBU source simulated in GEANT4 consists of a carbon foil of thickness 40(4) $\mu g/cm^2$ with radiation of 7.0 mm diameter implanted 41.2 nm into one side. The simulation assumes a radiation implantation thickness of 1.0 fm. A total of 8 β transitions were simulated out of the 9 listed in literature[9]. The β decay to the excited state level of 632 keV has almost zero probability according to literature data and is therefore ignored for the purpose of the simulation.

Most of the transitions are first forbidden transitions. A test was performed to see the effect of shape factors and its impact of detection β particles. The resulting effect of the β efficiencies for the main transition of 805 keV was impacted by $\sim$0.1% and assumed negligible within the parameters of the simulation uncertainties. No further shaping factor was applied to the simulations and all transitions were assumed to be allowed.

Similar to the ^{144}Ce decays scheme, ^{147}Nd is complex and comprised of many different pathways to ground state. Using the simplified decay scheme (Fig. 6.2), a total of 82 transitions that emit β particles, CEs, and γ-rays are possible (Table 6.3). A large number of excited states feed the 91.1 keV energy level, which has 5 possible de-excitations (91.1 keV γ-ray or 4 CEs). The absolute probability of each possible pathway is shown on the far right, which adds up to a total of 99.93% of all the transitions represented. Major pathways are shown in bold and are made up of direct β decay to an excited state then decay to ground state.

Table 6.3: List of possible pathways from the decay of ^{147}Nd to ground state (GS) of ^{147}Pm.

#	Transition (keV)	Energy Level (keV)	Transition (keV)	Energy Level (keV)	Transition (keV)	Energy Level (keV)	Transition (keV)	Energy Level (keV)	Absolute Probability
1	β - 210.1	685.9	γ - 594.8	91.1	γ - 91.1	GS			9.3E-04
2					CE - 45.92				1.6E-03
3					CE - 83.68				2.3E-04
4					CE - 89.50				5.0E-05
5					CE - 90.78				1.1E-05
6	β - 215.6	680.5	γ - 589.4	91.1	γ - 91.1	GS			1.3E-04
7					CE - 45.921				2.2E-04
8					CE - 83.68				3.2E-05
9					CE - 89.50				6.9E-06
10					CE - 90.78				1.6E-06
11	β - 263.1	632.9	γ - 541.8	91.1	γ - 91.1	GS			6.3E-05
12					CE - 45.92				1.1E-04
13					CE - 83.68				1.6E-05
14					CE - 89.50				3.4E-06
15					CE - 90.78				7.6E-07
16	β - 365	531	γ - 439.9	91.1	γ - 91.1	GS			4.2E-03
17					CE - 45.92				7.2E-03
18					CE - 83.68				1.1E-03
19					CE - 89.50				2.3E-04
20					CE - 90.78				5.1E-05
21	β - 406.8	489.3	γ - 398.2	91.1	γ - 91.1	GS			2.3E-03
22					CE - 45.92				3.9E-03
23					CE - 83.68				5.7E-04
24					CE - 89.50				1.2E-04

Continued on next page

Table 6.3 continued from previous page

#	Transition (keV)	Energy Level (keV)	Transition (keV)	Energy Level (keV)	Transition (keV)	Energy Level (keV)	Transition (keV)	Energy Level (keV)	Absolute Probability
25					CE - 90.78				2.8E-05
26	β - 485.5	410.5	γ - 319.4	91.1	γ - 91.1	GS			1.7E-03
27					CE - 45.92				2.9E-03
28					CE - 83.68				4.2E-04
29					CE - 89.50				9.1E-05
30					CE - 90.78				2.0E-05
31	β - 485.5	410.5	γ - 319.4	91.1	γ - 91.1	GS			1.2E-04
32					CE - 45.92				2.0E-04
33					CE - 83.68				3.0E-05
34					CE - 89.50				6.3E-06
35					CE - 90.78				1.4E-06
36	β - 210.1	685.9	γ - 275.4	410.5	γ - 319.4	91.1	γ - 91.1	GS	3.0E-03
37							CE - 45.92		5.2E-03
38							CE - 83.68		7.5E-04
39							CE - 89.50		1.6E-04
40							CE - 90.78		3.6E-05
41	β - 210.1	685.9	γ - 275.4	410.5	CE - 274.23	91.1	γ - 91.1	GS	2.1E-04
42							CE - 45.92		3.6E-04
43							CE - 83.68		5.2E-05
44							CE - 89.50		1.1E-05
45							CE - 90.78		2.5E-06
46	β - 210.1	685.9	γ - 196.6	489.3	γ - 398.2	91.1	γ - 91.1	GS	7.3E-04
47							CE - 45.92		1.2E-03
48							CE - 83.68		1.8E-04
49							CE - 89.50		3.9E-05
50							CE - 90.78		8.8E-06
51	β - 365	531	γ - 120.5	410.5	γ - 319.4	91.1	γ - 91.1	GS	1.2E-03
52							CE - 45.92		2.1E-03
53							CE - 83.68		3.1E-04
54							CE - 89.50		6.6E-05
55							CE - 90.78		1.5E-05
56	β - 365	531	γ - 120.5	410.5	CE - 274.227	91.1	γ - 91.1	GS	8.7E-05
57							CE - 45.92		1.5E-04
58							CE - 83.68		2.2E-05
59							CE - 89.50		4.6E-06
60							CE - 90.78		1.0E-06

Continued on next page

Table 6.3 continued from previous page

#	Transition (keV)	Energy Level (keV)	Transition (keV)	Energy Level (keV)	Transition (keV)	Energy Level (keV)	Transition (keV)	Energy Level (keV)	Absolute Probability
61	β - 365	531	γ - 120.5	410.5	γ - 319.4	91.1	γ - 91.1	GS	9.6E-04
62							CE - 45.92		1.6E-03
63							CE - 83.68		2.4E-04
64							CE - 89.50		5.1E-05
65							CE - 90.78		1.2E-05
66	β - 365	531	γ - 120.5	410.5	CE - 274.227	91.1	γ - 91.1	GS	6.7E-05
67							CE - 45.92		1.1E-04
68							CE - 83.68		1.7E-05
69							CE - 89.50		3.6E-06
70							CE - 90.78		8.1E-07
71	β - 210.1	685.9	γ - 685.9	GS					8.9E-03
72	β - 215.6	680.4	γ - 680.4						2.9E-04
73	**β - 365**	**531**	**γ - 531**	**GS**					**1.3E-01**
74			CE - 485.83						1.8E-03
75	β - 406.8	489.2	γ - 489.2	GS					1.6E-03
76	β - 365	531	γ - 408.5						0.0E+00
77	**β - 804.9**	**91.1**	**γ - 91.1**	**GS**					**2.6E-01**
78			**CE - 45.92**						**4.5E-01**
79			**CE - 83.68**						**6.6E-02**
80			CE - 89.50						1.4E-02
81			CE - 90.78						3.2E-03
82	β - 896	GS							1.5E-03

In order to compare simulations with measured data, the exact combination of simulated gas counter efficiencies is determined by the measurement. These measurements are dependent on the ability to detect a specific γ-ray in coincidence with a β particle. As such, the simulation is limited to those types of transitions. Decays where only a β particle and CE are emitted (without some γ-ray) are not determined through measurements. Those transitions that do not emit a γ-ray are used to determine the total gas counter efficiency for ^{147}Nd, but do not play a role in determining gas counter efficiencies for a $\beta\gamma$ coincidence event.

If a β particle is missed by the gas counter (or does not deposit enough energy to surpass the electronic threshold) and the γ-ray is detected, the emission of a CE could result in a detectable $\beta\gamma$ coincience event. The decay of a β particle and CE occurs on a time scale that is short enough to assume a single event in the gas counter. In this case, the energy deposited within the gas counter would be a combination of the energy from both the β particle and CE. This type of event results in a higher overall gas counter efficiency for detection of a γ-ray.

For example the ability to detect a β particle gated on a 319.4 keV γ-ray is made up of direct β population of the 410.5 keV excited state and those transitions that feed the excited state. A decay of a CE from the 410.5 keV excited state will not produce a 319.4 keV γ-ray and is not considered in the gas counter efficiency. Transitions 26-40, 51-55, and 61-65 (Table 6.3) all result in the emission of a 319 keV γ-ray, so the β efficiency gated on this γ-ray will be a combination of those particular β transitions. In total, the probability to see a 319.4 keV γ-ray is made up of 1.58% feeding and 0.51% direct decay for a total of 2.09% of all possible transitions.

Simulation of the daughter, ^{147}Pm, is relatively simple as there is one major transition that directly populates the ground state. The gas counter efficiency associated to ^{147}Pm is determined purely through simulation of a β particle with an end-point energy of 224.6 keV[9]. Due to the low $E_{\beta_{max}}$ of ^{147}Pm, the emitted β particles are highly attenuated in the source foil, which immediately reduces the efficiency of detection. Imposing thresholds on the energy deposited further reduces the efficiencies, but at a lesser rate.

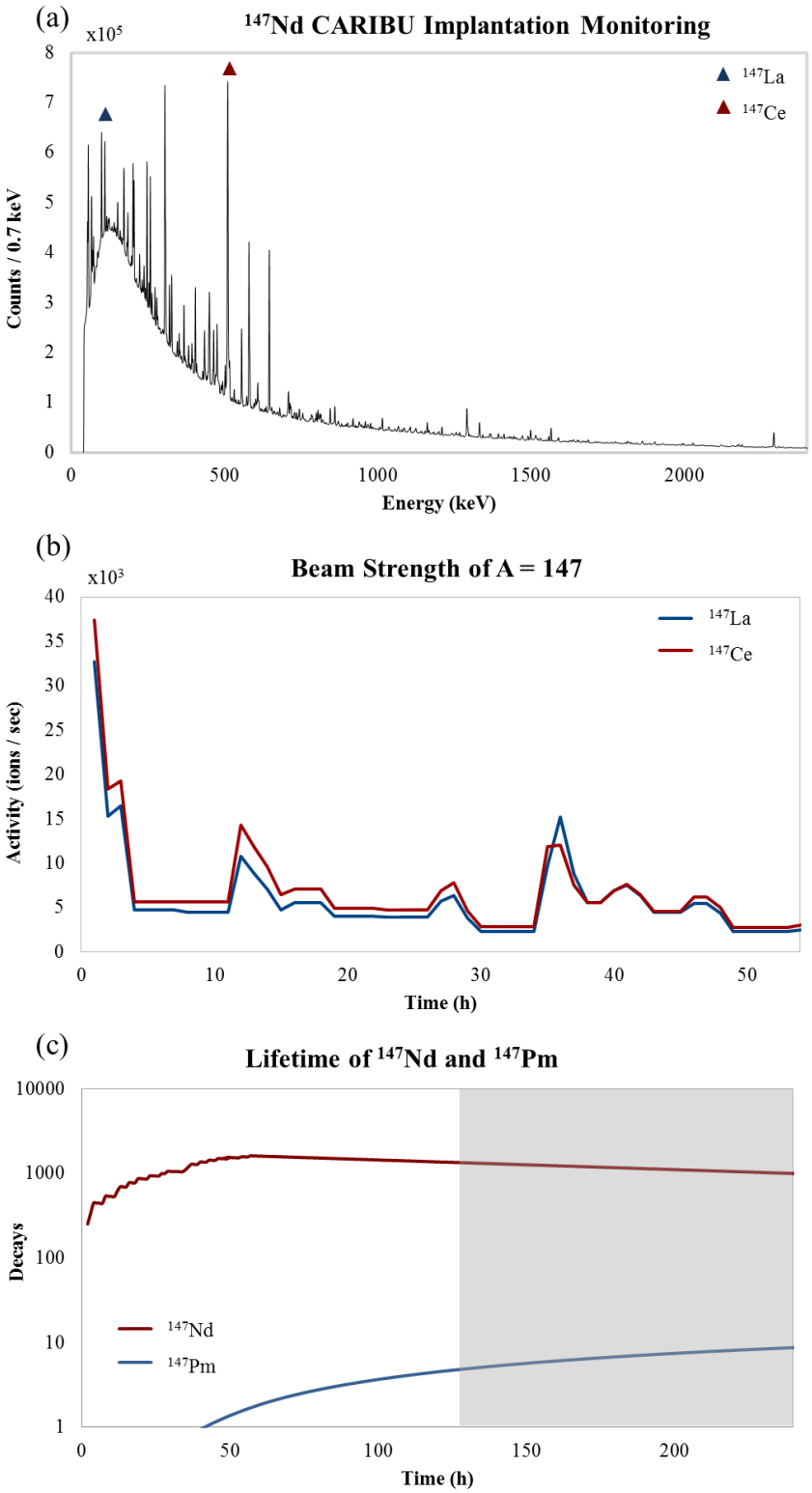

Figure 6.4: (a) γ-ray spectrum of the CARIBU beam monitoring of mass 147 isotopes. (b) Beam intensity over the length of the measurement. (c) Growth and decay of ^{147}Nd and ^{147}Pm. The gray section indicates the time during measurement at TAMU.

Table 6.4: Simulated results for gas counter efficiency of a 0.2 μm CARIBU-made ^{147}Nd/^{147}Pm source.

Detector Efficiency for ^{147}Nd				
	>0.5 keV	>1.0 keV	>1.5 keV	>2.0 keV
Total Gas Counter Efficiency for ^{147}Nd	0.9920	0.9901	0.9848	0.9714
β Gated on 91.105 keV γ-ray	0.9886	0.9834	0.9668	0.9244
β Gated on 117.98 keV γ-ray				
β Gated on 120.48 keV γ-ray	0.9919	0.9910	0.9895	0.9865
β Gated on 196.64 keV γ-ray	0.9836	0.9827	0.9811	0.9791
β Gated on 240.5 keV γ-ray				
β Gated on 271.87 keV γ-ray				
β Gated on 275.374 keV γ-ray	0.9847	0.9838	0.9823	0.9804
β Gated on 319.411 keV γ-ray	0.9898	0.9889	0.9874	0.9845
β Gated on 398.155 keV γ-ray	0.9903	0.9893	0.9876	0.9840
β Gated on 410.48 keV γ-ray	0.9815	0.9780	0.9711	0.9537
β Gated on 439.895 keV γ-ray	0.9914	0.9904	0.9888	0.9856
β Gated on 489.24 keV γ-ray	0.9771	0.9740	0.9688	0.9567
β Gated on 531.016 keV γ-ray	0.9739	0.9709	0.9663	0.9567
β Gated on 541.83 keV γ-ray	0.9873	0.9864	0.9849	0.9829
β Gated on 589.35 keV γ-ray	0.9841	0.9831	0.9816	0.9796
β Gated on 594.8 keV γ-ray	0.9836	0.9827	0.9811	0.9791
β Gated on 680.52 keV γ-ray	0.9518	0.9491	0.9445	0.9388
β Gated on 685.9 keV γ-ray	0.9503	0.9477	0.9431	0.9372
Total Gas Counter Efficiency for ^{147}Pm				
	>0.5 keV	>1.0 keV	>1.5 keV	>2.0 keV
Total Gas Counter Efficiency for ^{147}Pm	0.9528	0.9502	0.9457	0.9400

6.2 ^{147}Nd CARIBU-Produced Source Measurement

For the final measurement of ^{147}Nd, a source was produced at CARIBU and measured at TAMU. Small amounts of contamination within the source were detected in the form of ^{131}I ($t_{1/2}$= 8.0 d) and ^{103}Ru ($t_{1/2}$= 39.2 d). These isotopes have comparable half-lives with ^{147}Nd ($t_{1/2}$= 11.0 d). As such, it is not possible to wait out their decays and measure the source

at a later time (as with the ^{144}Ce decay). These isotopes are quantified using the detected γ-rays within the source and corrected.

From the spontaneous fission of ^{252}Cf, the majority of fission products of mass 147 are made up of ^{147}La ($t_{1/2}$= 4.06 s) and ^{147}Ce ($t_{1/2}$= 56.4 s) isotopes. The short half-lives of these isotopes result in a source made entirely of ^{147}Nd in an hour. It is possible for ^{147}La to emit a neutron (0.04% of decays) and become an isotope with mass 146, however, the decay chain results in short-lived isotopes that will decay to a stable form within a matter of hours.

Looking at the CARIBU spectra of measured γ-rays summed over the length of the implantation (Fig. 6.4a), many peaks are detected. Most peaks belong to isotopes along the 147 chain. From this measurement, it is difficult to draw conclusions about potential contamination present within this source.

The most intense γ-ray transitions from ^{147}La (103.9 keV) and ^{147}Ce (580.3 keV) were monitored to gain an understanding of the beam intensity during collection (Fig. 6.4b). At first the beam was quite strong then over time the beam lost its original intensity and settled into a rate that was similar to mass 144 collection. The source was collected over a period of 63 h and produced a source with an original strength of $\sim$ 1650 Bq.

Once collection terminated, the source was removed from the beam and left to sit for a few hours to allow the short-lived isotopes to decay. As ^{147}Nd decays, it populates ^{147}Pm which decays at a much slower rate comparatively (Fig. 6.4c). The growth during CARIBU implantation can be seen during the beginning hours then subsequent decay over time. The gray section indicates the period of time when measurement of the source took place. Roughly 3 d after collection, the source arrived at TAMU.

Before start of the measurement, a voltage plateau was measured for the gas counter using this ^{147}Nd source. The source strength at this time was 1367 Bq determined from measurements of the source inside the gas counter. The resulting voltage plateau was almost ideal.

The plateau region extended over 250 V (Fig. 4.9a) with changes less than 1% over the entire range (Fig. 4.9b). Everything about this measurement confirms the gas counter is operating as expected and a marked improvement over the first voltage plateau performed during the first ^{95}Zr and ^{144}Ce source measurements. The operating voltage was set at 2400 V.

All sources were removed from the vicinity and a background of both the γ-rays and gas counter detector was performed. The γ-ray background was measured over a period of 9.75 d. A shield was placed over the HPGe detector head so as to reduce γ-ray background radiation interference. With the HPGe shielded, the γ-ray background rate was reduced by a factor of 2 compared to an un-shielded measurement. Several background measurements of the gas counter were taken over this period to confirm the lack of the Malter effect that was seen in previous measurements (Section 4.3.1). The resulting gas counter background was determined to be 0.70(5) cps.

The ^{147}Nd source was placed inside the gas counter and the distance between the source and HPGe detector head was measured at 152.9(1) mm. Measurements of the γ-rays, β particles, and $\beta\gamma$ coincidence events were performed over a period of 6.8 days with a source activity of 1172 Bq averaged over the length of the measurement. The major peaks from ^{147}Nd are identified and clearly seen over the noise of the background (Fig. 6.5a).

Once the dedicated background is subtracted from the source spectrum (Fig. 6.5b), the peaks associated to the decay of ^{147}Nd are clearly visible. Other peaks shown arise from decay of the contaminants and background radiation associated to the decay of uranium and thorium. All peaks have been identified, which suggests there are no other sources of contamination present within the source. Comparing the size of the peaks of ^{147}Nd and those that belong to ^{103}Ru or ^{131}I, the level of contamination is quite small compared to the source and should not result in a large correction to the data. A dip in the background subtracted γ-ray spectrum can be seen around 662 keV, which could be an external source of radiation present within the vicinity that has decayed/moved between the time of the

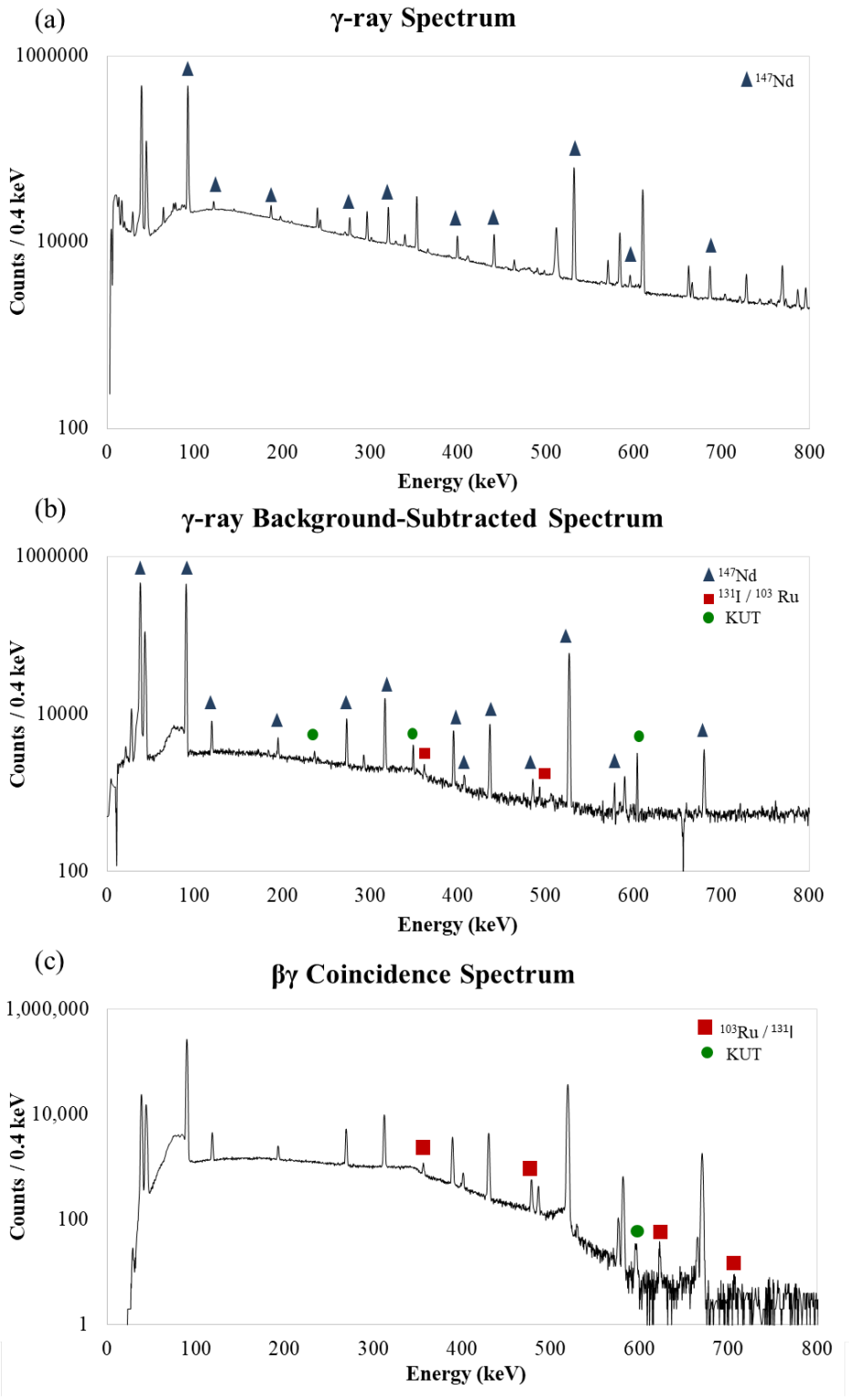

Figure 6.5: (a) γ-ray spectrum, (b) background subtracted γ-ray spectrum, and (c) measured coincidence spectrum of the CARIBU ^{147}Nd/^{147}Pm source.

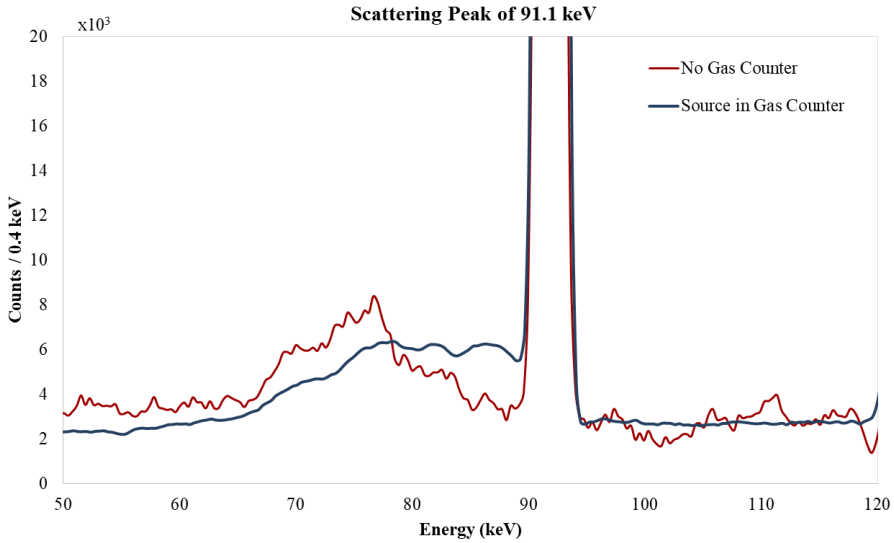

Figure 6.6: Two γ-ray spectra overlaid showing the effect of the gas counter on the 91.1 keV peak. These low energy γ-rays scatter off the copper housing and produce a broad peak on the low energy side of the 91.1 keV γ-ray.

^{147}Nd and background measurement causing an over subtraction from the background in this region.

γ-rays in coincidence with gas counter events are shown in Fig. 6.5c. This spectrum is extremely clean in the sense that most peaks belong to the source. Small background radiation peaks can be seen in the $\beta\gamma$ coincidence measurement due to the relatively high activity of the source in the gas counter and the high level of γ-ray background, which is detected within the 2 μs coincidence time range. These events are accidental and are corrected for by imposing a gate on the TDC peak and limiting that window to include only those events that occur on a shortened time scale. However, it does not entirely remove those peaks attributed to background as can be seen by Fig. 6.5c.

In both γ-ray and $\beta\gamma$ coincidence spectra, there is a large shelf to the left of the 91.1 keV peak. This shelf on the low energy side of the peak is due to scattering of these γ-rays from the gas counter housing. Fig. 6.6 shows a measurement of the γ-rays emitted from the ^{147}Nd

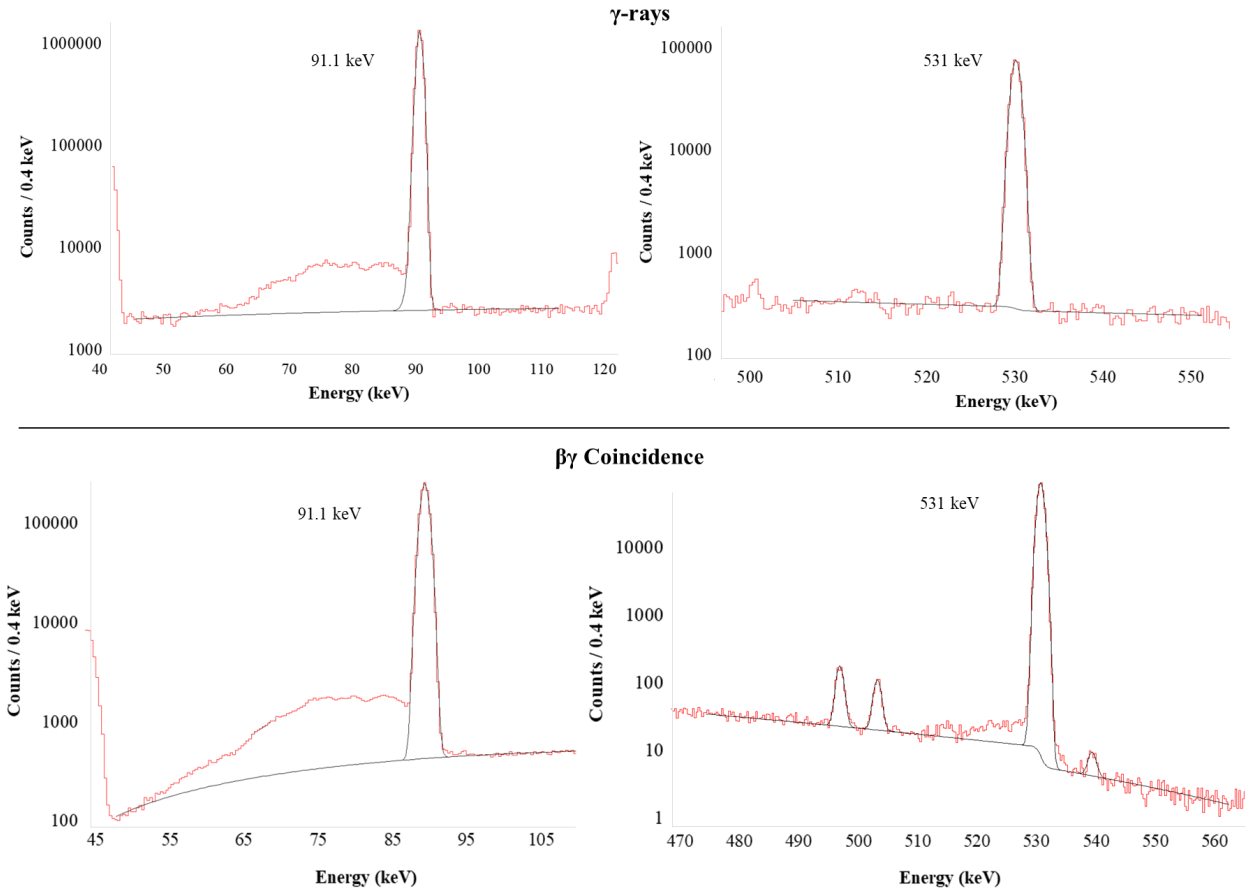

Figure 6.7: Sample fits of the γ-ray and $\beta\gamma$ peaks for 91.1 and 531 keV transitions of a ^{147}Nd source.

source both within and outside of the gas counter overlaid and zoomed in on the base of the 91.1 keV peak. These spectra have been normalized for the purpose of making a comparison. The blue line in the spectrum shows a shelf, while the red line has no shelf because the gas counter was removed during the specific measurement. This identification is important because it determines the left and right background levels around this peak. The background is relatively straight with a small step for the low energy side. There still exists a broad peak at around 75 keV that is most likely attributed to these γ-rays scattering off the aluminum holder that supports the foil. This holder cannot be removed from the measurement and its effect remains speculation. However, it is not present within the background measurement for peaks in this energy range, which suggests it has something to do with the geometry of

Table 6.5: Measured peak rates for γ-ray and $\beta\gamma$ coincidence measurements of ^{147}Nd/^{147}Pm CARIBU source.

γ Energy (keV)	γ-ray	$\beta\gamma$ Coincidence
91.1	3.411 (4)	3.277 (1)
120.48	0.041 (1)	0.040 (12)
196.64	0.016 (1)	0.015 (28)
275.37	0.055 (1)	0.054 (9)
319.4	0.125 (1)	0.119 (5)
398.16	0.046 (1)	0.044 (9)
410.48	0.006 (1)	0.005 (38)
439.9	0.061 (1)	0.058 (8)
489.24	0.007 (1)	0.006 (28)
531	0.577 (1)	0.545 (2)
589.35	0.002 (0)	0.001 (57)
594.8	0.011 (1)	0.010 (19)
680.52	0.001 (1)	0.001 (76)
685.9	0.030 (1)	0.028 (10)

the measurement of the source. It should be noted the red line has less statistics than the blue line causing an irregular count rate.

Peak rates for γ and $\beta\gamma$ coincidences are shown in Table 6.5. Sample fits of the peak are shown in Fig. 6.7. Rates for both measurements are relatively low for the majority of the transitions due to the small probability of a decay emitting a γ-ray. The breakdown of uncertainty contributions is shown in Table 6.6. The two major transitions at 91.1 and 531 keV have the lowest uncertainties, which can be attributed mainly to their high statistics resulting in low peak-to-background levels.

A measured TDC spectrum for the $\beta\gamma$ coincidence measurement is shown in Fig. 6.8. All the major γ-ray transitions gated on a β particle are represented. Those transitions that are highly converted (91.1 and 120.5 keV) show a spread in their TDC timing which lengthens the time range of gas counter detection compared with the detection of a γ-ray. A possible

Table 6.6: Uncertainty contributions associated to the γ-ray peak analysis for ^{147}Nd/^{147}Pm CARIBU source.

γ **Energy (keV)**	Energy	(keV)	Different Fits of Peak	1σ Shifts in Gain	0.5% Change in Normalizations	**Absolute Uncertainty in γ-ray Peak**
91.1	0.095%	0.034%	0.021%	0.027%	0.009%	**0.107%**
120.5	1.212%	3.088%	0.062%	1.069%	0.195%	**3.492%**
196.6	2.939%	5.448%	2.470%	1.444%	0.823%	**6.869%**
275.4	0.885%	1.439%	0.100%	0.053%	0.047%	**1.694%**
319.4	0.519%	0.564%	0.274%	0.140%	0.208%	**0.852%**
364.2	4.778%	11.749%	1.063%	3.681%	3.473%	**13.697%**
398.2	0.925%	1.200%	0.129%	0.605%	0.542%	**1.724%**
410.5	3.477%	8.772%	5.349%	5.847%	5.143%	**13.353%**
439.9	0.714%	0.801%	0.447%	0.203%	0.273%	**1.211%**
489.2	3.233%	7.493%	1.921%	1.051%	1.483%	**8.579%**
497	7.679%	12.434%	2.961%	0.900%	2.918%	**15.221%**
531	0.203%	0.080%	0.041%	0.018%	0.010%	**0.223%**
589.4	6.897%	17.646%	2.293%	1.399%	5.351%	**19.869%**
594.8	2.132%	3.872%	1.306%	1.805%	1.152%	**5.083%**
680.5	16.322%	54.203%	7.495%	3.797%	11.159%	**58.306%**
685.9	1.087%	1.673%	0.388%	0.112%	0.353%	**2.066%**

explanation of the broadening of the TDC peak for these transitions is the slightly different time scale of the CE detection. Conversely, those transitions that are not converted or are converted at a low rate do not show this TDC peak broadening.

Both γ-ray and coincidence rates are decay-corrected to a specific reference time (Eq. 2.13) so that a comparison can be made to determine gas counter efficiency. This alteration corrects for differences in measurement times and dead times between γ-ray and $\beta\gamma$ coincidence measurements. A decay correction of 4.67×10^{-6} was applied to the coincidence measurement and 3.65×10^{-6} was applied to the γ-ray measurement. This correction accurately accounts for the coincidence measurement duration to be 80% to that of the γ-ray measurement

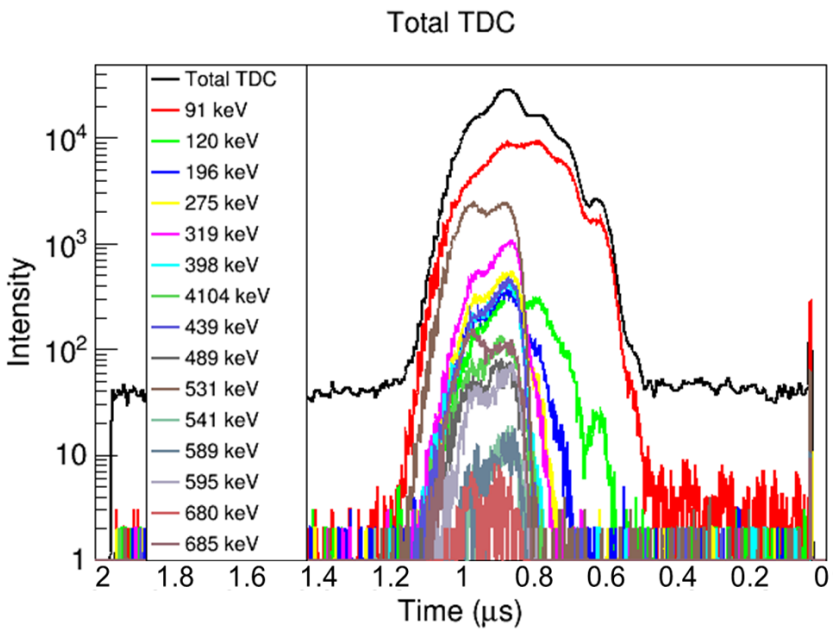

Figure 6.8: TDC spectrum for the measurement of ^{147}Nd source.

duration. This correction uses the measured half-life of ^{147}Nd which is known very well ($t_{1/2}$= 10.98(1) d) and results in a negligible uncertainty contribution.

A comparison between measured and simulated deposition of energy within the gas counter was made using the coincidence system. Only those particles that were in coincidence with a γ-ray event were compared. The deposition of energy is a result of these particles depositing energy through interactions with methane detection gas. Comparing the total deposition of energy between measured and simulated data, good agreement is found (Fig. 6.9a). Both spectra line up well with one another and allow energy information to be obtained from the measurement data using the simulated data. An average energy deposition of a particle within the gas counter from the decay of ^{147}Nd/^{147}Pm was 3.1 keV and an electronic threshold is set to 1.1 keV during the measurement.

Looking at individual transitions of gas counter particles gated on 91.1 and 531 keV γ-rays, deposition of energy spectra were produced (Fig. 6.9b and Fig. 6.9c). In both cases, a β decay to this energy level and subsequent decay to ground state by emission of a γ-ray occurs,

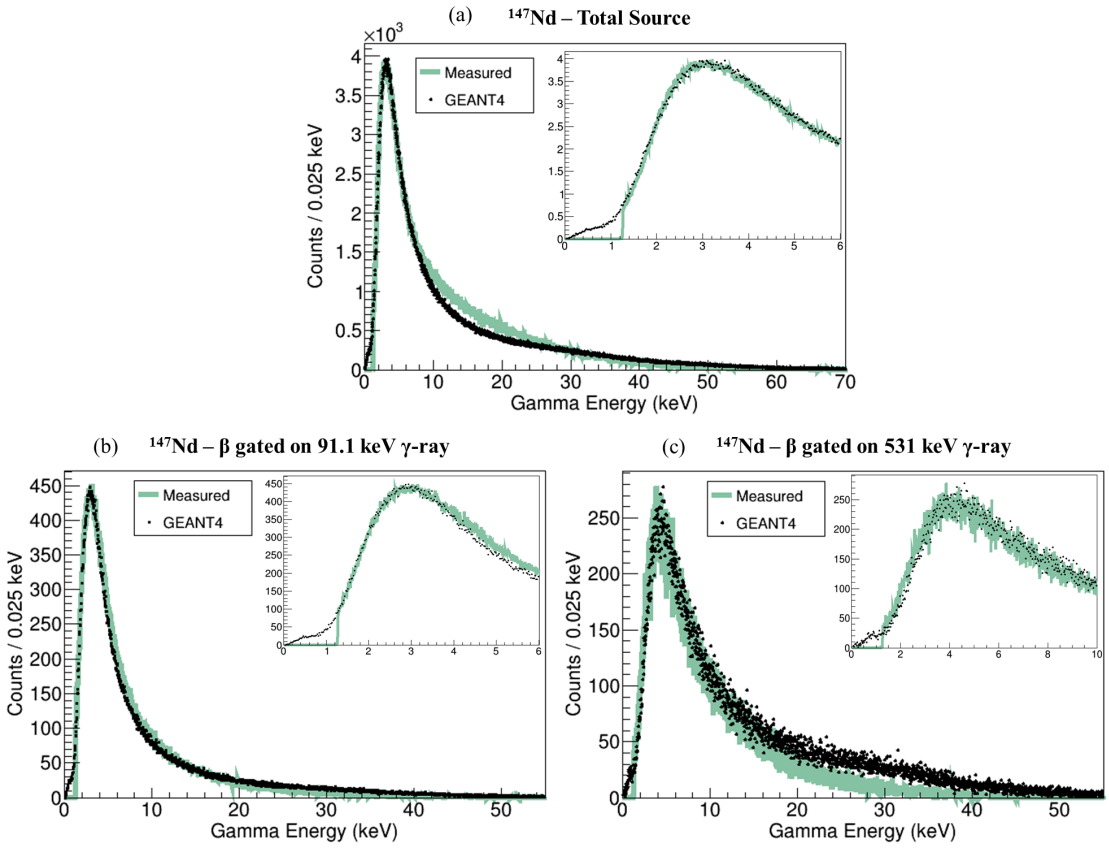

Figure 6.9: (a) A comparison of the deposition of energy spectra between measured and GEANT4 simulated data. Gas counter events gated on the (b) 91.1 and (c) 531 keV γ-rays agree well with simulated data due to the lack of CEs associated to these decays.

resulting in relatively simple decay paths. These transitions are almost perfectly recreated using simulated data, which suggests the β decay is accurately represented by simulations. It is important to note, the average energy the particles deposit is different between the two transitions due to the differences in $E_{\beta_{max}}$ values. For the transition emitting a 91.1 keV γ-ray, the $E_{\beta_{max}}$ is high and less average energy is deposited per event. For the transition emitting a 531 keV γ-ray, the $E_{\beta_{max}}$ is low in comparison and deposits a higher average energy within the gas counter.

Gas counter efficiency values are calculated in Table 6.7 and compared with simulated values using a threshold of 1.1 keV. In most cases, as the energy of the β particle decreases, the efficiency for detection also decreases. The main reason for this trend is a result of attenuation

of the β particles within the source foil. Lower energy β particles interact more with the carbon atoms of the foil and a larger fraction will be absorbed. β particles with energies of 450 keV or greater are affected by the electronic threshold more so than attenuation. These higher energy β particles interact less with the detection gas and, as such deposit, less energy before escaping the chamber. The energy deposited may not be enough to distinguish between the general noise of the electronics because it is below the imposed threshold level. There is good agreement between GEANT4 simulated efficiencies and those experimentally determined within error. This gives confidence to both measured and simulated values.

Table 6.7: Measured and GEANT4 simulated gas counter efficiency values for a ^{147}Nd/^{147}Pm CARIBU-made source.

β Energy (keV)	GEANT4	Measured
804.9 β when Gated on 91.1 keV	0.982	0.985(1)
365 β when Gated on 120.48 keV	0.991	1.001(12)
210.1 β when Gated on 196.64 keV	0.982	0.939(70)
210.1 β when Gated on 275.37 keV	0.984	1.007(19)
485.5 β when Gated on 319.4 keV	0.989	0.978(10)
406.7 β when Gated on 398.16 keV	0.989	1.000(9)
485.5 β when Gated on 410.48 keV	0.977	0.921(133)
365 β when Gated on 439.9 keV	0.990	0.977(14)
406.7 β when Gated on 489.24 keV	0.973	0.960(84)
365 β when Gated on 531 keV	0.970	0.968(2)
215.6 β when Gated on 589.35 keV	0.983	0.656(136)
210.1 β when Gated on 594.8 keV	0.982	0.927(50)
215.6 β when Gated on 680.52 keV	0.948	0.622(349)
210.1 β when Gated on 685.9 keV	0.947	0.938(9)

An additional piece of information required for determination of the γ-ray branching ratio is the total isotopic efficiencies of ^{147}Nd and ^{147}Pm. Calculated values of isotopic gas counter efficiencies are determined purely through simulations by combining the possible transitions

that make up an isotope using literature β branching values. Calculations result in isotopic efficiencies of 0.991(1) for ^{147}Nd and 0.952(2) for ^{147}Pm. Using these isotopic efficiencies, a total gas counter efficiency for the source was determined to be 0.991(2). This value takes into account the relative ratio of ^{147}Nd/^{147}Pm at the time of measurement and corrects for contamination present within the source.

Dead times of the system are relatively small compared to the measurement time. The dead time associated to the γ-ray measurement emitted from the source was determined to be 0.62%. Dead times associated to the coincidence measurement is a sum of the dead times to process a β, γ-ray, and coincidence event. This value was determined to be 0.16%. Differences between the γ-ray and coincidence dead times can be attributed to the large γ-ray background radiation that is detected during the γ-ray measurement, but not the coincidence measurement. During γ-ray measurements, each event is evaluated for energy, whereas during the coincidence event, only those γ-rays which are considered coincidence events are evaluated for energy.

The dead time associated to the measurement of β particles in the gas counter is 0.06%. The low dead time of the gas counter compared to the γ-ray HPGe detector can be attributed to quick dissipation of the electrons moving through methane gas compared to electrons moving through a solid germanium crystal.

Specific isotopic contributions to the measured amount of β particles were determined by calculating the source's growth and decay over time. The total gas counter activity was 1171.58(6) Bq once the contributions of contaminates were removed. This value was calculated by taking the measured β rate, subtracting gas counter background and contaminates, and correcting for total gas counter efficiency of the source. The specifics of the CARIBU measurement (duration and beam intensity) and the decay of the source before and during the measurement were incorporated into the calculation. During the measurement, the ratio of Nd to total source activity is 99.41%, the ratio of Pm to total source activity is 0.59%.

Table 6.8: Calculated γ-ray branching ratio values for a ^{147}Nd/^{147}Pm CARIBU-produced source.

γ-ray Energy (keV)	$R_{\beta\gamma}$ (cps)	R_{β} (cps)	ϵ_{γ}	$\epsilon_{\beta_{total}}$ / ϵ_{β_i}	γ-ray Branching Ratio	NNDC
91.1	3.2766(37)	1154.27(6)	0.009765(30)	0.99483(6)	0.2931(9)	0.2810(70)
120.48	0.0399(14)		0.009240(29)	1.00038(6)	0.00374(5)	0.00376(9)
196.64	0.0148(11)		0.007496(23)	0.99201(6)	0.00172(5)	0.00190(4)
275.37	0.0536(9)		0.005996(18)	0.99312(6)	0.00779(7)	0.00910(19)
319.4	0.1192(11)		0.005385(16)	0.99827(6)	0.0192(1)	0.0213(4)
398.16	0.0444(8)		0.004565(18)	0.99870(6)	0.00843(9)	0.00912(19)
410.48	0.0053(8)		0.004464(18)	0.98838(6)	0.00104(4)	0.00150(3)
439.9	0.0584(7)		0.004259(17)	0.99978(6)	0.01188(10)	0.0128(3)
489.24	0.0063(6)		0.003930(15)	0.98423(6)	0.00141(4)	0.00155(3)
531	0.5448(13)		0.003699(11)	0.98108(6)	0.1301(5)	0.1340(30)
589.35	0.0014(4)		0.003431(15)	0.99248(6)	0.00034(2)	0.00039(3)
594.8	0.0099(6)		0.003410(15)	0.99201(6)	0.00252(5)	0.00283(6)
680.52	0.0007(6)		0.003097(9)	0.95902(6)	0.00019(1)	0.00029(1)
685.9	0.0278(6)		0.003082(9)	0.95760(6)	0.00816(8)	0.00886(18)

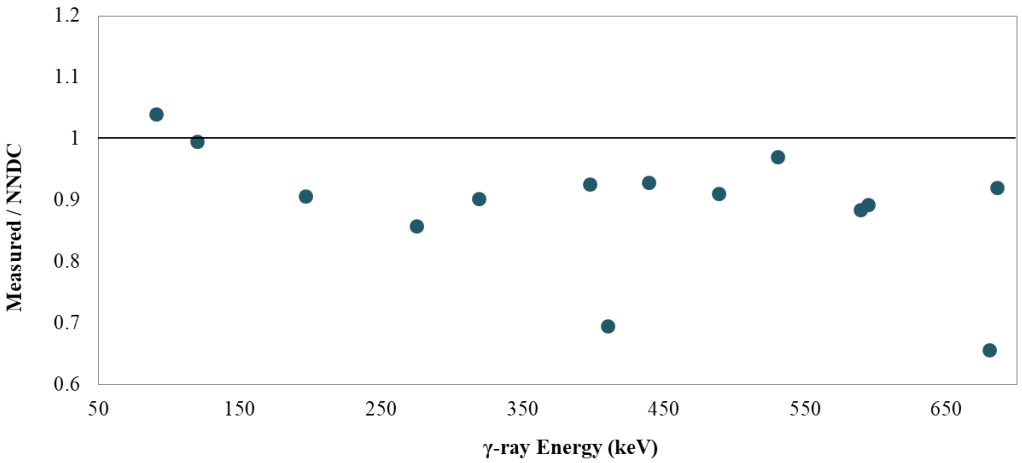

Figure 6.10: A comparison between literature γ-ray branching values and those determined by this method. A value close to 1 is a good agreement.

Measurement of the source was performed days after its creation, which effectively minimizes the contribution of the ^{147}Pm to the activity of the source (Fig. 6.3b).

The observed contribution of each isotope is determined by correcting the source activities for gas counter efficiencies. These rates are the detected amount of radiation given off from the source. The total measured gas counter rate was 1160.83(6) *cps*, of which 1154.27 *cps* is ^{147}Nd and 0.56 *cps* is ^{147}Pm. Only the ^{147}Nd β rate is used in calculation of γ-ray branching ratios due to the low probability of detection of ^{147}Pm γ-rays.

With the necessary information present, calculated γ-ray branching ratios along with the contributions and uncertainties are shown in Table 6.8. Due to the large amount of transitions of ^{147}Nd, a comparison between literature values and experimental values is shown in Fig. 6.10. For most values, the experimental analysis results in γ-ray branching ratio values that are less than those quoted in literature[9]. For the most intense transition (91.1 keV), the value is actually larger than that of the literature value.

Chapter 7

Future Work and Conclusion

7.1 Future Work

Efforts to develop a method to accurately reduce γ-ray branching ratios for fission products with relatively long half-lives have shown to be effective. Future applications of this method will be applied to other fission products with half-lives of a day or longer. Fission products of interest to stockpile stewardship and nuclear forensics will be studied for effectiveness and application of this method.

7.1.1 Method Improvements

Efforts are underway to move measurements of γ-rays and $\beta\gamma$ coincidence from Texas A&M University (TAMU) to Lawrence Livermore National Laboratory (LLNL). The reasoning for this transition is purely a choice of convenience. Scheduling conflicts, gas counter and radioactive source shipments, and instability of systems increase the complexity of this measurement. Between source creation at CARIBU (roughly one week) and measurement a

few days thereafter (two weeks or more), the scheduling of these systems need to overlap and both need to be available. Both facilities are user facilities and become booked many months in advance, requiring the measurement to be scheduled before the previous analysis is complete or waiting months until the scheduled time to perform the experiment. Also, if there were some type of issue during the measurement, there is no time to fully explore the problem before the scheduled time of the experiment runs out. Higher statistics could have been achieved for several of the measurements if the experiment were allowed to run for a longer duration.

Each experiment requires both the gas counter and radioactive source to be shipped to TAMU. The gas counter requires several days to be set up, conditioned, and tested to assure it is operating with high precision. Shipping the gas counter, while possible, holds some risk of damaging the anode wires, windows, or sealed system that then requires time out of the scheduled experiment to fix and restore back to operating conditions. Shipping the CARIBU source holds the same type of risk, but it is more of an issue as to its owner. The shipment of radioactive sources is highly regulated and the more times it is shipped the more complex tracking its specific movement becomes. This could be made easier if shipment from CARIBU went only to LLNL. The gas counter could be ready to measure once the source arrives as it would not have to be shuffled about to different institutions.

The system at TAMU has had some instability problems throughout this measurement. In order to prevent the loss of large amount of measurement data, the system was checked every 4 hours requiring the assistance of several scientists (or not). Also, this is not our system and making any changes required the help of the TAMU staff scientist. As such, their involvement in the project was heavily relied upon. Also, differences in measurement systems of the γ-rays and $\beta\gamma$ coincidence detection created several corrections to the data, which increased the uncertainty associated to the measurements. These alterations could be fixed if the system was recreated at LLNL.

Furthermore, the ^{252}Cf spontaneous fission source at CARIBU has been in the process of upgrading to a more active source. The half-life of ^{252}Cf is 2.65 years and its intensity at the start of the first collection (June 2016) to the final collection (Dec. 2017) had reduced by over 30%. A stronger source could increase the implantation rate of fission product to the foil. Less time would be needed for collection of the ions or more active sources could be created with a stronger ^{252}Cf source.

7.2 Conclusion

The work presented in this dissertation combines state-of-the-art radioactive beams of fission products and high precision equipment to produce measurements of γ-ray branching ratios that are known to $\sim$1%. The relative ease of the measurement allows for any generic fission product (with a half-life greater than one day) to be analyzed. Any of these types of fission products of ^{252}Cf can be studied, creating a plethora of isotopes available for measurement.

The use of ^{95}Zr as a test source for this method and subsequent application of the fission products ^{144}Ce and ^{147}Nd create a well-reasoned argument for the validity of this approach. Sources created at the CARIBU facility prove that method of radioactive source creation is viable and a consistent mechanism to create sources of high activity and low contamination. Measurements of the γ-rays and $\beta\gamma$ coincidences can be made with high precision using meticulously calibrated systems. Together these measurements serve to increase the certainty of nuclear data concerning the decay of fission products.

Bibliography

[1] M. B. Chadwick, M. Herman, P. Obložinský, *et al.*, "ENDF/B-VII.1 nuclear data for science and technology: Cross sections, covariances, fission product yields and decay data," *Nuclear Data Sheets*, vol. 112, no. 12, pp. 2887 – 2996, 2011. Special Issue on ENDF/B-VII.1 Library.

[2] J. I. Katakura, "JENDL FP Decay Data File 2011 and Fission Yields Data File 2011," 2012.

[3] G. Savard and R. Pardo, "Proposal for the ^{252}Cf source upgrade to the Atlas Facility," 2005.

[4] G. Savard, A. Levand, R. Pardo, *et al.*, "The CARIBU facility," in *JPS Conf. Proc. 6, 010008*, 2015.

[5] I. Rittersdorf, "Gamma-ray spectroscopy," *Advances in Physics*, 2007.

[6] G. F. Knoll, *Radiation Detection and Measurement*. John Wiley & Sons, Inc., 4th ed., 2010.

[7] R. G. Helmer, J. C. Hardy, V. E. Iacob, *et al.*, "The use of Monte Carlo calculations in the determination of a Ge detector efficiency curve," *Nuclear Instruments and Methods in Physics Research Section A: Accelerators, Spectrometers, Detectors and Associated Equipment*, vol. 511, no. 3, pp. 360 – 381, 2003.

[8] Cross Section Evaluation Working Group, "ENDF/B-VI summary documentation, report BNL-NCS-17541(ENDF-201), edited by P. F. Rose," tech. rep., National Nuclear Data Center, Brookhaven National Laboratory, Upton, NY, USA., 1991.

[9] R. R. Kinsey, C. L. Dunford, J. K. Tuli, *et al.*, "The NUDAT/PCNUDAT program for nuclear data," vol. 2, 01 1996.

[10] A. A. Sonzogni, "Nuclear data sheets A = 95," pp. Data extracted from the ENSDF database, revision of Dec. 1, 2000.

[11] J. L. Kulp, "Dating with carbon 14," *Journal of Chemical Education*, vol. 30, no. 9, p. 432, 1953.

[12] B. N. Taylor and P. J. Mohr, "CODATA value: Proton-electron mass ratio," *The NIST Reference on Constants, Units, and Uncertainty*, 2006.

[13] E. Segrè, "Spontaneous fission," *Physics Review*, vol. 86, pp. 21–28, Apr. 1952.

[14] E. Rutherfod, *Radio-activity*. University Press, 1905.

[15] H. Bateman, "The solution of a system of differential equations occurring in the theory of radioactive transformations," *In Proc. Cambridge Philos. Soc.*, vol. 15, no. pt V, pp. 423 – 427, 1910.

[16] R. A. Anderl and C. H. Cargo, "A laboratory-scale shielded cell for ^{252}Cf," in *The 27th Conference on Rernote Systems Technology*, 1979.

[17] G. Savard, J. Clark, C. Boudreau, *et al.*, "Development and operation of gas catchers to thermalize fusion–evaporation and fragmentation products," *Nuclear Instruments and Methods in Physics Research Section B: Beam Interactions with Materials and Atoms*, vol. 204, pp. 582 – 586, 2003. 14th International Conference on Electromagnetic Isotope Separators and Techniques Related to their Applications.

[18] F. Herfurth, J. Dilling, A. Kellerbauer, *et al.*, "A linear radiofrequency ion trap for accumulation, bunching, and emittance improvement of radioactive ion beams," *Nuclear Instruments and Methods in Physics Research Section A: Accelerators, Spectrometers, Detectors and Associated Equipment*, vol. 469, no. 2, pp. 254 – 275, 2001.

[19] C. N. Davids and D. Peterson, "A compact high-resolution isobar separator for the CARIBU project," *Nuclear Instruments and Methods in Physics Research Section B: Beam Interactions with Materials and Atoms*, vol. 266, no. 19, pp. 4449 – 4453, 2008. Proceedings of the XVth International Conference on Electromagnetic Isotope Separators and Techniques Related to their Applications.

[20] J. C. Hardy, V. E. Iacob, M. Sanchez-Vega, *et al.*, "Precise efficiency calibration of an HPGe detector: Source measurements and Monte Carlo calculations with sub-percent precision," *Applied Radiation and Isotopes*, vol. 56, no. 1, pp. 65 – 69, 2002. Proceedings of the Conference on Radionuclide Metrology and its A pplications, ICRM'01.

[21] R. G. Helmer, N. Nica, J. C. Hardy, *et al.*, "Precise efficiency calibration of an HPGe detector up to 3.5 MeV, with measurements and Monte Carlo calculations," *Applied Radiation and Isotopes*, vol. 60, no. 2, pp. 173 – 177, 2004. Proceedings of the 14th International Conference on Radionuclide Metrology and its Applications, ICRM 2003.

[22] V. V. Golovko, V. E. Iacob, and J. C. Hardy, "The use of GEANT4 for simulations of a plastic β-detector and its application to efficiency calibration," *Nucl. Instrum. Meth.*, vol. A594, pp. 266–272, 2008.

[23] E. Schönfeld, H. Janssen, R. Klein, *et al.*, "Production of ^{60}Co sources for high-accuracy efficiency calibrations of γ-ray spectrometers," *Applied Radiation and Isotopes*, vol. 56, no. 1, pp. 215 – 221, 2002. Proceedings of the Conference on Radionuclide Metrology and its Applications, ICRM'01.

[24] M. Stano, S. Matejcik, J. D. Skalny, and T. D. Märk, "Electron impact ionization of CH_4: Ionization energies and temperature effects," *Journal of Physics B: Atomic, Molecular and Optical Physics*, vol. 36, no. 2, p. 261, 2003.

[25] V. T. Koslowsky, E. Hagberg, J. C. Hardy, *et al.*, "The half-lives of ^{26m}Al, ^{34}Cl, ^{38m}K: Precision measurements with isotope-separated samples," *Nuclear Physics A*, vol. 405, no. 1, pp. 29 – 39, 1983.

[26] V. T. Koslowsky, E. Hagberg, J. C. Hardy, *et al.*, "The half-lives of ^{42}Sc, ^{46}V, ^{50}Mn, and ^{54}Co," *Nuclear Instruments and Methods in Physics Research Section A: Accelerators, Spectrometers, Detectors and Associated Equipment*, vol. 401, no. 2, pp. 289 – 298, 1997.

[27] H. H. Seliger and L. Cavallo, "The absolute standardization of radioisotopes by 4π counting," *Journal of Research of the National Bureau of Standards*, vol. 47, no. 41, 1951.

[28] S. Yamada and M. Imai, "Analysis of outputs from gas flow counter with respect to plateau curves," *Journal of Nuclear Science and Technology*, vol. 1, no. 9, pp. 343–349, 1964.

[29] R. E. Lee, "Plateau characteristics of Geiger counters with respect to different gas mixtures and pressures," Master's thesis, Missouri University of Science and Technology, 1949.

[30] V. E. Iacob, J. C. Hardy, A. Banu, *et al.*, "Precise half-life measurement of the superallowed β^+ emitter ^{26}Si," *Phys. Rev. C*, vol. 82, p. 035502, Sept. 2010.

[31] V. E. Iacob, J. C. Hardy, L. Chen, *et al.*, "Precise half-life measurement of the superallowed emitter ^{30}S," *Phys. Rev. C*, vol. 97, p. 035501, Mar. 2018.

[32] B. Hyland, D. Melconian, G. C. Ball, *et al.*, "Precision half-life measurement of ^{62}Ga," *Journal of Physics G: Nuclear and Particle Physics*, vol. 31, no. 10, p. S1885, 2005.

[33] J. C. Hardy, V. E. Iacob, H. I. Park, *et al.*, "Ft values measured to $\pm 0.1\%$ for superallowed β transitions: Metrology at sub-second time scales," *Applied Radiation and Isotopes*, vol. 87, pp. 297 – 301, 2014. Proceedings of the 19th International Conference on Radionuclide Metrology and its Applications 17–21 June 2013, Antwerp, Belgium.

[34] J. C. Hardy, V. E. Iacob, M. Sanchez-Vega, *et al.*, "High precision measurement of the superallowed $0^+ \rightarrow 0^+ \beta$ decay of ^{22}Mg," *Phys. Rev. Lett.*, vol. 91, p. 082501, Aug. 2003.

[35] V. E. Iacob, Y. Zhai, T. Al-Abdullah, *et al.*, "β decay of proton-rich nucleus ^{23}Al and astrophysical consequences," *Phys. Rev. C*, vol. 74, p. 045810, Oct. 2006.

[36] D. Melconian, S. Triambak, C. Bordeanu, *et al.*, "β decay of ^{32}Cl: Precision γ-ray spectroscopy and a measurement of isospin-symmetry breaking," *Phys. Rev. C*, vol. 85, p. 025501, Feb. 2012.

[37] N. Nica, J. C. Hardy, V. E. Iacob, *et al.*, "Precise measurement of k-shell fluorescence yield in iridium: An improved test of internal-conversion theory," *Phys. Rev. C*, vol. 71, p. 054320, May 2005.

[38] N. Nica, J. C. Hardy, V. E. Iacob, *et al.*, "Internal conversion coefficients in ^{134}Cs, ^{137}Ba, and ^{139}La: A precise test of theory," *Phys. Rev. C*, vol. 77, p. 034306, Mar. 2008.

[39] N. Nica, J. C. Hardy, V. E. Iacob, *et al.*, "Further test of internal-conversion theory with a measurement in ^{197}Pt," *Phys. Rev. C*, vol. 80, p. 064314, Dec. 2009.

[40] H. I. Park, J. C. Hardy, V. E. Iacob, *et al.*, "Precise measurement of branching ratios in the β decay of ^{38}Ca," *Phys. Rev. C*, vol. 92, p. 015502, July 2015.

[41] D. V. Booker, "The divergence from gaussian of peak shapes in γ-ray spectra observed with germanium detectors," *Journal of Radioanalytical Chemistry*, vol. 48, pp. 83–90, Mar. 1979.

[42] A. H. Fatah and A. H. Ahmed, "Analysis of γ-ray spectra using Levenberg-Marquardt method," vol. 73, pp. 269–274, June 2011.

[43] G. S. Zahn, F. A. Genezini, and M. Moralles, "Evaluation of peak-fitting software for gamma spectrum analysis," Nov. 2015.

[44] D. C. Radford, *Notes on the Use of the Program gf3.* Physics Division of Oak Ridge National Laboratory, 1.1 ed.

[45] The Arizona Carbon Foil Co., "ACF metals' product information 2018," Accessed June 2016.

[46] A. P. Baerg, "The efficiency extrapolation method in coincidence counting," *Nuclear Instruments and Methods*, vol. 112, no. 1, pp. 143 – 150, 1973.

[47] L. Mo, H. Y. Wu, and C. Baldock, "Absolute activity determination of ^{198}Au solid source using $4\pi\beta$-γ coincidence counting corrected by Monte Carlo calculation," vol. 54, pp. 677 – 683, July 2007.

[48] S. Agostinelli, J. Allison, K. Amako, *et al.*, "GEANT4 - a simulation toolkit," *Nuclear Instruments and Methods in Physics Research Section A: Accelerators, Spectrometers, Detectors and Associated Equipment*, vol. 506, no. 3, pp. 250 – 303, 2003.

[49] J. Allison, K. Amako, J. Apostolakis, *et al.*, "GEANT4 developments and applications," *IEEE Transactions on Nuclear Science*, vol. 53, pp. 270–278, Feb. 2006.

[50] J. Allison, K. Amako, J. Apostolakis, *et al.*, "Recent developments in GEANT4," *Nuclear Instruments and Methods in Physics Research Section A: Accelerators, Spectrometers, Detectors and Associated Equipment*, vol. 835, July 2016.

[51] H. Behrens and J. Jänecke, "Landolt-börnstein - group i elementary particles, nuclei and atoms," 1969.

[52] H. Paul, "Shapes of β spectra," *Nuclear Data Sheets. Section A*, vol. 2, no. 3, pp. 281 – 298, 1966.

[53] X. Mougeot, "Reliability of usual assumptions in the calculation of β and ν spectra," *Phys. Rev. C*, vol. 91, p. 055504, May 2015.

[54] J. F. Ziegler, M. Ziegler, and J. Biersack, "SRIM – the stopping and range of ions in matter," *Nuclear Instruments and Methods in Physics Research Section B: Beam Interactions with Materials and Atoms*, vol. 268, no. 11, pp. 1818 – 1823, 2010. 19th International Conference on Ion Beam Analysis.

[55] R. H. Fulmer, D. P. Stricos, and T. F. Ruane, "Neutron absorption cross sections for zirconium-94 and zirconium-96," *Nuclear Science and Engineering*, vol. 46, no. 2, pp. 314–317, 1971.

[56] D. R. Lide, *CRC Handbook of Chemistry and Physics*. Zirconium, New York: CRC Press, 2007–2008 ed.

[57] B. Czajka, K. Pruchniak, and L. Wachowski, "Aluminium and zirconium powders as components of specialty pyrotechnics and rocket propellants," *Institute of Non-Ferrous Metals*, 2012.

[58] H. Ellern, *Military and Civilian Pyrotechnics*. Chemical Publishing Company Inc., 1968.

[59] W. A. Ferrando, "Zirconium as a structural material for naval systems," tech. rep., Naval Surface Weapons Center, 1985.

[60] I. I. Novikov, V. V. Roshchupkin, M. M. Lyakhovitskii, *et al.*, "Investigation of the acoustic properties of zirconium," *Inorganic Materials: Applied Research*, vol. 5, pp. 184–188, Mar. 2014.

[61] W. B. Blumenthal, "Zirconium chemistry in industry," *Journal of Chemical Education*, vol. 39, no. 12, p. 604, 1962.

[62] S. B. Kalidindi, S. Nayak, M. E. Briggs, *et al.*, "Chemical and structural stability of zirconium-based metal–organic frameworks with large three-dimensional pores by linker engineering," *Angewandte Chemie International Edition*, vol. 54, no. 1, pp. 221–226.

[63] J. Meija, T. B. Coplen, M. Berglund, *et al.*, "Isotopic Compositions of the Elements 2013," *IUPAC Technical Report*, vol. 88, pp. 293–306, Jan. 2016.

[64] B. Champine, *Experiments to Improve Nuclear Data for High Energy Density Environments*. PhD thesis, University of California Berkeley, 2016.

[65] K. Debertin, U. Schötzig, K. Walz, and H. Weiss, "γ-ray emission probabilities of the fission products ^{144}Ce/^{144}Pr, ^{106}Rh, ^{95}Zr," *Annals of Nuclear Energy*, vol. 2, no. 1, pp. 37 – 43, 1975.

[66] W. Neumann, "Spurious malter pulses in a 4π proportional counter," *Nuclear Instruments and Methods*, vol. 142, no. 3, pp. 439 – 442, 1977.

[67] J. Va'vra, "Physics and chemistry of aging – early developments," *Nuclear Instruments and Methods in Physics Research Section A: Accelerators, Spectrometers, Detectors and Associated Equipment*, vol. 515, no. 1, pp. 1 – 14, 2003. Proceedings of the International Workshop on Aging Phenomena in Gaseous Detectors.

[68] D. Bravo-Berguño, "SOX: Short distance neutrino oscillations with borexino," *Nuclear and Particle Physics Proceedings*, vol. 273-275, pp. 1760 – 1764, 2016. 37th International Conference on High Energy Physics (ICHEP).

[69] J. Gaffiot, "The SOX experiment," *Nuclear and Particle Physics Proceedings*, vol. 265-266, pp. 129 – 131, 2015. Proceedings of the Neutrino Oscillation Workshop.

[70] L. Lakosi and Á. Veres, "Nondestructive assay of fission products in spent-fuel assemblies using γ and photoneutron activation," *Nuclear Instruments and Methods in Physics Research Section A: Accelerators, Spectrometers, Detectors and Associated Equipment*, vol. 299, no. 1, pp. 463 – 467, 1990.

[71] J. S. Walter, H. Arino, and K. H. Herman, "A new ^{144}Ce/^{144}Pr radioisotope generator system," *The International Journal of Applied Radiation and Isotopes*, vol. 29, no. 9, pp. 575 – 578, 1978.

[72] B. T. Kilbourn, *Cerium and Cerium Compounds*. American Cancer Society, 2003.

[73] K. Reinhardt and H. Winkler, *Cerium Mischmetal, Cerium Alloys, and Cerium Compounds*. American Cancer Society, 2000.

[74] D. Bouzid, N. Belkhie, and T. Aliouane, "Optical glass surfaces polishing by cerium oxide particles," *IOP Conference Series: Materials Science and Engineering*, vol. 28, no. 1, p. 012007, 2012.

[75] T. Montini, M. Melchionna, M. Monai, *et al.*, "Fundamentals and catalytic applications of CeO_2-based materials," *Chemical Reviews*, vol. 116, no. 10, pp. 5987–6041, 2016. PMID: 27120134.

[76] A. Trovarelli, C. de Leitenburg, and G. Dolcetti, "Design better cerium-based oxidation catalysts," *CHEMTECH*, vol. 27, June 1997.

[77] P. G. Harrison, I. K. Ball, W. Azelee, *et al.*, "Nature and surface redox properties of copper(ii)-promoted cerium(iv) oxide co-oxidation catalysts," *Chemistry of Materials*, vol. 12, no. 12, pp. 3715–3725, 2000.

[78] D. R. Mullins, "The surface chemistry of cerium oxide," *Surface Science Reports*, vol. 70, no. 1, pp. 42 – 85, 2015.

[79] J. S. Stroud, "Color-center kinetics in cerium-containing glass," *The Journal of Chemical Physics*, vol. 43, no. 7, pp. 2442–2450, 1965.

[80] J. G. Cuninghame, J. A. B. Goodall, and H. H. Willis, "Absolute yields in the fission of ^{235}U by mono-energetic neutrons of energy 130–1700 kev," vol. 36, pp. 1453–1457, Dec. 1977.

[81] J. Laurec, A. Adam, T. de Bruyne, *et al.*, "Fission product yields of ^{233}U, ^{235}U, ^{238}U, and ^{239}Pu in fields of thermal neutrons, fission neutrons and 14.7-MeV neutrons," *Nuclear Data Sheets*, vol. 111, no. 12, pp. 2965 – 2980, 2010. Nuclear Reaction Data.

[82] H. Kumahora, H. Inoue, and Y. Yoshizawa, "Precision measurement of γ-ray energies in the range 450–600 keV," *Nuclear Instruments and Methods in Physics Research*, vol. 206, no. 3, pp. 489 – 495, 1983.

[83] R. Weinreich, "Efficiency calibration of a Ge(li) detector by absolute counting of fall-out nuclides by means of the 4π $\beta\gamma$ coincidence method," *Nuclear Instruments and Methods*, vol. 125, pp. 601 – 603, 1975.

[84] M. B. Chadwick, "Fission yields and other diagnostics for nuclear performance," *Nuclear Data Sheets*, vol. 120, pp. 297–307, June 2014.

[85] A. Figueiredo, M. Saiki, and L. Marques, "Determination of rare earth elements, U and Th in the standard rock GS-N by neutron activation analysis," *Inorganica Chimica Acta*, vol. 140, pp. 285 – 287, 1987.

[86] S. Kagami and T. Yokoyama, "Chemical separation of Nd from geological samples for chronological studies using ^{146}Sm-^{142}Nd and ^{147}Sm-^{143}Nd systematics," *Analytica Chimica Acta*, vol. 937, pp. 151 – 159, 2016.

[87] D. D. München and H. M. Veit, "Neodymium as the main feature of permanent magnets from hard disk drives (HDDs)," *Waste Management*, vol. 61, pp. 372 – 376, 2017.

[88] J. Coey, "Rare-earth magnets," *Endeavour*, vol. 19, no. 4, pp. 146 – 151, 1995.

[89] A. A. Kondrukevich, A. S. Vlasov, Y. T. Platov, *et al.*, "Color of porcelain containing neodymium oxide," *Glass and Ceramics*, vol. 65, pp. 203–207, May 2008.

[90] L. W. Riker, *The Use of Rare Earths in Glass Compositions*, ch. 4, pp. 81–94.

[91] J. E. Geusic, H. M. Marcos, and L. G. V. Uitert, "Laser oscillations in Nd-doped yttrium aluminum, yttrium gallium and gadolinium garnets," *Appl. Phys. Lett.*, vol. 4, no. 182, 1964.

[92] R. Paschotta, *Neodymium-Doped Gain Media*. Wiley-VCH, 1 ed., Oct. 2008.

[93] N. Nica, "Nuclear data sheets for A = 147," *Nuclear Data Sheets*, vol. 110, pp. 749–997, Apr. 2009.

[94] M. M. Bé, V. Chisté, C. Dulieu, *et al.*, *Table of Radionuclides*, vol. 7 of *Monographie BIPM-5*. Pavillon de Breteuil, F-92310 Sèvres, France: Bureau International des Poids et Mesures, 2013.

[95] R. Roussille, J. Pinston, H. Börner, *et al.*, "Level structure of ^{147}Nd (i). The ^{146}Nd (n, γ) reaction," *Nuclear Physics A*, vol. 246, no. 2, pp. 380 – 394, 1975.

[96] J. A. Pinston, R. Roussille, G. Bailleul, *et al.*, "Level structure of ^{147}Nd (ii). The decay of ^{147}Pr," *Nuclear Physics A*, vol. 246, no. 2, pp. 395 – 401, 1975.

[97] R. Roussille, J. Pinston, F. Braumandl, *et al.*, "Level structure of ^{147}Nd (iii). The ^{146}Nd (n, e-) reaction," *Nuclear Physics A*, vol. 258, no. 2, pp. 257 – 263, 1976.

[98] E. Jacobs, K. Heyde, M. Dorikens, *et al.*, "The decay of ^{147}Nd," *Nuclear Physics A*, vol. 99, no. 3, pp. 411 – 420, 1967.

[99] M. J. Canty and R. D. Connor, "The decay of ^{147}Nd," *Nuclear Physics A*, vol. 104, no. 1, pp. 35 – 48, 1967.

[100] J. C. Hill and M. L. Wiedenbeck, "The decay of ^{147}Nd," *Nuclear Physics*, no. A98, pp. 599 – 613, 1967.

[101] H. Beekhuis, P. Boskma, J. van Klinken, *et al.*, "The β decay of ^{147}Nd," *Nuclear Physics*, vol. 79, no. 1, pp. 220 – 230, 1966.